Supplementary Material for

The impact of recent diurnally asymmetric warming on atmospheric dryness and terrestrial vegetation productivity

Ziqian Zhong*, Hans W. Chen

Department of Space, Earth and Environment, Division of Geoscience and Remote Sensing, Chalmers University of Technology, SE-412 96 Gothenburg, Sweden

*e-mail: ziqian.zhong@chalmers.se

Please note that:

This supporting material contains figures from manuscripts currently under review. Consequently, we are unable to share these materials at this stage. The relevant content will be made publicly available upon the paper's publication. For further information, please feel free to contact Ziqian Zhong.

nature communications

Article

https://doi.org/10.1038/s41467-023-43007-6

Reversed asymmetric warming of sub-diurnal temperature over land during recent decades

Received: 30 April 2023

Accepted: 30 October 2023

Published online: 08 November 2023

Check for updates

Ziqian Zhong[1,2], Bin He[1] ✉, Hans W. Chen[2], Deliang Chen[3], Tianjun Zhou[4], Wenjie Dong[5], Cunde Xiao[6], Shang-ping Xie[7], Xiangzhou Song[8], Lanlan Guo[1], Ruiqiang Ding[6], Lixia Zhang[4], Ling Huang[9], Wenping Yuan[5], Xingming Hao[10], Duoying Ji[1] & Xiang Zhao[11]

In the latter half of the twentieth century, a significant climate phenomenon "diurnal asymmetric warming" emerged, wherein global land surface temperatures increased more rapidly during the night than during the day. However, recent episodes of global brightening and regional droughts and heatwaves have brought notable alterations to this asymmetric warming trend. Here, we re-evaluate sub-diurnal temperature patterns, revealing a substantial increase in the warming rates of daily maximum temperatures (T_{max}), while daily minimum temperatures have remained relatively stable. This shift has resulted in a reversal of the diurnal warming trend, expanding the diurnal temperature range over recent decades. The intensified T_{max} warming is attributed to a widespread reduction in cloud cover, which has led to increased solar irradiance at the surface. Our findings underscore the urgent need for enhanced scrutiny of recent temperature trends and their implications for the wider earth system.

The surface air temperature (SAT) is a commonly used measure of land surface climate change due to its ability to represent terrestrial energy exchange with reasonable accuracy[1,2]. In addition to daily average temperatures, the diurnal temperature range (DTR), defined as the difference between the daily maximum temperature (T_{max}) and daily minimum temperature (T_{min}), provides useful information about the climate[3,4]. Changes in DTR have received considerable attention because it is closely linked with crop yields[5–7], plant growth[8–11], animal wellbeing[12,13] and human health[14–16]. Existing studies found that the surface warming since the 1950s has been associated with larger increases in T_{min} than in T_{max}, i.e., decreases in DTR, which is commonly known as night warming or asymmetric warming[17–20].

Changes in DTR are complex; the changes are subject to many factors, including cloud cover[21–23], solar radiation[24,25], aerosols[26], precipitation[27,28], planetary boundary layer height[29], land use change[30,31] and deforestation[32,33]. For example, an increase in total cloud cover reduces DTR due to a decrease in daytime surface insolation and an increase in night-time downwards longwave radiation[34].

[1]State Key Laboratory of Earth Surface Processes and Resource Ecology, Faculty of Geographical Science, Beijing Normal University, Beijing 100875, China. [2]Department of Space, Earth and Environment, Division of Geoscience and Remote Sensing, Chalmers University of Technology, SE-412 96 Gothenburg, Sweden. [3]Regional Climate Group, Department of Earth Sciences, University of Gothenburg, S-40530 Gothenburg, Sweden. [4]Institute of Atmospheric Physics, Chinese Academy of Sciences, Beijing 100029, China. [5]School of Atmospheric Sciences, Sun Yat-Sen University, Guangzhou 510275, China. [6]State Key Laboratory of Earth Surface Processes and Resource Ecology, Beijing Normal University, Beijing 100875, China. [7]Scripps Institution of Oceanography, University of California San Diego, La Jolla, CA 92039, USA. [8]Key Laboratory of Marine Hazards Forecasting, Ministry of Natural Resources (MNR), Hohai University, Nanjing 210024, China. [9]College of Urban and Environmental Sciences, Peking University, Beijing 100871, China. [10]State Key Laboratory of Desert and Oasis Ecology, Xinjiang Institute of Ecology and Geography, Chinese Academy of Sciences, Urumqi 830011, China. [11]State Key Laboratory of Remote Sensing Science, Beijing Normal University, Beijing 100875, China. ✉e-mail: hebin@bnu.edu.cn

Increases in precipitation and soil moisture can reduce T_{max} and therefore DTR through increased evaporative cooling[35]. However, considering known changes in these processes, the higher warming rate of T_{min} than that of T_{max} is seemingly inconsistent with two recent phenomena. One contradiction is the increase in surface solar radiation that has occurred since the late 1980s, which is referred to as brightening after dimming[36–38]. Solar radiation affects T_{max} more than T_{min}[26], thus, brightening should contribute to further warming of T_{max}. The second contradiction is the increased occurrence of drought events and heatwaves, especially in spring and summer[39–41]. This phenomenon indicates that the cooling effect of soil moisture may have been weakened, which should lead to a faster increase in T_{max}. Motivated by these different changes, we re-evaluated the warming rates of T_{max} and T_{min} over the period of 1961–2020 and investigated the causes behind the associated changes in DTR.

Results

Observed reversing asymmetric warming

With changes in recent years included, we evaluated the surface warming rates of T_{max} and T_{min} using two station observation-based datasets from Berkeley Earth Surface Temperatures (BEST)[42] and the Climatic Research Unit Time-Series version 4.07 (CRU TS)[43]. Both datasets were gridded and gap-filled over the land masses, and BEST was used to detect global surface temperature changes in the Intergovernmental Panel on Climate Change (IPCC) sixth assessment report[44]. As shown in Fig. 1a, b, the trends in the global area-weighted average of T_{max} calculated using a 30-year moving window increased faster than that of T_{min} during 1961–2020. The warming rate in global average T_{max} reached the warming rate in T_{min} in recent decades, with an earlier surpassing moment in BEST than in CRU TS. In the last 30-year window (1991–2020), both datasets exhibit a slight (CRU TS dataset) or substantially more pronounced (BEST dataset) rise in the global average of T_{max} compared to that of T_{min}. Spatially, a stronger warming rate of T_{max} was found in almost 25% of the land area in the earlier time window (1961–1990); the area expanded rapidly, and in the recent time window (1991–2020) the area of stronger warming rate of T_{max} was found in at least half of the area (approximately 52% in CRU TS and 70% in BEST, Fig. 1e, f, with consistent results between the two datasets in 61% of the total land area). Observations from stations based on Global Surface Summary of the Day (GSOD) support the finding of a greater increase in T_{max} than in T_{min} from 1991–2020 (Fig. 2). Analyzes of all observed monitoring sites indicate that 63% of the sites exhibited an overall upward trend in DTR, while more than one-third (35%) of all sites displayed a statistically significant increase in DTR during 1991–2020. Spatially, a widespread decreasing trend in DTR was detected (81% and 76% land area fraction in the BEST and CRU TS temperature datasets, respectively) for the period 1961–1990, with the exceptions of southern Africa, Southern Europe, and some regions in Northern America (Fig. 1c, d). However, during the recent decades of 1991–2020, both temperature datasets show a consistent increase in DTR over more than half of the land area, in particular over the western United States, southern Europe, West Africa, inner East Asia, and Australia.

Our analyzes reveal that the reversal of asymmetric warming was more pronounced in the BEST dataset compared with CRU TS. We assessed the accuracy of these two sets of gridded DTR data by comparing them against GSOD station DTR data (see Methods). The findings revealed a significantly stronger correlation between BEST's DTR data and the GSOD station dataset (one-tailed t-test, $p < 0.001$) compared to the correlation between CRU TS's DTR data and the GSOD station dataset (Supplementary Fig. 1). Thus, in the subsequent analysis we used the BEST dataset to study annual and seasonal trends in T_{max}, T_{min} and DTR for the periods 1961–1990 and 1991–2020.

A significant decline in the global average of DTR (−0.08 °C decade^{-1}, $p < 0.05$) was found during 1961–1990. For the period 1991–2020, the globally averaged DTR increased at a rate of 0.06 °C decade^{-1} ($p < 0.05$) (Supplementary Fig. 2c). This reversal in DTR occurred mainly due to a marked increase in T_{max} for the latter period (0.35 °C year^{-1} decade^{-1}, $p < 0.05$ during 1991–2020 vs. 0.13 °C year^{-1} decade^{-1}, $p < 0.05$ during 1961–1990, Supplementary Fig. 2a, b). Seasonally, the largest decline in DTR was detected in winter during 1961–1990, which is consistent with previous findings[35]. Significant increases ($p < 0.05$) in DTR were detected in spring, summer and winter, which were mainly caused by a significant increase in T_{max} (Supplementary Fig. 2a). All these evidences point to a reversing asymmetric warming over land in recent decades.

Potential mechanisms behind reversing asymmetric warming

Earlier studies suggested that the recent global warming is mainly forced by greenhouse gases[45], while changes in DTR are influenced largely by cloud cover[23,46]. In addition, aerosols and soil moisture may also have affected the variability of DTR[47,48]. These potential drivers of DTR exhibit a high degree of correlation. For instance, the phenomenon of aerosol-cloud interactions, such as the influence of aerosols on cloud albedo[49] and lifetime[50], has gained growing attention[51–53]. Moreover, clear associations can be observed between cloud cover and soil moisture, as increasing cloud cover is associated with enhanced precipitation[54], which subsequently leads to soil wetting. The intricate interactions among these factors highlight the presence of high multi-collinearity when performing regression analysis with them as independent variables, posing challenges in discerning the dominant drivers of DTR change. To address the impact of multi-collinearity and accurately identify relationships, we conducted ridge regression analyzes[55] at individual grid points. This analysis (Methods) employed as independent variables monthly total cloud cover from the fifth-generation ECMWF reanalysis (ERA5)[56] dataset, aerosol optical depth from Modern-Era Retrospective analysis for Research and Applications, version 2 (MERRA-2)[57], and soil moisture from the Global Land Evaporation Amsterdam Model (GLEAM)[58] dataset, while DTR was calculated from the BEST dataset as the dependent variable spanning 1981 to 2020. Ridge regression is a linear regression method with regularization that can effectively address the issue of multi-collinearity. By introducing a penalty term in the cost function that discourages overly large parameter values, it improves upon the ordinary least squares regression model in scenarios where there exist strong correlations among independent variables. An evaluation of the ridge regression (Methods) shows that the ridge regression model can capture the majority of the explained variance in DTR (Supplementary Fig. 3a), except in certain regions in particularly Africa, South America, and Northern Hemisphere high-latitudes.

The analysis using ridge regression suggests a worldwide negative response of DTR to changes in total cloud cover and soil moisture (Supplementary Fig. 3b, d), with generally stronger negative impacts of cloud cover than soil moisture. This result aligns with previous findings[21,23]. Negative responses of DTR to aerosol concentrations are detected in Western Africa, the Arabian Peninsula, India and southern China (Supplementary Fig. 3c). To make a quantitative comparison, Fig. 3 shows a cyan-magenta-yellow (CMY) composite map (see Methods) of the relative contributions of total cloud cover, aerosol and soil moisture to DTR. Generally, changes in DTR during 1981–2020 were dominated by cloud cover variations over 83.5% of the global land area; this phenomenon is widely detected in most of North America, southern South America, Europe, southern Africa, Central Asia, and East Asia. Moreover, the dominant effect of cloud cover on DTR over land is further confirmed when using an independent total cloud cover dataset obtained from the Moderate Resolution Imaging Spectroradiometer (MODIS) satellite during 2003–2020 (84.4% of the total land area; Supplementary Fig. 4).

The ridge regression analysis assumes linear relationships and may overlook the non-linear associations among cloud, aerosol,

https://doi.org/10.1038/s41467-023-43007-6

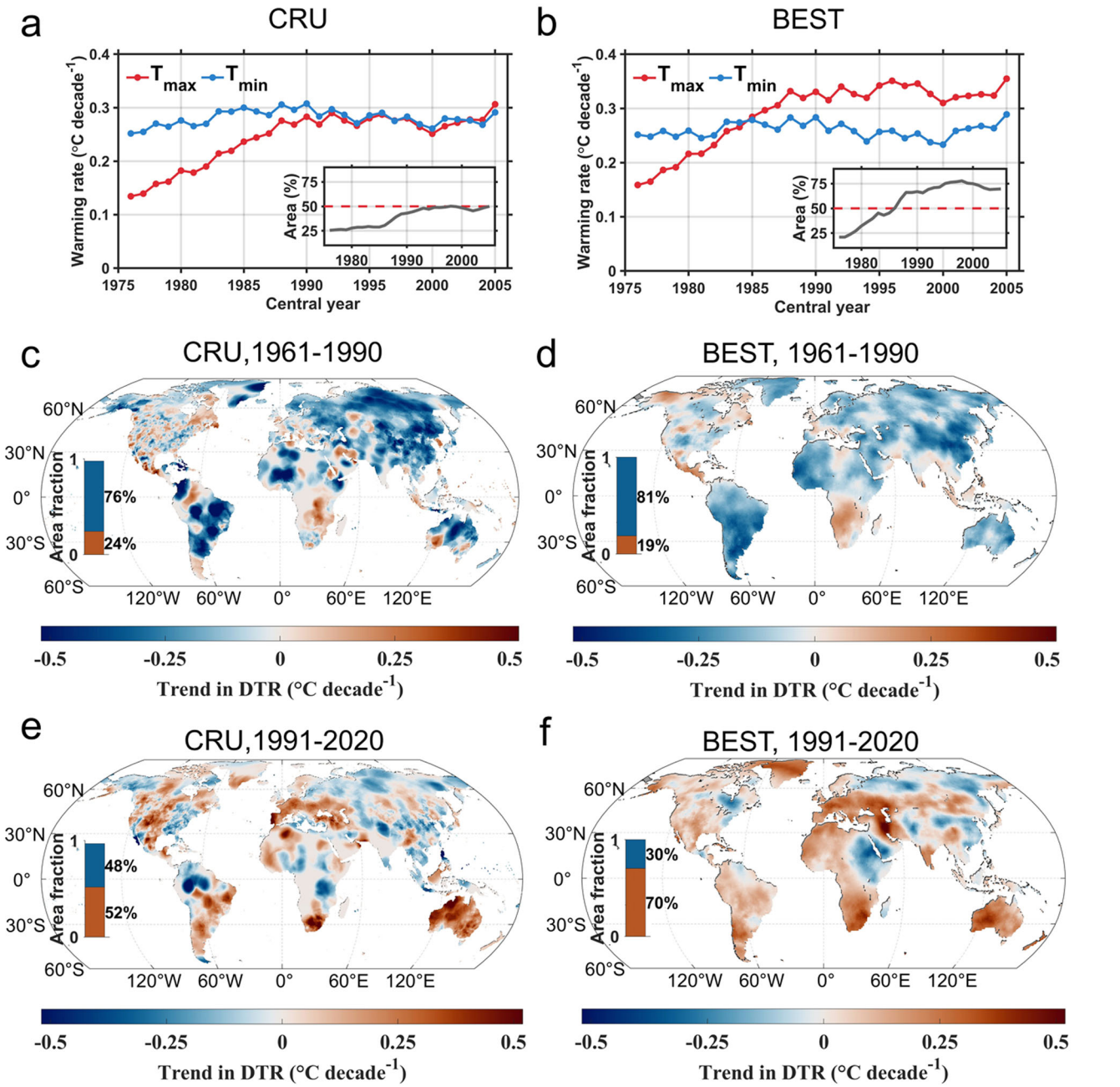

Fig. 1 | Trends in the daily maximum temperature (T_{max}), daily minimum temperature (T_{min}) and diurnal temperature range (DTR). a, **b** Global area-weighted average warming rates derived from the CRU TS (**a**) and BEST (**b**) datasets in T_{max} (red) and T_{min} (blue). The trends were calculated using a 30-year moving window over 1961–2020. The *x*-axis shows the central year (rounding down) of the moving window. The inset shows the area fraction over land (%) with faster warming rates of T_{max} than T_{min}. **c**–**f** Spatial distribution of the trend in DTR in CRU TS during 1961–1990 (**c**) and 1991–2020 (**e**), and in BEST during 1961–1990 (**d**) and 1991–2020 (**f**).

soil moisture, and DTR. To address this limitation, we repeated the regression analysis using the Random Forest algorithm[59] (Methods). Random Forest is a machine learning technique based on decision trees and can capture non-linear relationships. The results from the Random Forest regression consistently corroborate our prior findings, indicating that total cloud cover is indeed the dominant driving force behind DTR fluctuations in terrestrial regions, encompassing a substantial proportion (79.1%) of the land area (Supplementary Fig. 5). DTR is significantly negatively correlated with total cloud cover in most regions of the terrestrial land surface, suggesting that DTR is greatly influenced by cloud cover.

To further elucidate the influence of different environment variables on DTR, we analyzed the changes of DTR, total cloud cover, aerosol optical depth and soil moisture over the global land area during recent decades (Supplementary Fig. 6). During the 1960s to the early 1970s, there was a strong and significant upward trend in total cloud cover, which later stabilized. However, a remarkable downward trend emerged from the mid-1980s onwards. This decline in cloud cover corresponded with an increase in DTR during the same period. Between 1981 and 2020, a significant ($p < 0.05$) negative correlation was found between the annual average global surface total cloud cover and DTR. The mean bootstrapped partial correlation coefficient (−0.47; −0.54 to −0.41, 95% confidence interval (CI)) between these two

https://doi.org/10.1038/s41467-023-43007-6

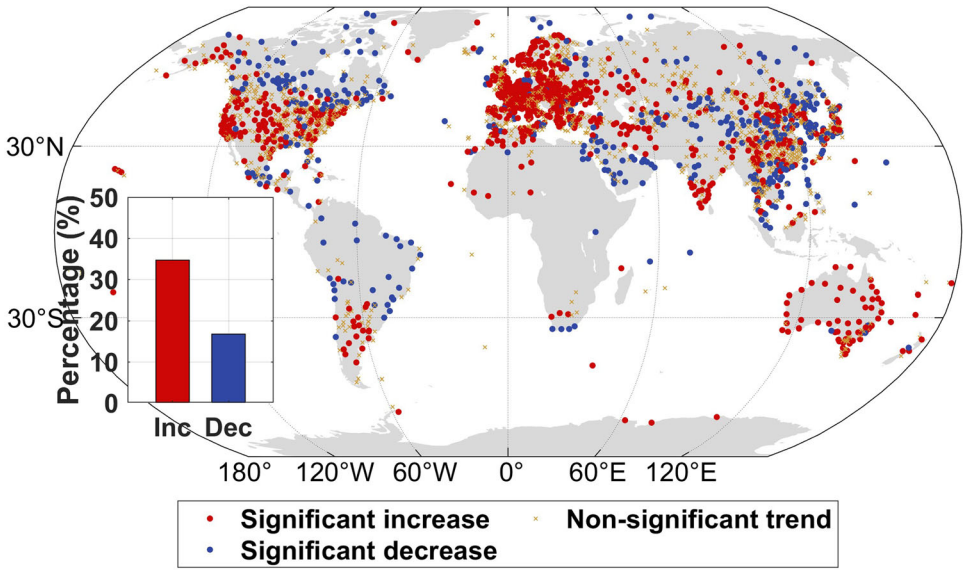

Fig. 2 | Spatial distribution of the trend in diurnal temperature range (DTR) in Global Surface Summary of the Day (GSOD) during 1991–2020. The insets in the figure depict the percentage of sites showing a significant increasing (Inc; $p < 0.05$; red) and significant decreasing (Dec; $p < 0.05$; blue) trend in DTR.

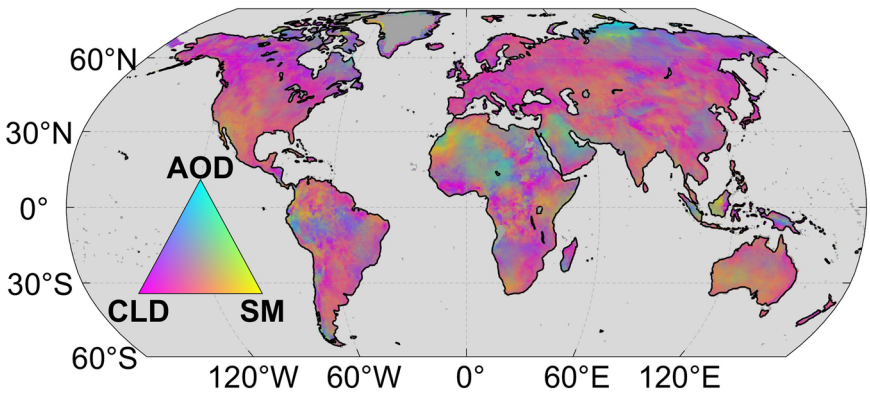

Fig. 3 | Cyan-magenta-yellow (CMY) composite of diurnal temperature range (DTR) sensitivity. The contributions of total cloud cover (CLD; magenta), aerosol optical depth (AOD; cyan) and soil moisture (SM; yellow) to DTR changes during 1981–2020. The color of the composite was determined by the relative contribution from the magnitude of the ridge regression coefficients. Only the grid cells with the regression result that passed the test of significance ($p < 0.05$) in the training set are shown. The CLD was from the fifth-generation ECMWF reanalysis (ERA5) dataset, AOD was from Modern-Era Retrospective analysis for Research and Applications, version 2 (MERRA-2), and SM was from the Global Land Evaporation Amsterdam Model (GLEAM) dataset.

variables was higher than that of the mean correlation between DTR and soil moisture (−0.31; −0.39 to −0.23, 95% CI), as well as the correlation between DTR and aerosol optical depth (−0.18; −0.28 to −0.07, 95% CI).

Cloud cover can influence DTR through two primary mechanisms. On the one hand, diminished cloud cover leads to greater daytime solar radiation, resulting in elevated daytime maximum temperatures and, consequently, an expanded DTR. Conversely, reduced cloud cover leads to decreased night-time outgoing radiation at the surface, causing lower minimum temperatures and further increasing DTR[23,46]. To discern the predominant effect, we calculated the partial correlations between both cloud cover and T_{max} and cloud cover and T_{min} (Supplementary Fig. 7). The results indicate that, overall, the prevalent association is a negative correlation between cloud cover and maximum temperatures. This suggests that decreased cloud cover has led to an increased DTR in recent decades, primarily due to the associated increase in incoming solar radiation, while the impact of night-time cooling has played a secondary role.

To reveal the spatial patterns of cloud and radiation changes, we compared the trends in total cloud cover and solar radiation during the earlier decades (1961–1990) and the recent decades (1991–2020) (Fig. 4). Specifically, a global (over 69% of land) increase in cloud cover corresponded to a decline in solar radiation at the surface over almost three-quarters (74%) of the land area for the period 1961–1990; the dimming has disappeared since the 1990s, and increases in solar radiation were detected in over 63% of global land, which is partly due to an extensive (over 66% of land) decrease in cloud cover. Over the period 1961–1990, central North America, southern South America, the Mediterranean, and Australia saw weak decreases in solar radiation, with the local DTR narrowing or experiencing little change. However, during 1991–2020, a substantial increasing trend in solar incident radiation was detected over central North America, southern South America the Mediterranean, and Australia, corresponding to a local general increase of DTR.

To further elucidate the relationship between incident solar radiation and DTR, we conducted a partial correlation analysis between DTR and incident shortwave radiation extracted from ERA5 (1961–2020), CERES (2001–2020), and MERRA-2 (1981–2020), while adjusting for the influence of soil moisture (Supplementary Fig. 8). The results show a significant positive correlation between

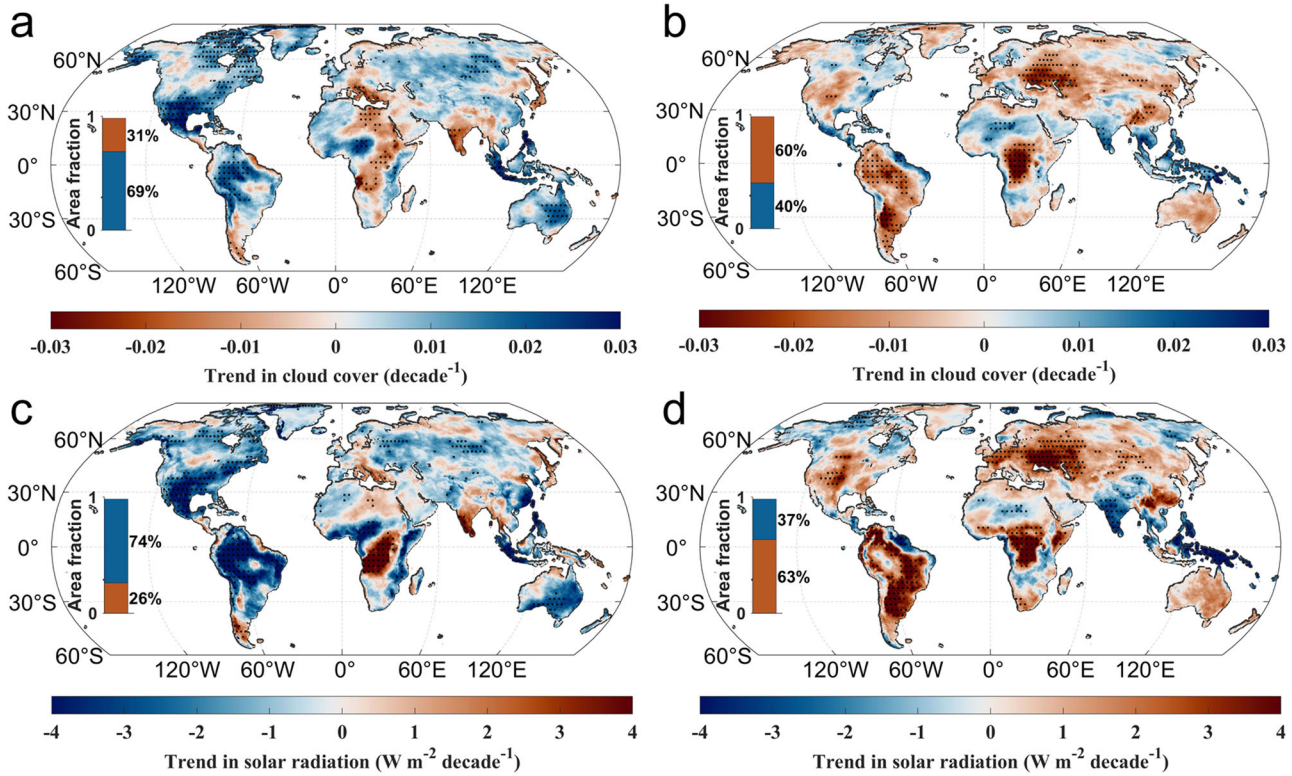

Fig. 4 | Comparisons of trends in total cloud cover and solar radiation between two periods. a, **b** The spatial distribution of trends in total cloud cover during 1961–1990 (**a**) and 1991–2020 (**b**). **c**, **d** The spatial distribution of trends in solar radiation during 1961–1990 (**c**) and 1991–2020 (**d**). The black dots mark the areas where trends are significant at the $p < 0.05$ level. The total cloud cover and solar radiation were from the fifth-generation ECMWF reanalysis (ERA5) dataset.

DTR and surface solar radiation over most land areas of the world in all four datasets, confirming a credible positive influence of solar radiation on DTR, consistent with previous studies[24,25]. The above results indicate that the recent global decrease in cloud cover[60–62] has increased incoming solar radiation at the surface, resulting in a greater increase in T_{max} than in T_{min}, ultimately expanding DTR.

Our analyzes show that the reversed asymmetric warming was mainly driven by changes in cloud cover which led to enhanced solar radiation. Further, the influence of soil moisture or aerosols on DTR appears to be particularly noticeable in certain regions. Although the influence of soil moisture on DTR may not be as substantial as that of cloud cover, it shows relatively extensive spatial distributions across terrestrial surfaces on a global scale (Supplementary Fig. 3d). In those regions, decreasing soil moisture may have contributed to the acceleration of T_{max} increases and thus decreasing DTR, possibly due to less effective daytime evaporation cooling on air temperature during dry conditions. Additionally, the increase in DTR in the Mediterranean over the past three decades may be related to a decrease in aerosol concentrations (Supplementary Fig. 9b), which is likely linked to reductions in local aerosol and precursor emissions[63]. However, due to the little change in global drought[64] and the relatively short-lived influence of aerosol on DTR[65], the overall impact of soil moisture and aerosols on the global asymmetric warming pattern was limited. In addition to these three environmental factors, changes in DTR may be closely associated with land use/land cover change (LULCC). Given the complexity of LULCC's effects, our study specifically focuses on exploring one potential impact: changes in albedo. However, we found that there was no significant positive or negative correlation between changes in albedo and DTR across the majority of land areas (Supplementary Fig. S10). This finding indicates a limited influence of LULCC on global asymmetric warming.

Discussion

The reversing asymmetric warming is supported by regional increasing DTR trends in Europe[66], Central Asia[67], South India[68] and Australia[69] during recent decades. Globally, it was reported that most of the global-mean DTR decrease occurred between 1960 and 1980. After that period, globally averaged DTR exhibited little change from 1979 to 2012[70]. Here we found that global DTR has reversed from decreasing to increasing in the recent three decades based on two observation-based datasets and station observations. While there are differences between the two gridded temperature datasets, particularly in South America and Africa where the observational coverage is limited[71,72], the increasing DTR in Europe, Australia, and Northern America is robust due to the dense observations in these regions. It is worth noting that the large number of land stations (approximately 39,000 records) and the diverse range of sources (8 sources) integrated within the BEST temperature dataset could potentially explain its higher correlation with the observed temperatures from the stations in the GSOD dataset, as compared to the CRU TS temperature dataset. In addition to disparities in station selection, variations in gridding and interpolation methodologies[69], as well as the implementation of quality assurance procedures[73], may also contribute to the differences in detected regional DTR trends between these two datasets. With that said, irrespective of the dataset employed, it is evident that more than half of the global land surface has displayed a discernible increasing trend in DTR over the past three decades. This finding signals a fundamental shift in the pattern of asymmetric warming.

The results of the ridge regression analysis in this study suggest that statistical models incorporating total cloud cover, aerosol optical depth, and soil moisture as independent variables can effectively capture the variations in DTR across most land areas. The model fit is relatively low in regions such as South America and Africa (Supplementary Fig. 3a) where the observational coverage is limited. These regions are also where the CRU TS and BEST gridded temperature

datasets show the largest discrepancies in DTR trends in the later period (1991–2020), which shows that there are considerable uncertainties in the estimated DTRs in regions with few observations. Additionally, in this study, we did not include other potentially relevant factors such as precipitation[28,74], atmospheric water vapor[23,75], vegetation[76], LULCC[45,77,78] and regional atmospheric circulation[79]. This omission may introduce further uncertainty. Increased precipitation, for example, is closely linked to decreased DTR, which can be attributed to the strong association between precipitation, cloud cover, atmospheric water vapor, radiation, and soil moisture[29,74]. Future studies are needed to disentangle the effects of these highly correlated variables on DTR. Prior research conducted in specific regions, such as China and India[77,78], has demonstrated that LULCC exerts a notable influence on DTR. In light of the intricate nature of LULCC's effects, our study specifically focuses on exploring the potential impact of changes in albedo. However, we found that there is a relatively weak correlation between DTR and albedo across the majority of land areas. This could be attributed to the fact that LULCC encompasses other processes, such as vegetation dynamics[76,80,81]. Further studies are needed to gain a comprehensive understanding of the entire scenario.

We found that the reversed asymmetric warming is closely linked with changes in solar radiation associated with total cloud cover. This finding offers fresh insights into and a different perspective on global climate change in recent decades. Given that clouds may continue to have a positive feedback on global warming through radiative fluxes[82,83], this radiation-induced phenomenon, in which the rising rate of T_{max} exceeds that of T_{min}, may persist and potentially intensify in the future. Therefore, more attention needs to be paid to this asymmetric warming phenomenon from the perspective of tackling the ongoing challenges posed by global warming.

Methods

Data

The T_{max} and T_{min} data utilized in this study were obtained from the Climatic Research Unit Time-Series version 4.07 (CRU TS)[43] and Berkeley Earth Surface Temperatures (BEST) datasets[42]. The CRU TS temperature dataset is derived from a blend of data sources including weather station records, ship logs, and more recent satellite observations. This dataset undergoes meticulous calibration to account for biases and variations in measurement methods, making it an extensively used resource in climate research for documenting long-term temperature trends and variations. It provides spatiotemporal resolutions of 0.5° × 0.5° on a monthly basis, covering the period from 1901 to 2022.

The BEST dataset encompasses a larger sample of approximately 39,000 records. It employs advanced statistical techniques to quantify and adjust measurement biases, ensuring a highly accurate representation of global temperature trends. This dataset offers spatiotemporal resolutions of 1° × 1° on a monthly basis, spanning from 1850 to the present.

In situ T_{max} and T_{min} records were acquired from the Global Surface Summary of the Day (GSOD) database, downloaded in September 2021 from https://data.nodc.noaa.gov/cgi-bin/iso?id=gov.noaa.ncdc:C00516. The GSOD dataset originates from the Integrated Surface Hourly (ISH) database developed by the US National Climatic Data Center. This dataset contains meteorological variables, including temperature, precipitation, and wind speed, from over 9000 weather stations. The original observations undergo rigorous quality control procedures to ensure their accuracy[84]. Specifically, we selected daily maximum and minimum temperature data with relatively complete records from all stations covering the period 1991 to 2020. We employed stringent selection criteria to exclude incomplete data series, only including stations with missing values not exceeding one year of the analysis period (1991 to 2020) and with complete records for all 12 months. Furthermore, we required each monthly value to be derived from at least 15 days of data. Consequently, our trend analysis encompassed a total of 2557 stations.

Monthly data on total cloud cover were obtained from the fifth-generation ECMWF reanalysis (ERA5) dataset[56] on a 0.25° × 0.25° regular latitude–longitude grid (the native resolution of ERA5 is about 31 km). In addition, monthly total cloud cover was obtained from the MODIS MCD06COSP data at a spatial resolution of 1° × 1° after 2003. ERA5 total cloud cover was used for the main analyzes.

The monthly incident shortwave radiation data in all-sky conditions were obtained from the ERA5 dataset on a 0.25° grid, the Cloud and the Earth's Radiant Energy System energy balanced and filled edition 4.1 (CERES–EBAF)[85] dataset at a spatial resolution of 1° × 1° after March 2000, and the Modern-Era Retrospective analysis for Research and Applications, version 2 (MERRA-2)[57] dataset with a spatial resolution of 0.625° × 0.5° after 1980.

The monthly average aerosol optical depth and surface albedo at a spatial resolution of 0.625°×0.5° was obtained from the MERRA-2 dataset beginning in 1980. The monthly surface soil moisture at a spatial resolution of 0.25° was obtained from the Global Land Evaporation Amsterdam Model (GLEAM) version 3.5 dataset[58], which is a global dataset spanning 40 years from 1981 to 2020 and based on satellite and reanalysis data. The cloud cover, radiation, aerosol optical depth, and soil moisture data sets were aggregated to a common 0.5° grid.

Assessment of temperature-gridded data

We assessed the accuracy of the temperature gridded data using GSOD station temperature dataset. The evaluation period spanned from 1978 to 2020, during which the GSOD data records were relatively complete. Following a similar methodology used in analyzing station-based DTR trends, we selected a total of 2,058 stations with missing observations comprising less than 5% of the evaluation period for temperature-gridded data assessment. In the evaluation process, we extracted the time series of DTR from the gridded BEST and CRU TS datasets corresponding to each station's location. Daily data were averaged to obtain yearly data and missing values at these stations were filled using linear interpolation. We then computed Pearson correlation coefficients between the annual station observation series and the observed DTR sequence at each station, serving as an indicator of accuracy. The significance of the correlation coefficient differences between the DTR station data and the two sets of DTR gridded data was tested by the one-tailed Student's *t*-test.

Seasonal analysis

To analyze DTR variations by season, we defined the seasons as follows: March, April, May for spring (autumn), June, July, August for summer (winter), September, October, November for autumn (spring), and December, January, February for winter (summer) in the Northern Hemisphere (Southern Hemisphere). Correspondingly, the annual average value of a variable in one year is defined as the average of 12 months from December in the preceding year to November of that year.

Ridge regression

Ridge regression is a method for estimating coefficients in multiple linear regression models in scenarios characterized by high correlations among the independent variables. In ridge regression, a regularization term is introduced to the standard least squares objective function, aiding in stabilizing the estimated coefficients. This regularization term is controlled by a tuning parameter denoted as λ. The ridge regression objective function can be expressed as follows:

$$\hat{\beta} = \sum_{i=1}^{n} \left(y_i - \beta_0 - \sum \beta_i x_i \right)^2 + \lambda \sum \beta_i^2 \quad (1)$$

where $\hat{\beta}$ represents the estimated regression coefficients, y_i is the dependent variable, β_0 is the intercept term, and β_i signifies the regression coefficient for the independent variable x_i. The tuning parameter λ governs the extent of shrinkage applied to the coefficients. When λ is set to zero, the regularization term exerts no effect, and ridge regression reduces to ordinary least squares regression. However, as λ increases, the penalty term gains influence. The larger λ becomes, the more pronounced is the shrinkage applied to the coefficients. Consequently, ridge regression effectively mitigates the impact of multi-collinearity.

Prior to performing the ridge regression analysis in this study, all-time series were detrended by subtracting the linear trend and transformed into z-scores by subtracting the monthly climatology means dividing by the monthly climatological standard deviations from 1981 to 2020. For validation, the z-scores were randomly divided into an 80% calibration dataset and a 20% validation dataset. The dataset in the training set was used to train the ridge regression model, while the dataset in the validation set was employed to assess the performance of the ridge regression model. Afterwards, all the datasets were merged to determine the ridge regression coefficients.

The ridge regression was performed on the variables in each grid cell, and the tuning parameter λ was determined for each grid cell based on the Variance Inflation Factor (VIF) of the independent variables within each individual grid cell. VIF serves as a measure of multi-collinearity among the independent variables in the regression model. The following formula was used to calculate the VIF:

$$VIF_i = \frac{1}{1 - R_i^2} \tag{2}$$

where R_i^2 denotes the coefficient of determination between the ith independent variable and all other independent variables. A higher VIF value indicates stronger multi-collinearity within the regression model's independent variables. Here, a VIF value less than 3 suggests an acceptable level of multi-collinearity[86].

Throughout the regression analysis process, the initial value of λ was set to 0 and incremented by a step size of 0.01. As λ increased, the degree of multi-collinearity decreased, subsequently resulting in a decline in the VIF value. The incrementation of λ ceased when the VIF value dropped below 3, with this λ value being determined as the tuning parameter at this grid point. The significance of the ridge regression analysis was assessed utilizing an F-test at a significance level of 0.05. The accuracy of the ridge regression model was evaluated by employing the coefficient of determination on the validation dataset.

CMY composite

The color of the cyan-magenta-yellow (CMY) composite was determined by the relative contributions from the magnitudes of the ridge regression coefficients (R.c), which can be expressed as follows:

$$C = \frac{|R.c_{x1}|}{|R.c_{x1}| + |R.c_{x2}| + |R.c_{x3}|} \tag{3}$$

$$M = \frac{|R.c_{x2}|}{|R.c_{x1}| + |R.c_{x2}| + |R.c_{x3}|} \tag{4}$$

$$Y = \frac{|R.c_{x3}|}{|R.c_{x1}| + |R.c_{x2}| + |R.c_{x3}|} \tag{5}$$

Here, $R.c_{x1}$, $R.c_{x2}$, $R.c_{x3}$ represent the R.c of DTR to variables x_1, x_2, and x_3, respectively. We denoted the relative contributions of variables x_1, x_2, and x_3 to DTR as C, M, and Y, respectively. These contributions then served as the brightness values for the cyan, magenta, and yellow channels, respectively, culminating in the generation of a CMY image.

Random Forest regression analysis

We also utilized the Random Forest algorithm for regression analysis[59]. The input to the Random Forest was standardized in the same way as for the ridge regression analysis, and the data was also randomly partitioned into an 80% calibration dataset and a 20% validation dataset for the validation. During the modeling process at individual grid cells, the Random Forest algorithm leveraged the provided sequences of independent variables and dependent variables in the calibration dataset to train 100 decision trees. Each decision tree independently predicted DTR values based on the given predictor variables. Moreover, we employed out-of-bag (OOB) prediction error estimation, an inherent capability of the Random Forest algorithm. Additionally, we assessed the importance of predictors by enabling the OOB Predictor Importance feature, providing insights into the relative contributions of total cloud cover, aerosol optical depth, and soil moisture in predicting DTR. Similar to the ridge regression coefficients, these Predictor Importance features were subsequently utilized in generating a CMY image.

Partial correlation analysis and bootstrap method for assessing relationships

To determine the magnitude of the relationship between annual solar radiation and DTR, T_{max} or T_{min} at individual grid points, while controlling for the effect of soil moisture, we conducted a partial correlation analysis. Partial correlation analysis is a statistical technique used to assess the relationship between two variables while controlling for the influence of one or more additional variables. Here, both the variables involved in the correlation analysis and the variable being controlled for were specific to each individual grid cell. The significance of the partial correlations was evaluated at a threshold of $p < 0.05$.

The uncertainties of the partial correlations between global annual DTR and total cloud cover, soil moisture, or aerosol optical depth were assessed using the bootstrap method[87]. Specifically, we generated 1000 bootstrap samples through random samples with replacements from the original data to create samples of equal size to the original dataset. For each bootstrap sample, we computed the partial correlation coefficient between DTR and an environmental factor while adjusting for the potential confounding effect of other variables. Subsequently, we calculated the mean correlation coefficient across all bootstrap samples and determined the 95% confidence interval using the 2.5th to 97.5th percentile of the bootstrap distribution.

Data availability

All data needed to evaluate the conclusions in the paper are present in the paper and/or the Supplementary Materials. The source data underlying Figs. 1–4 are provided as Source Data files and have been deposited in the Figshare repository available at https://doi.org/10.6084/m9.figshare.24310699.v1[88]. The CRU temperature dataset is from https://crudata.uea.ac.uk/cru/data/hrg/. The Berkeley Earth Surface Temperature dataset is from https://berkeleyearth.org/data/. The Global Surface Summary of the Day dataset is from https://data.nodc.noaa.gov/cgi-bin/iso?id=gov.noaa.ncdc:C00516. The ERA5 cloud cover, incident shortwave radiation and temperature dataset is from https://cds.climate.copernicus.eu/cdsapp#!/dataset/reanalysis-era5-single-levels-monthly-means?tab=form. The MODIS cloud dataset is from https://modis.gsfc.nasa.gov/data/. The Cloud and the Earth's Radiant Energy System energy balanced and filled cloud cover and incident shortwave radiation dataset is from https://asdc.larc.nasa.gov/project/CERES/CERES_EBAF_Edition4.1. The MERRA-2 downwards shortwave radiation, aerosol optical depth and surface albedo dataset

is from https://disc.gsfc.nasa.gov/datasets?project=MERRA-2. The GLEAM soil moisture data is from https://www.gleam.eu/#datasets.

Code availability

The code for the analysis and mapping can be obtained from the Figshare repository (https://doi.org/10.6084/m9.figshare.24310699.v1)[88].

References

1. Ji, F., Wu, Z., Huang, J. & Chassignet, E. P. Evolution of land surface air temperature trend. *Nat. Clim. Change* **4**, 462–466 (2014).
2. Jhajharia, D. & Singh, V. P. Trends in temperature, diurnal temperature range and sunshine duration in Northeast India. *Int. J. Climatol.* **31**, 1353–1367 (2011).
3. Braganza, K., Karoly, D. J. & Arblaster, J. M. Diurnal temperature range as an index of global climate change during the twentieth century. *Geophys. Res. Lett.* **31**, https://doi.org/10.1029/2004GL019998 (2004).
4. Shahid, S., Harun, S. B. & Katimon, A. Changes in diurnal temperature range in Bangladesh during the time period 1961–2008. *Atmos. Res.* **118**, 260–270 (2012).
5. Lobell, D. B. Changes in diurnal temperature range and national cereal yields. *Agric. For. Meteorol.* **145**, 229–238 (2007).
6. Peng, S. B. et al. Rice yields decline with higher night temperature from global warming. *Proc. Natl Acad. Sci. USA* **101**, 9971–9975 (2004).
7. Mu, Q., Guo, T. T., Li, X. R. & Yu, J. M. Phenotypic plasticity in plant height shaped by interaction between genetic loci and diurnal temperature range. *N. Phytologist* **233**, 1768–1779 (2022).
8. Zheng, Z. P. et al. Is the pinus massoniana lamb. tree-ring latewood formation influenced by the diurnal temperature range in humid subtropical china? *Forests* **13**, https://doi.org/10.3390/f13091439 (2022).
9. Buntgen, U. et al. Declining pine growth in Central Spain coincides with increasing diurnal temperature range since the 1970s. *Glob. Planet. Change* **107**, 177–185 (2013).
10. Zhang, X. et al. Reduced diurnal temperature range mitigates drought impacts on larch tree growth in North China. *Sci. Total Environ.* **848**, 157808 (2022).
11. Peng, S. S. et al. Asymmetric effects of daytime and night-time warming on Northern Hemisphere vegetation. *Nature* **501**, 88 (2013).
12. Carrington, L. B., Seifert, S. N., Willits, N. H., Lambrechts, L. & Scott, T. W. Large diurnal temperature fluctuations negatively influence aedes aegypti (diptera: culicidae) life-history traits. *J. Med. Entomol.* **50**, 43–51 (2013).
13. Briga, M. & Verhulst, S. Large diurnal temperature range increases bird sensitivity to climate change. *Sci. Rep.* **5**, 16600 (2015).
14. Wu, M. et al. Prenatal exposure of diurnal temperature range and preterm birth: findings from a birth cohort study in China. *Sci. Total Environ.* **656**, 1102–1107 (2019).
15. Zhou, X. D. et al. Acute effects of diurnal temperature range on mortality in 8 Chinese cities. *Sci. Total Environ.* **493**, 92–97 (2014).
16. Sharafkhani, R., Khanjani, N., Bakhtiari, B., Jahani, Y. & Mahdi, R. E. Diurnal temperature range and mortality in Urmia, the Northwest of Iran. *J. Therm. Biol.* **69**, 281–287 (2017).
17. Easterling, D. R. et al. Maximum and minimum temperature trends for the globe. *Science* **277**, 364–367 (1997).
18. Vose, R. S., Easterling, D. R. & Gleason, B. Maximum and minimum temperature trends for the globe: An update through 2004. *Geophysical Research Letters* **32**, https://doi.org/10.1029/2005GL024379 (2005).
19. Phillips, C. L., Gregg, J. W. & Wilson, J. K. Reduced diurnal temperature range does not change warming impacts on ecosystem carbon balance of Mediterranean grassland mesocosms. *Glob. Change Biol.* **17**, 3263–3273 (2011).
20. Intergovernmental Panel on Climate, C. *Climate Change 2013 – The Physical Science Basis: Working Group I Contribution to the Fifth Assessment Report of the Intergovernmental Panel on Climate Change*. (Cambridge University Press, 2014).
21. Sun, B., Groisman, P. Y., Bradley, R. S. & Keimig, F. T. Temporal changes in the observed relationship between cloud cover and surface air temperature. *J. Clim.* **13**, 4341–4357 (2000).
22. Liu, L. et al. Large-scale pattern of the wintertime diurnal temperature range variations over North America during 1979–2018. *Atmos. Res.* **257**, 105614 (2021).
23. Cox, D. T. C., Maclean, I. M. D., Gardner, A. S. & Gaston, K. J. Global variation in diurnal asymmetry in temperature, cloud cover, specific humidity and precipitation and its association with leaf area index. *Glob. Change Biol.* **26**, 7099–7111 (2020).
24. Makowski, K. et al. On the relationship between diurnal temperature range and surface solar radiation in Europe. *J. Geophys. Res.-Atmos.* **114**, https://doi.org/10.1029/2008jd011104 (2009).
25. Liu, B. H., Xu, M., Henderson, M., Qi, Y. & Li, Y. Q. Taking China's temperature: Daily range, warming trends, and regional variations, 1955-2000. *J. Clim.* **17**, 4453–4462 (2004).
26. Stjern, C. W. et al. How aerosols and greenhouse gases influence the diurnal temperature range. *Atmos. Chem. Phys.* **20**, 13467–13480 (2020).
27. He, B., Huang, L. & Wang, Q. F. Precipitation deficits increase high diurnal temperature range extremes. *Scientific Reports* **5**, https://doi.org/10.1038/srep12004 (2015).
28. Dai, A., Genio, A. D. D. & Fung, I. Y. Clouds, precipitation and temperature range. *Nature* **386**, 665–666 (1997).
29. Davy, R., Esau, I., Chernokulsky, A., Outten, S. & Zilitinkevich, S. Diurnal asymmetry to the observed global warming. *Int. J. Climatol.* **37**, 79–93 (2017).
30. Wei, B. C. et al. Land use/land cover change and it's impacts on diurnal temperature range over the agricultural pastoral ecotone of Northern China. *Land Degrad. Dev.* **29**, 3009–3020 (2018).
31. Shen, X., Liu, B. & Lu, X. Effects of land use/land cover on diurnal temperature range in the temperate grassland region of China. *Sci. Total Environ.* **575**, 1211–1218 (2017).
32. Schultz, N. M., Lawrence, P. J. & Lee, X. H. Global satellite data highlights the diurnal asymmetry of the surface temperature response to deforestation. *J. Geophys. Res.-Biogeosciences* **122**, 903–917 (2017).
33. Meier, R., Davin, E. L., Swenson, S. C., Lawrence, D. M. & Schwaab, J. Biomass heat storage dampens diurnal temperature variations in forests. *Environ. Res. Lett.* **14**, https://doi.org/10.1088/1748-9326/ab2b4e (2019).
34. Na, L. et al. Diurnal temperature range variability driven by cloud cover and precipitation in Mongolian Plateau under global warming. *Int. J. Climatol.* **42**, 8184–8200 (2022).
35. Lindvall, J. & Svensson, G. The diurnal temperature range in the CMIP5 models. *Clim. Dyn.* **44**, 405–421 (2015).
36. Wild, M. et al. From dimming to brightening: decadal changes in solar radiation at earth's surface. *Science* **308**, 847–850 (2005).
37. Wild, M. Global dimming and brightening: A review. *J. Geophys. Res. Atmos.* **114** (2009).
38. Wild, M. Enlightening global dimming and brightening. *Bull. Am. Meteorological Soc.* **93**, 27–37 (2012).
39. Li, X. & Wang, S. Recent increase in the occurrence of snow droughts followed by extreme heatwaves in a warmer world. *Geophys. Res. Lett.* **49**, e2022GL099925 (2022).
40. Zhang, R., Sun, C., Zhu, J., Zhang, R. & Li, W. Increased European heat waves in recent decades in response to shrinking Arctic sea ice and Eurasian snow cover. *npj Clim. Atmos. Sci.* **3**, 7 (2020).
41. He, B. et al. Lengthening Dry Spells Intensify Summer Heatwaves. *Geophys. Res. Lett.* **49**, https://doi.org/10.1029/2022gl099647 (2022).

42. Rohde, R. A. & Hausfather, Z. The berkeley earth land/ocean temperature record. *Earth Syst. Sci. Data* **12**, 3469–3479 (2020).
43. Harris, I., Osborn, T. J., Jones, P. & Lister, D. Version 4 of the CRU TS monthly high-resolution gridded multivariate climate dataset. *Sci. Data* **7**, 109 (2020).
44. Gulev, S. K. et al. *Changing State of the Climate System*. *In Climate Change 2021: The Physical Science Basis. Contribution of Working Group I to the Sixth Assessment Report of the Intergovernmental Panel on Climate Change*. 287–422 (Cambridge University Press, 2021).
45. Zhou, L. M., Dickinson, R. E., Tian, Y. H., Vose, R. S. & Dai, Y. J. Impact of vegetation removal and soil aridation on diurnal temperature range in a semiarid region: Application to the Sahel. *Proc. Natl Acad. Sci. USA* **104**, 17937–17942 (2007).
46. Dai, A., Trenberth, K. E. & Karl, T. R. Effects of clouds, soil moisture, precipitation, and water vapor on diurnal temperature range. *J. Clim.* **12**, 2451–2473 (1999).
47. Wang, Y. et al. Reduced European aerosol emissions suppress winter extremes over northern Eurasia (vol 10, pg 225, 2020). *Nat. Clim. Change* **10**, 582 (2020).
48. Zhu, J. et al. Decrease in radiative forcing by organic aerosol nucleation, climate, and land use change. *Nat. Commun.* **10**, 423 (2019).
49. Twomey, S. Pollution and the planetary albedo. *Atmos. Environ.* **41**, 1251–1256 (1974).
50. Albrecht, B. A. Aerosols, cloud microphysics, and fractional cloudiness. *Science* **245**, 1227–1230 (1989).
51. Perlwitz, J. & Miller, R. L. Cloud cover increase with increasing aerosol absorptivity: a counterexample to the conventional semidirect aerosol effect. *J. Geophys. Res.: Atmos.* **115**, https://doi.org/10.1029/2009JD012637 (2010).
52. Myhre, G. et al. Aerosol-cloud interaction inferred from MODIS satellite data and global aerosol models. *Atmos. Chem. Phys.* **7**, 3081–3101 (2007).
53. Chen, Y. et al. Machine learning reveals climate forcing from aerosols is dominated by increased cloud cover. *Nat. Geosci.* **15**, 609–614 (2022).
54. Kawamoto, K. Relationships between cloud properties and precipitation amount over the Amazon basin. *Atmos. Res.* **82**, 239–247 (2006).
55. Hoerl, A. E. & Kennard, R. W. Ridge regression: biased estimation for nonorthogonal problems. *Technometrics* **12**, 55–67 (1970).
56. Hersbach, H. et al. The ERA5 global reanalysis. *Q. J. R. Meteorological Soc.* **146**, 1999–2049 (2020).
57. Gelaro, R. et al. The modern-era retrospective analysis for research and applications, Version 2 (MERRA-2. *J. Clim.* **30**, 5419–5454 (2017).
58. Martens, B. et al. GLEAM v3: satellite-based land evaporation and root-zone soil moisture. *Geoscientific Model Dev. Discuss.* **10**, 1–36 (2017).
59. Breiman, L. Random Forests. *Mach. Learn.* **45**, 5–32 (2001).
60. Dim, J. R. et al. The recent state of the climate: Driving components of cloud-type variability. *J. Geophysi. Res.-Atmos.* **116**, https://doi.org/10.1029/2010jd014559 (2011).
61. Eastman, R. & Warren, S. G. A 39-Yr survey of cloud changes from land stations worldwide 1971–2009: long-term trends, relation to aerosols, and expansion of the tropical belt. *J. Clim.* **26**, 1286–1303 (2013).
62. Zhong, X. et al. Observed trends in clouds and precipitation (1983–2009): implications for their cause(s). *Atmos. Chem. Phys.* **21**, 4899–4913 (2021).
63. Yang, Y., Lou, S. J., Wang, H. L., Wang, P. Y. & Liao, H. Trends and source apportionment of aerosols in Europe during 1980-2018. *Atmos. Chem. Phys.* **20**, 2579–2590 (2020).
64. Sheffield, J., Wood, E. F. & Roderick, M. L. Little change in global drought over the past 60 years. *Nature* **491**, 435–438 (2012).
65. Zhou, Y., Yan, H. P. & Luo, J. J. Impacts of Amazon Fire Aerosols on the Subseasonal Circulations of the Mid-High Latitudes. *Front. Earth Sci.* **8**, https://doi.org/10.3389/feart.2021.609554 (2021).
66. Makowski, K., Wild, M. & Ohmura, A. Diurnal temperature range over Europe between 1950 and 2005. *Atmos. Chem. Phys.* **8**, 6483–6498 (2008).
67. Feng, R., Yu, R. D., Zheng, H. W. & Gan, M. Spatial and temporal variations in extreme temperature in Central Asia. *Int. J. Climatol.* **38**, E388–E400 (2018).
68. Kothawale, D. R., Kumar, K. K. & Srinivasan, G. Spatial asymmetry of temperature trends over India and possible role of aerosols. *Theor. Appl. Climatol.* **110**, 263–280 (2012).
69. Thorne, P. W. et al. Reassessing changes in diurnal temperature range: Intercomparison and evaluation of existing global data set estimates. *J. Geophys. Res.: Atmos.* **121**, 5138–5158 (2016).
70. Thorne, P. W. et al. Reassessing changes in diurnal temperature range: A new data set and characterization of data biases. *J. Geophys. Res.: Atmos.* **121**, 5115–5137 (2016).
71. Jones, P. The reliability of global and hemispheric surface temperature records. *Adv. Atmos. Sci.* **33**, 269–282 (2016).
72. Xu, W. et al. A new integrated and homogenized global monthly land surface air temperature dataset for the period since 1900. *Clim. Dyn.* **50**, 2513–2536 (2018).
73. Durre, I., Menne, M. J., Gleason, B. E., Houston, T. G. & Vose, R. S. Comprehensive automated quality assurance of daily surface observations. *J. Appl. Meteorol. Climatol.* **49**, 1615–1633 (2010).
74. Zhou, L. et al. Spatial dependence of diurnal temperature range trends on precipitation from 1950 to 2004. *Clim. Dyn.* **32**, 429–440 (2009).
75. Yang, Y. & Ren, R. On the contrasting decadal changes of diurnal surface temperature range between the Tibetan Plateau and southeastern China during the 1980s–2000s. *Adv. Atmos. Sci.* **34**, 181–198 (2017).
76. Jeong, S.-J., Ho, C.-H., Park, T.-W., Kim, J. & Levis, S. Impact of vegetation feedback on the temperature and its diurnal range over the Northern Hemisphere during summer in a 2 × CO2 climate. *Clim. Dyn.* **37**, 821–833 (2011).
77. Zheng, L. et al. Spatial, temporal, and spectral variations in albedo due to vegetation changes in China's grasslands. *Isprs J. Photogramm. Remote Sens.* **152**, 1–12 (2019).
78. Xu, Z., Mahmood, R., Yang, Z.-L., Fu, C. & Su, H. Investigating diurnal and seasonal climatic response to land use and land cover change over monsoon Asia with the Community Earth System Model. *J. Geophys. Res.: Atmospheres* **120**, 1137–1152 (2015).
79. Manatsa, D., Morioka, Y., Behera, S. K., Mushore, T. D. & Mugandani, R. Linking the southern annular mode to the diurnal temperature range shifts over southern Africa. *Int. J. Climatol.* **35**, 4220–4236 (2015).
80. Grant, L. et al. Biogeophysical Effects of Land-Use and Land-Cover Change Not Detectable in Warmest Month. *J. Clim.* **36**, 1845–1861 (2023).
81. Williams, C. A., Gu, H. & Jiao, T. Climate impacts of U.S. forest loss span net warming to net cooling. *Sci. Adv.* **7**, eaax8859 (2021).
82. Norris, J. R. et al. Evidence for climate change in the satellite cloud record. *Nature* **536**, 72–75 (2016).
83. Ceppi, P. & Nowack, P. Observational evidence that cloud feedback amplifies global warming. *Proc. Natl Acad. Sci. USA* **118**, e2026290118 (2021).
84. Zeng, Z. et al. A reversal in global terrestrial stilling and its implications for wind energy production. *Nat. Clim. Change* **9**, 979–985 (2019).
85. Nasa/Larc/Sd/Asdc. (2019).

86. Hair, J. F., Black, W. C., Babin, B. J. & Anderson, R. E. *Multivariate Data Analysis (7th Edition)*. 200 (Pearson 2009).
87. Markus, M. T. & Groenen, P. J. F. An introduction to the bootstrap. *Psychometrika* **63**, 97–101 (1998).
88. Zhong, Z., He, B., Chen, H. W. & Chen, D. Reversed asymmetric warming of sub-diurnal temperature over land during recent decades. Data sets. figshare., https://doi.org/10.6084/m9.figshare.24310699.v1 (2023).

Acknowledgements

This work has been supported by the Third Xinjiang Scientific Expedition Program (GrantNo.2022xjkk0106) and the State Key Laboratory of Earth Surface Processes and Resource Ecology. H.W.C. was supported by the Swedish Foundation for International Cooperation in Research and Higher Education (CH2020-8799).

Author contributions

B.H. and Z.Z. designed research; Z.Z. performed the analysis and wrote the paper; H.W.C., D.C., and T.Z. provided comments to improve the manuscript; B.H. supervised the project. W.D., C.X., S.X., X.S., L.G., R.D., L.Z., L.H., W.Y., X.H., D.J., and X.Z. offered thoughts on the analysis and contributed to the writing.

Competing interests

The authors declare no competing interests.

Additional information

Supplementary information The online version contains supplementary material available at https://doi.org/10.1038/s41467-023-43007-6.

Correspondence and requests for materials should be addressed to Bin He.

Peer review information *Nature Communications* thanks the anonymous reviewers for their contribution to the peer review of this work. A peer review file is available.

Diurnally asymmetric warming has amplified atmospheric dryness since the 1980s

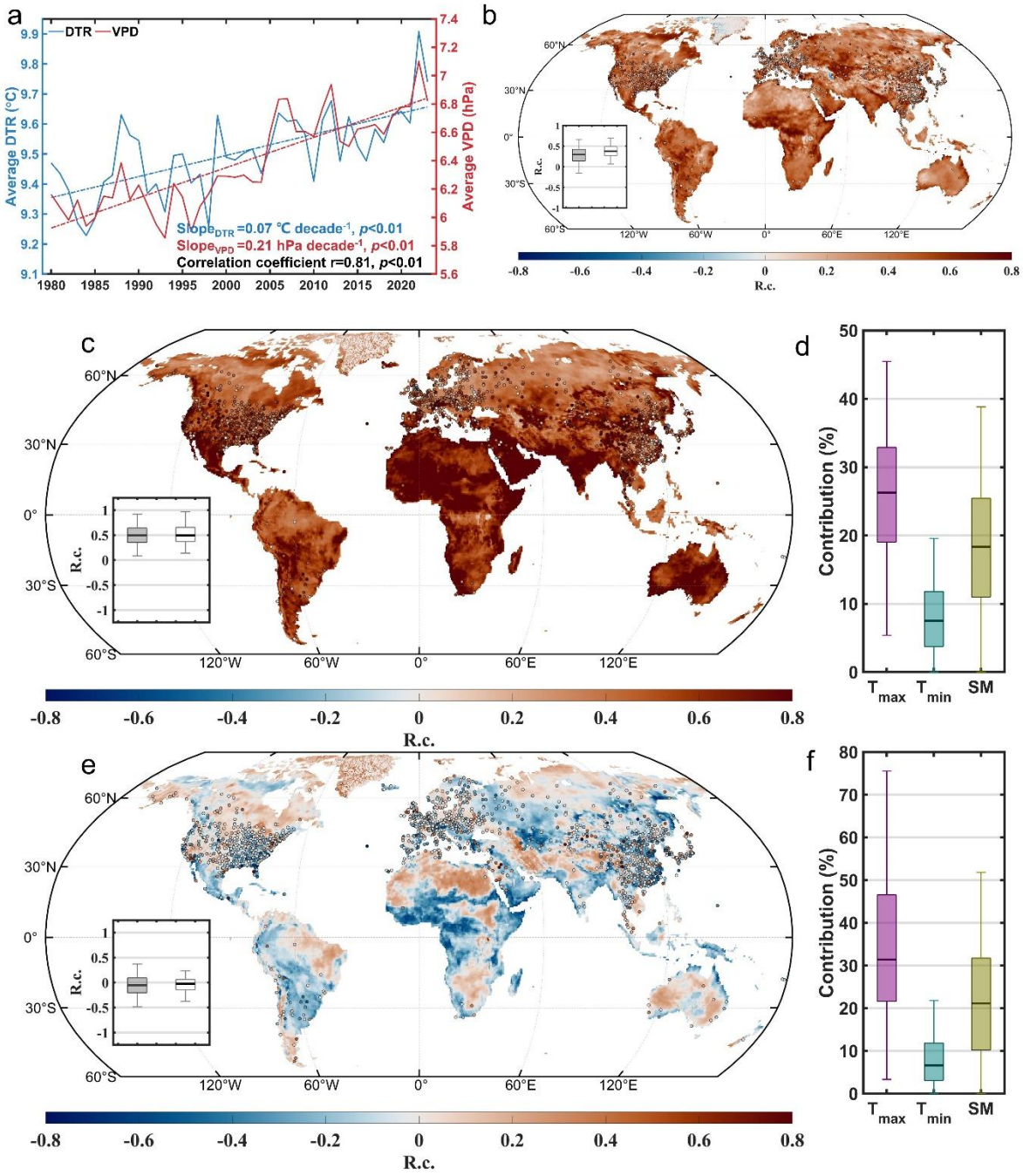

Fig. 1: Diurnally asymmetric warming and its impact on vapor pressure deficit (VPD) from 1980 to 2023. a, Variations and changes in annual average VPD and diurnal temperature range (DTR) averaged over all stations (dots in **b**, **c** and **e**). The dashed lines show the linear trends obtained from linear regressions. **b**, Spatial distribution of ridge regression coefficients (R.c., see Methods) of VPD with respect to DTR, with DTR, soil moisture (SM), and mean air temperature as independent variables. **c**, **e**, Spatial distribution of R.c. of annual average VPD

with respect to annual average daily maximum temperature (T_{max}, **c**) and daily minimum temperature (T_{min}, **e**), with T_{max}, T_{min} and SM as independent variables. All variables in the ridge regressions are detrended annual averages. The insets in **b**, **c** and **e** show the R.c. across different stations (solid box) and ERA5-Land grid points (hollow box) with boxplots. **d**, **f**, Assessment of the contributions of interannual T_{max}, T_{min}, and SM to the variations in interannual VPD across different stations (**d**) and ERA5-Land grid points (**f**). In the station-based regression, we used SM from the ERA5-Land dataset at the station sites. Only the stations or grid points with regression results that passed the test of significance (p<0.05) were included in the analysis and are shown. In all boxplots, the height of each box represents the interquartile, with the thick black line indicating the median, and the edges denoting the first and third quartiles. Whiskers extend to the 2.5th and 97.5th percentiles.

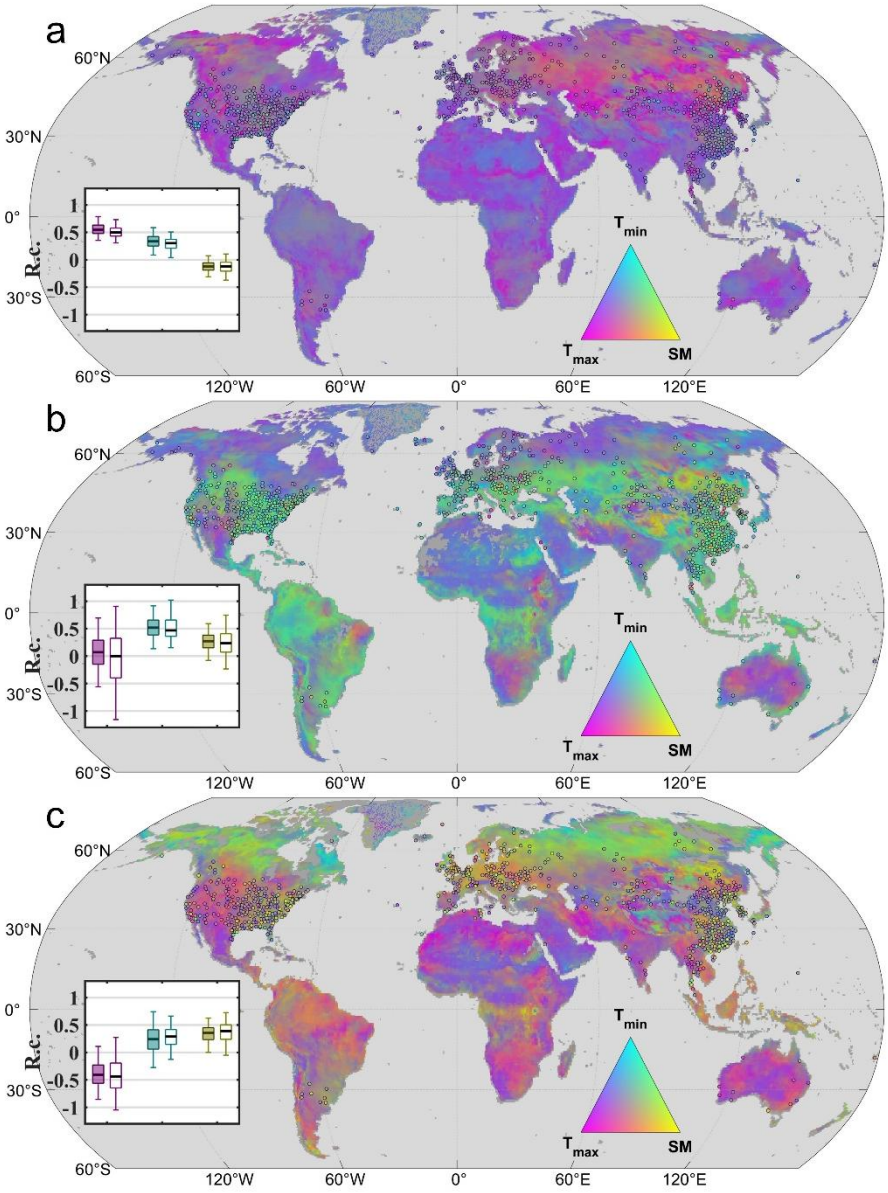

Fig. 2: Contributions of daily maximum temperature (T_{max}), daily minimum temperature (T_{min}) and soil moisture (SM) to saturated vapor pressure (SVP), actual vapor pressure (AVP) and relative humidity (RH) from 1980 to 2023. The cyan-magenta-yellow (CMY) composites[26] show the contributions of T_{max} (magenta), T_{min} (cyan) and SM (yellow) to SVP (**a**), AVP (**b**) and RH (**c**) variations on the interannual timescale (long-term trends removed). The color of the composite was determined by the relative magnitude of the ridge regression coefficients (R.c.) for each independent variable. The insets show the R.c. across different stations (solid boxes) or ERA5-Land grid points (hollow boxes) with boxplots. In the station-based regression, we used SM from the ERA5-Land dataset at the station sites. In all boxplots, the height of each box represents the interquartile range of R.c. across different stations or grid points, with the thick black line indicating the median, and the edges denoting the first and third quartiles. Whiskers extend to the 2.5th and 97.5th percentiles. Only the stations with regression results that passed the test of significance (p<0.05) were included in the analysis and are shown.

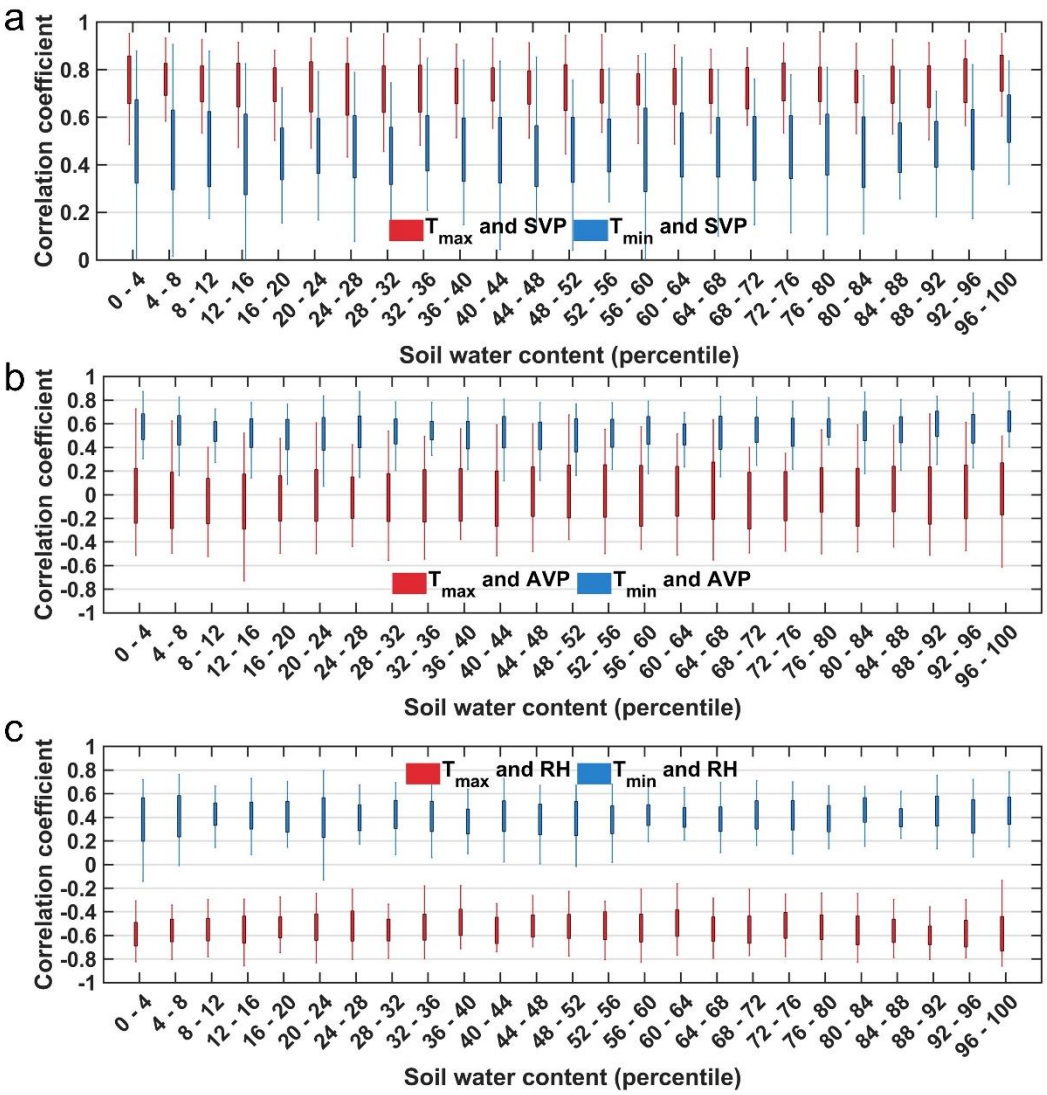

Fig. 3: Asymmetric effects of daily maximum temperature (T_{max}) and daily minimum temperature (T_{min}) on saturated vapor pressure (SVP), actual vapor pressure (AVP) and relative humidity (RH). Assessment of the partial correlation between T_{max} or T_{min} and SVP (**a**), AVP (**b**), and RH (**c**) while controlling for the other variable across different soil water content percentiles at all FLUXNET sites. The height of each box represents the interquartile range of correlation coefficients across different stations, with the edges denoting the first and third quartiles. Whiskers extend to the 2.5th and 97.5th percentiles of correlation coefficient.

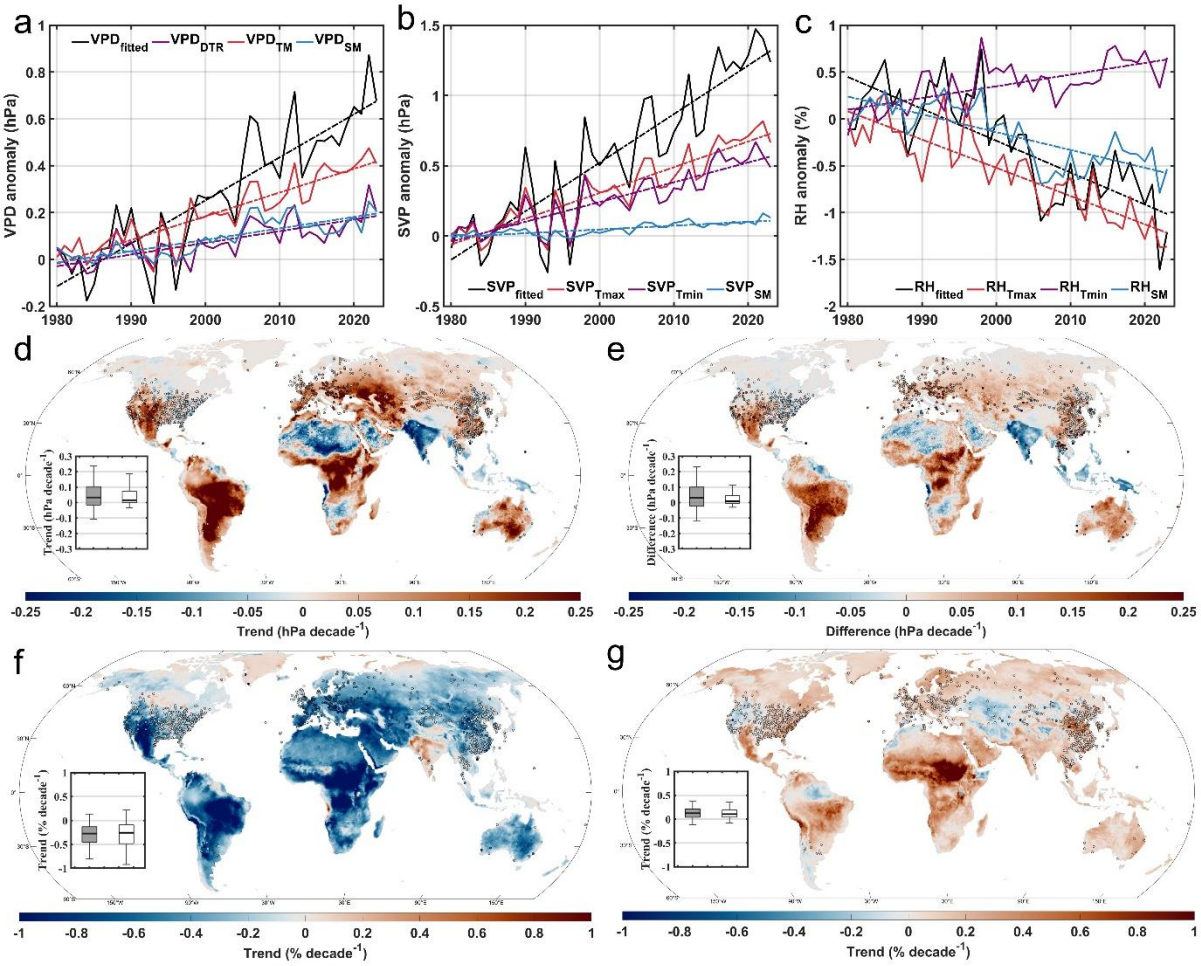

Fig. 4: Contribution of sub-diurnal asymmetric warming to trends in saturated vapor pressure (SVP), relative humidity (RH) and vapor pressure deficit (VPD) from 1980 to 2023. **a**–**c**, Variations and changes in the annual average model-fitted (subscript fitted) VPD (**a**), SVP (**b**), and RH (**c**), and the contributions of diurnal temperature range (subscript DTR), mean temperature (subscript TM), and soil moisture (subscript SM) to the variations and changes over land. The model-fitted values are anomalies calculated by subtracting the mean values for the control period (1980–1982). The dashed lines show the linear trends obtained from linear regressions. **d**, **f** and **g**, Spatial distribution of trends in VPD_{DTR} (**d**), RH_{Tmax} (**f**) and RH_{Tmin} (**g**). **e**, Spatial distribution of differences between trends in SVP_{Tmax} and SVP_{Tmin}. The insets show the trends or differences across different stations (solid box) or grid points (hollow box) with boxplots. In all boxplots, the height of each box represents the interquartile range of trends or differences across different stations or grid points, with the thick black line indicating the median, and the edges denoting the first and third quartiles. Whiskers extend to the 2.5th and 97.5th percentiles.

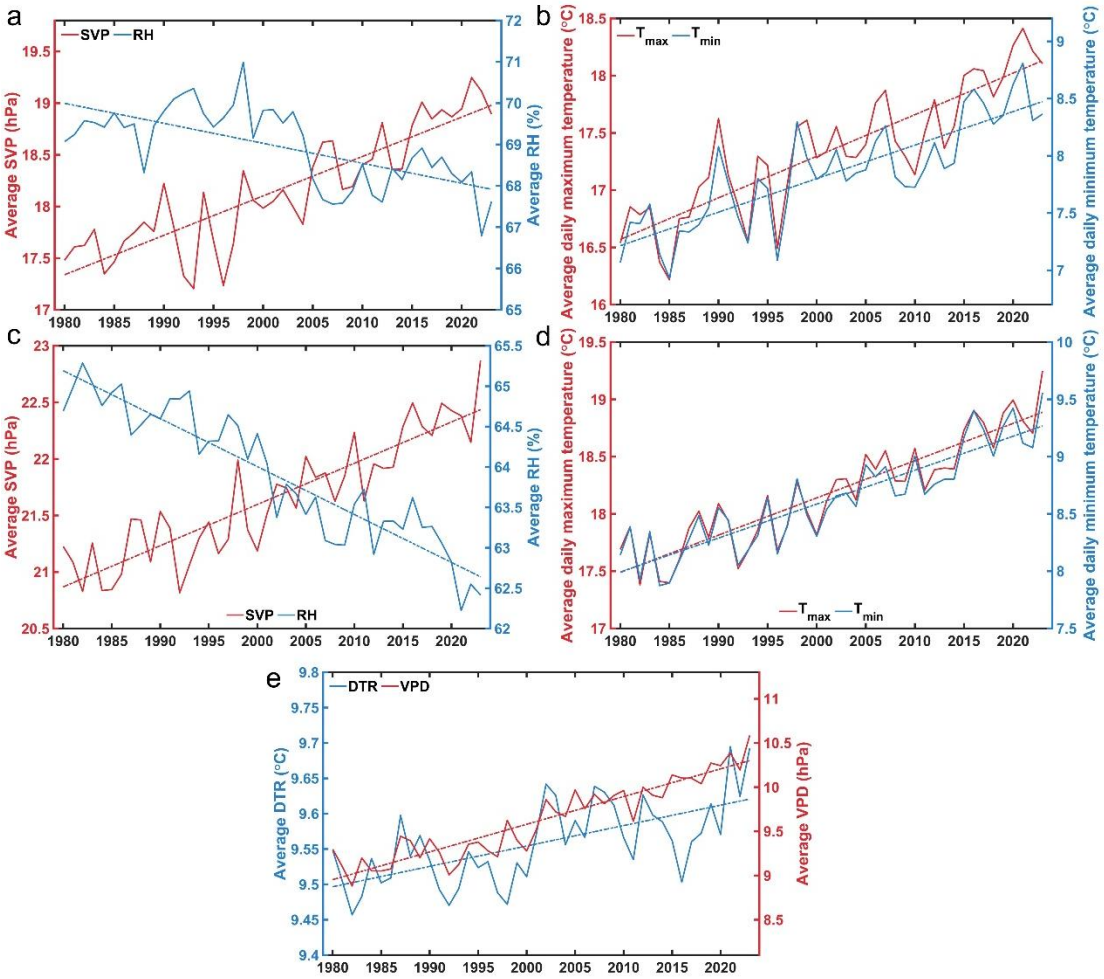

Supplementary Figure 1. Variations and changes in annual average saturated vapor pressure (SVP), relative humidity (RH), daily maximum temperature (T_{max}), daily minimum temperature (T_{min}), vapor pressure deficit (VPD) and diurnal temperature range (DTR) over land areas during 1980–2023. a, **b**, Variations and changes in annual average SVP and RH (**a**) and T_{max} and T_{min} (**b**) across all stations. **c**–**e**, Variations and changes in annual area-weighted average SVP and RH (**c**), T_{max} and T_{min} (**d**), and DTR and VPD (**e**) derived from the ERA5-Land dataset.

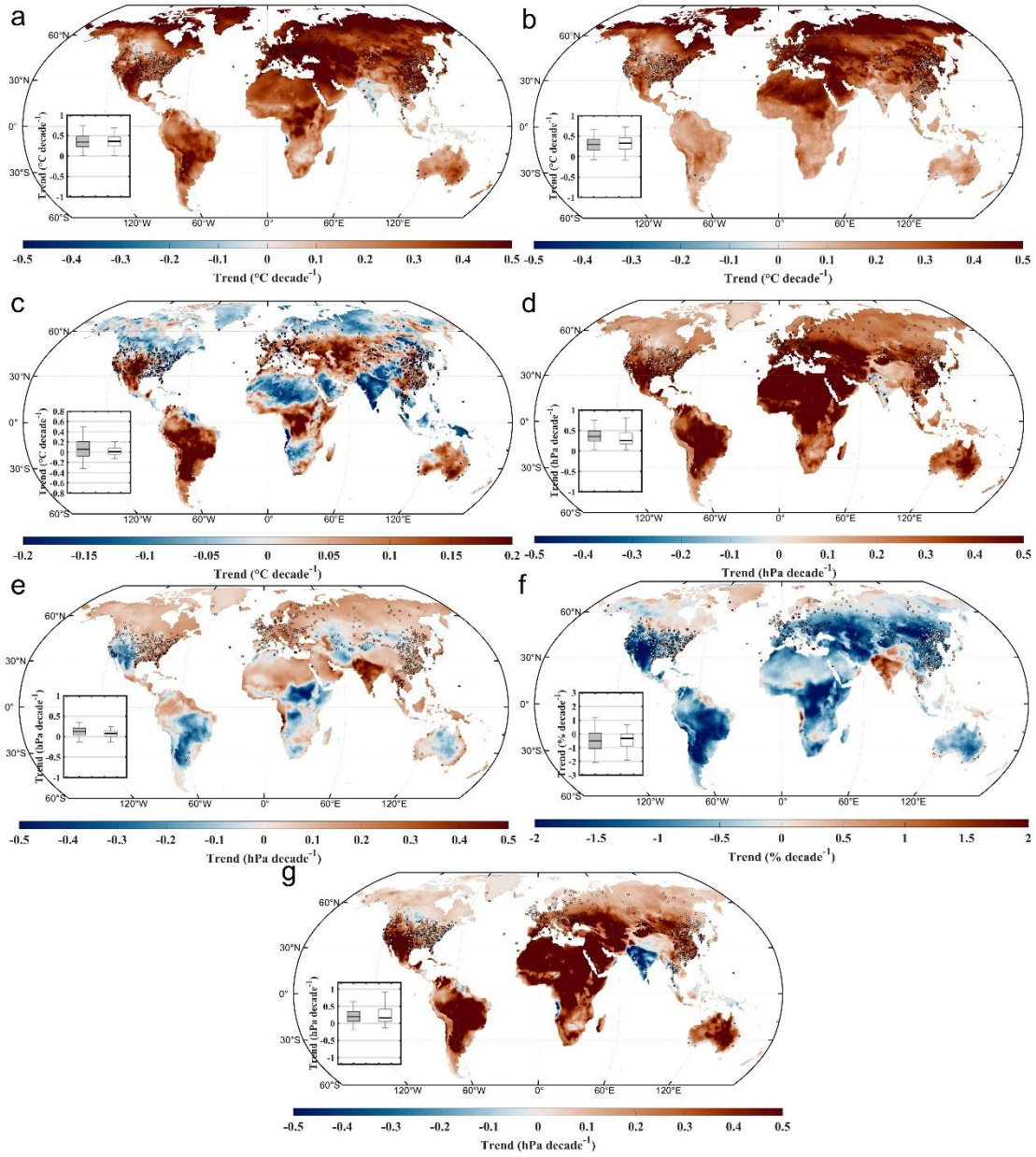

Supplementary Figure 2. Spatial distribution of the trend in temperature and humidity variables during 1980–2023. Trend in annual average daily maximum temperature (**a**), daily minimum temperature (**b**), diurnal temperature range (**c**), saturated vapor pressure (**d**), actual vapor pressure (**e**), relative humidity (**f**), and vapor pressure deficit (**g**) over land areas during 1980–2022**.** The insets show the trends across different stations (solid box) or grid points (hollow box) with a boxplot. The height of each box represents the interquartile range of trend across different stations or grids, with the thick black line indicating the median, and the edges denoting the first and third quartiles. Whiskers extend to the 2.5th and 97.5th percentiles.

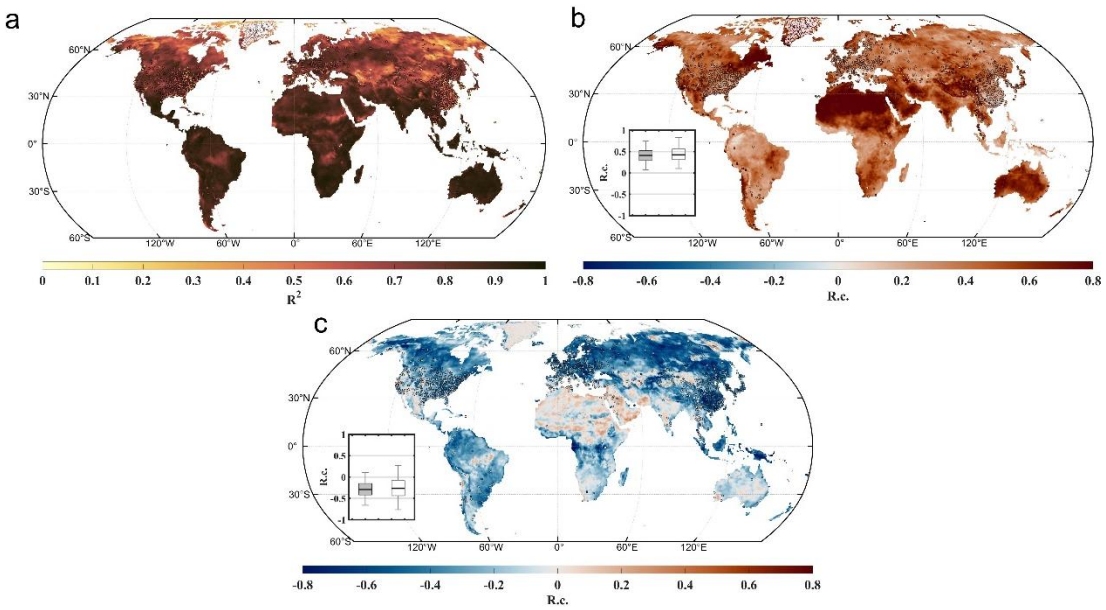

Supplementary Figure 3. Impact of mean air temperature and soil moisture on vapor pressure deficit (VPD) on the interannual scale during 1980–2023. a, Spatial distribution of determination coefficients (R^2) of the ridge regression model, with VPD as dependent variable and diurnal temperature range, mean air temperature and soil moisture as independent variables. **b** and **c**, Spatial distribution of ridge regression coefficients (R.c.) of detrended annual VPD with respect to mean air temperature (**b**) and soil moisture (**c**). The insets show the R.c. across different stations (solid box) or grids (hollow box) with boxplots. The height of each box represents the interquartile range of R.c. across different stations or grids, with the thick black line indicating the median, and the edges denoting the first and third quartiles. Whiskers extend to the 2.5th and 97.5th percentiles. Only the stations or grids with the regression result that passed the test of significance ($p<0.05$) were included in the analysis and are shown.

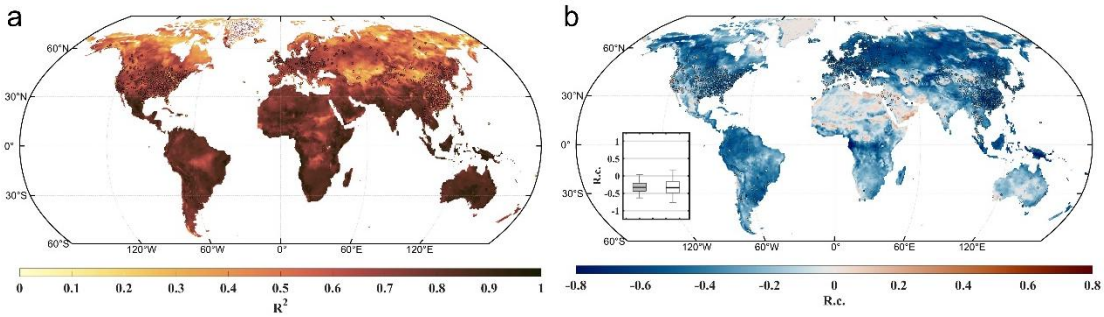

Supplementary Figure 4. Impact of soil moisture on vapor pressure deficit (VPD) on the interannual scale during 1980–2023. a, Spatial distribution of determination coefficients (R^2) of the ridge regression model, with VPD as dependent variable and daily maximum temperature, daily minimum temperature and soil moisture as independent variables**. b**, Spatial distribution of ridge regression coefficients (R.c.) of detrended annual VPD with respect to soil moisture. The inset show the R.c. across different stations (solid box) or grids (hollow box) with a boxplot. The height of each box represents the interquartile range of R.c. across different stations or grids, with the thick black line indicating the median, and the edges denoting the first and third quartiles. Whiskers extend to the 2.5th and 97.5th percentiles. Only the stations or grids with the regression result that passed the test of significance ($p<0.05$) were included in the analysis and are shown.

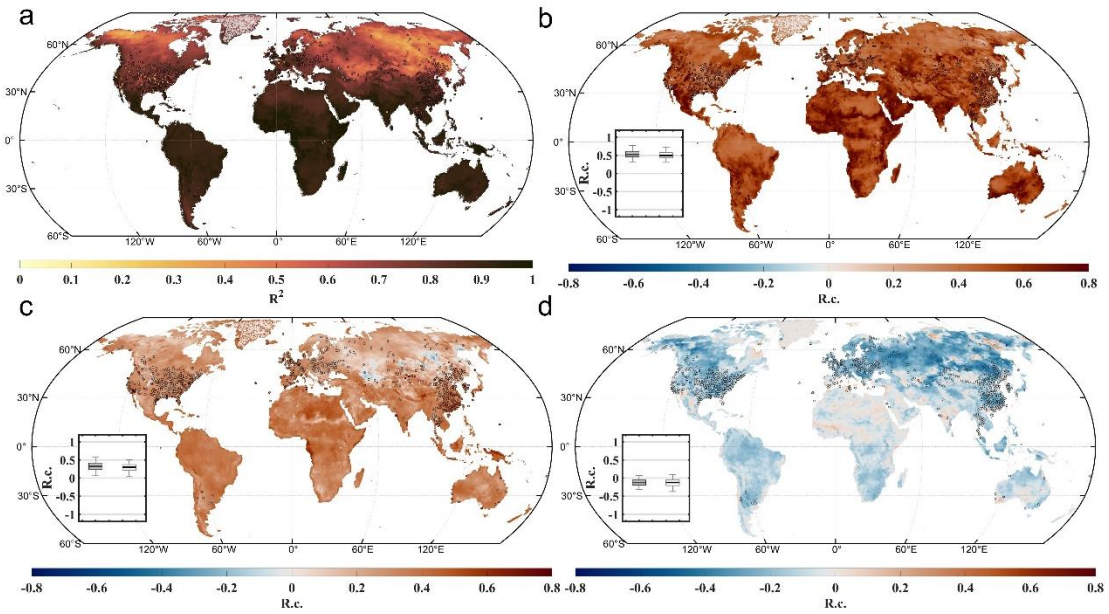

Supplementary Figure 5. Impact of daily maximum temperature (T_{max}), daily minimum temperature (T_{min}) and soil moisture (SM) on saturated vapor pressure (SVP) on the interannual scale during 1980–2023. a, Spatial distribution of determination coefficients (R^2) of the ridge regression model, with SVP as the dependent variable and T_{max}, T_{min}, and SM as independent variables. **b** and **c**, Spatial distribution of ridge regression coefficients (R.c.) of detrended annual SVP with respect to T_{max} (**b**), T_{min} (**c**) and SM (**d**). The insets show the R.c. across different stations (solid box) or grids (hollow box) with boxplots. The height of each box represents the interquartile range of R.c. across different stations or grids, with the thick black line indicating the median, and the edges denoting the first and third quartiles. Whiskers extend to the 2.5th and 97.5th percentiles. Only the stations or grids with the regression result that passed the test of significance ($p<0.05$) were included in the analysis and are shown.

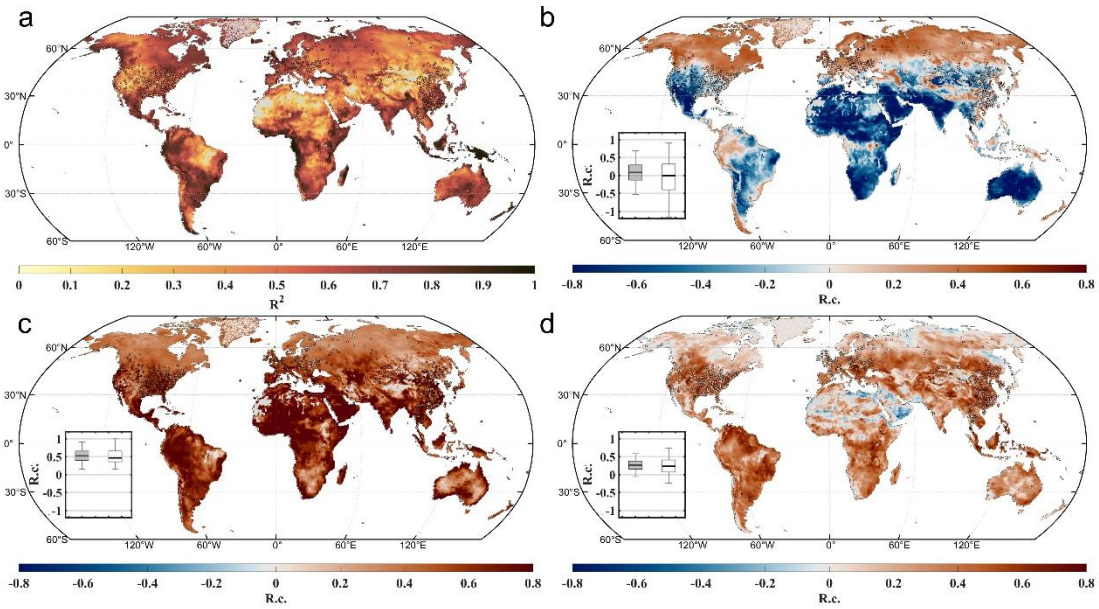

Supplementary Figure 6. Impact of daily maximum temperature (T_{max}), daily minimum temperature (T_{min}) and soil moisture (SM) on actual vapor pressure (AVP) on the interannual scale during 1980-2023. a, Spatial distribution of determination coefficients (R^2) of the ridge regression model, with AVP as the dependent variable and T_{max}, T_{min}, and SM as independent variables. **b** and **c**, Spatial distribution of ridge regression coefficients (R.c.) of detrended annual AVP with respect to T_{max} (**b**), T_{min} (**c**), and SM (**d**). The insets show the R.c. across different stations (solid box) or grids (hollow box) with boxplots. The height of each box represents the interquartile range of R.c. across different stations or grids, with the thick black line indicating the median, and the edges denoting the first and third quartiles. Whiskers extend to the 2.5th and 97.5th percentiles. Only the stations or grids with the regression result that passed the test of significance ($p<0.05$) were included in the analysis and are shown.

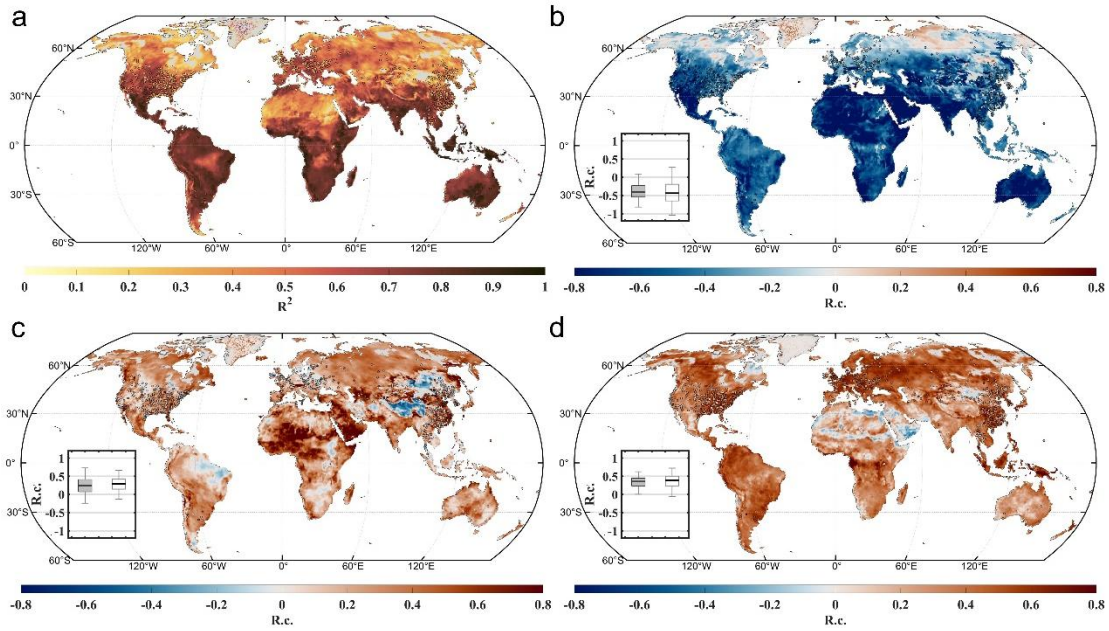

Supplementary Figure 7. Impact of daily maximum temperature (T_{max}), daily minimum temperature (T_{min}) and soil moisture (SM) on relative humidity (RH) on the interannual scale during 1980–2023. a Spatial distribution of determination coefficients (R^2) of the ridge regression model, with RH as the dependent variable and T_{max}, T_{min}, and SM as independent variables. **b** and **c**, Spatial distribution of ridge regression coefficients (R.c.) of detrended annual RH with respect to T_{max} (**b**), T_{min} (**c**), and SM (**d**). The insets show the R.c. across different stations (solid box) or grids (hollow box) with boxplots. The height of each box represents the interquartile range of R.c. across different stations or grids, with the thick black line indicating the median, and the edges denoting the first and third quartiles. Whiskers extend to the 2.5th and 97.5th percentiles. Only the stations or grids with the regression result that passed the test of significance ($p<0.05$) were included in the analysis and are shown.

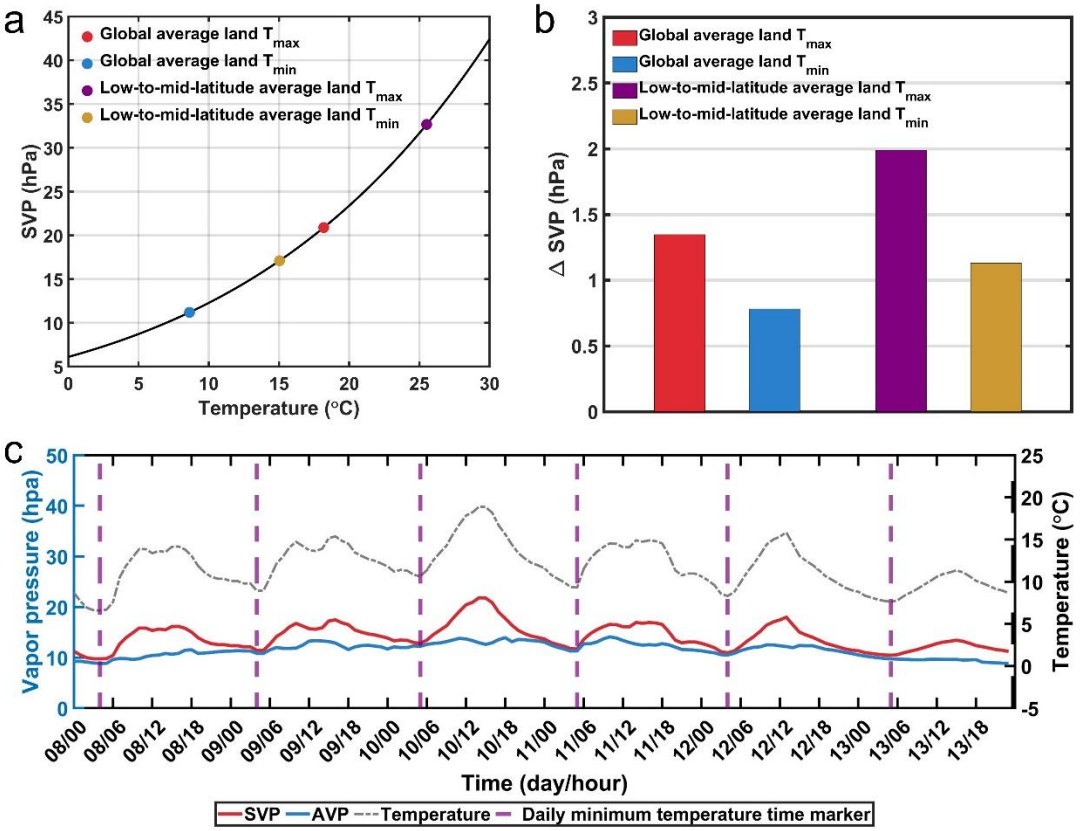

Supplementary Figure 8. The impact of daily maximum temperature (T_{max}) and daily minimum temperature (T_{min}) on saturated vapor pressure (SVP) and actual vapor pressure (AVP). a, The relationship between SVP and temperature. The points on the curve indicate the global area-weighted average land T_{max} and T_{min}, as well as the low-to-mid-latitude (between 45°S and 45°N) area-weighted average land T_{max} and T_{min} during 1980–2023. **b**, Changes in SVP (ΔSVP) due to a 1°C increase at different temperature conditions indicated in (a). **c**, Demonstration of how T_{min} limits the changes in AVP. The graph shows variations in vapor pressure (SVP and AVP; left y-axis) and temperature (right y-axis) at 45°N, 5°E from May 8 to May 13, 2010 (UTC time). Despite fluctuations in temperature and SVP, AVP is constrained by the T_{min} values during this period. All temperature and humidity variables were derived from the ERA5-Land dataset.

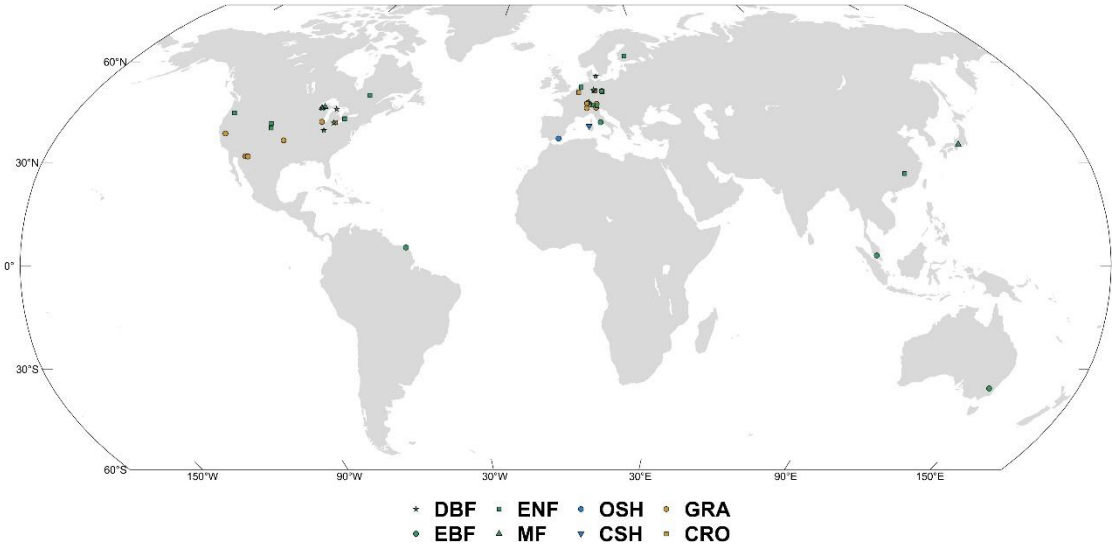

Supplementary Figure 9. Spatial distribution of FLUXNET tower sites. The biomes include evergreen needleleaf forest (ENF), evergreen broadleaf forest (EBF), deciduous broadleaf forest (DBF), mixed forest (MF), closed shrub (CSH), open shrub (OSH), grassland (GRA) and cropland (CRO).

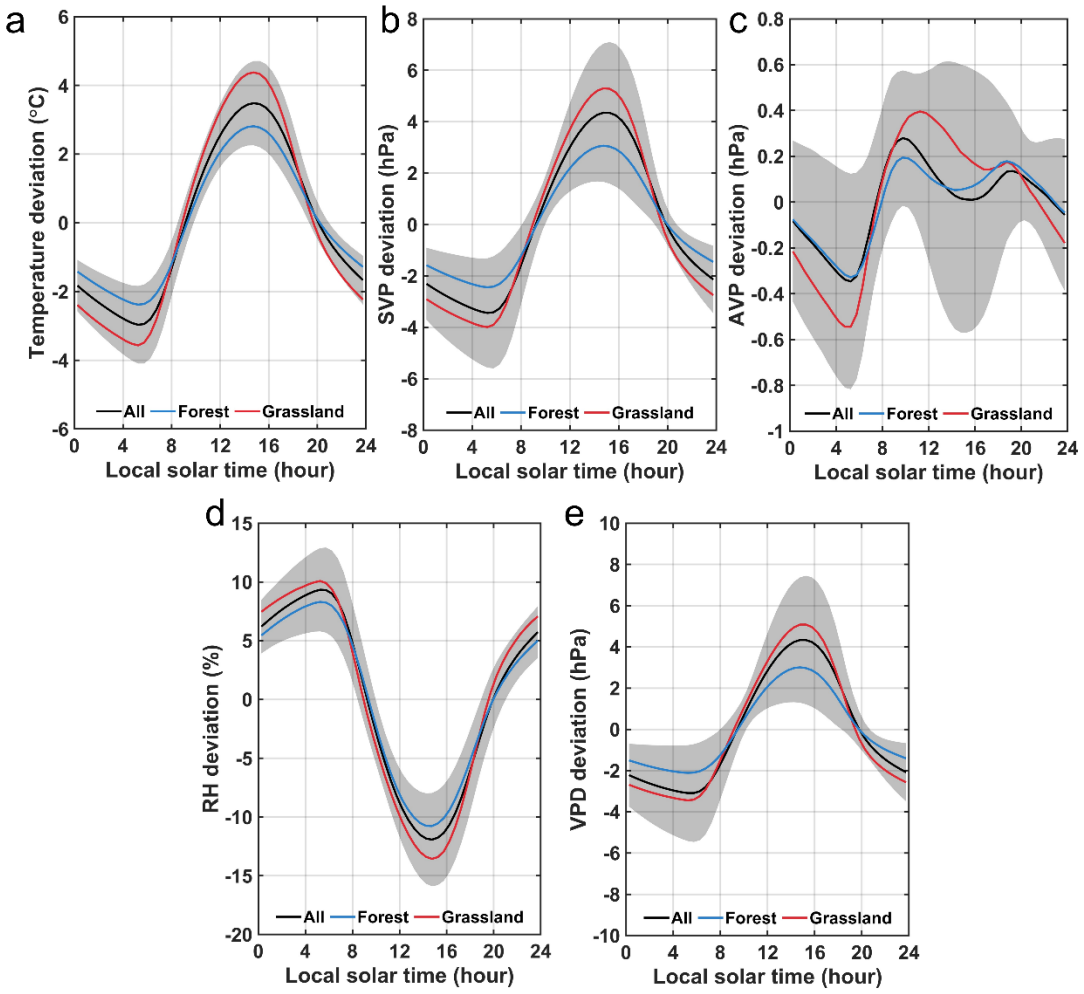

Supplementary Figure 10. Diurnal variations in temperature and humidity variables across FLUXNET tower sites. Averaged annual diurnal variations in temperature (**a**), saturated vapor pressure (SVP, **b**), actual vapor pressure (AVP, **c**), relative humidity (RH, **d**) and vapor pressure deficit (VPD, **e**) across all 56 sites. The y-axis represents the annual-average half-hourly variable deviations from the daily mean. The black thick lines represent the mean value and the shading the standard deviation around the mean for all sites. The blue and red thick lines represent the mean value for 32 forest sites and 12 grassland sites, respectively.

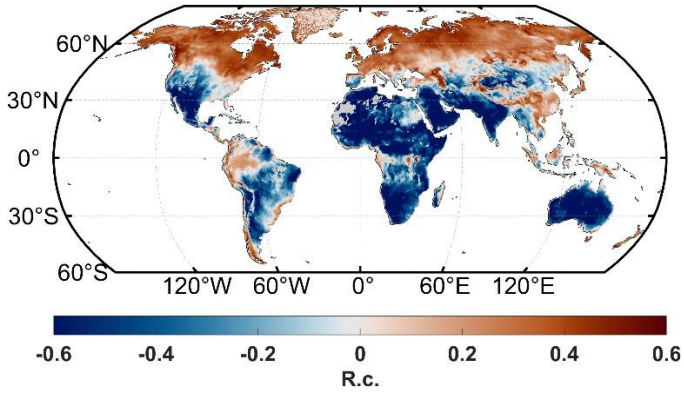

Supplementary Figure 11. Impact of daily maximum temperature (T_{max}) on actual vapor pressure (AVP) on the interannual scale during 1980–2023. a, Spatial distribution of determination coefficients (R^2) of the ridge regression model, with AVP as the dependent variable and T_{max}, daily minimum temperature, soil moisture and surface incoming solar radiation as independent variables. Only the stations or grids with the regression result that passed the test of significance ($p<0.05$) were included in the analysis and are shown.

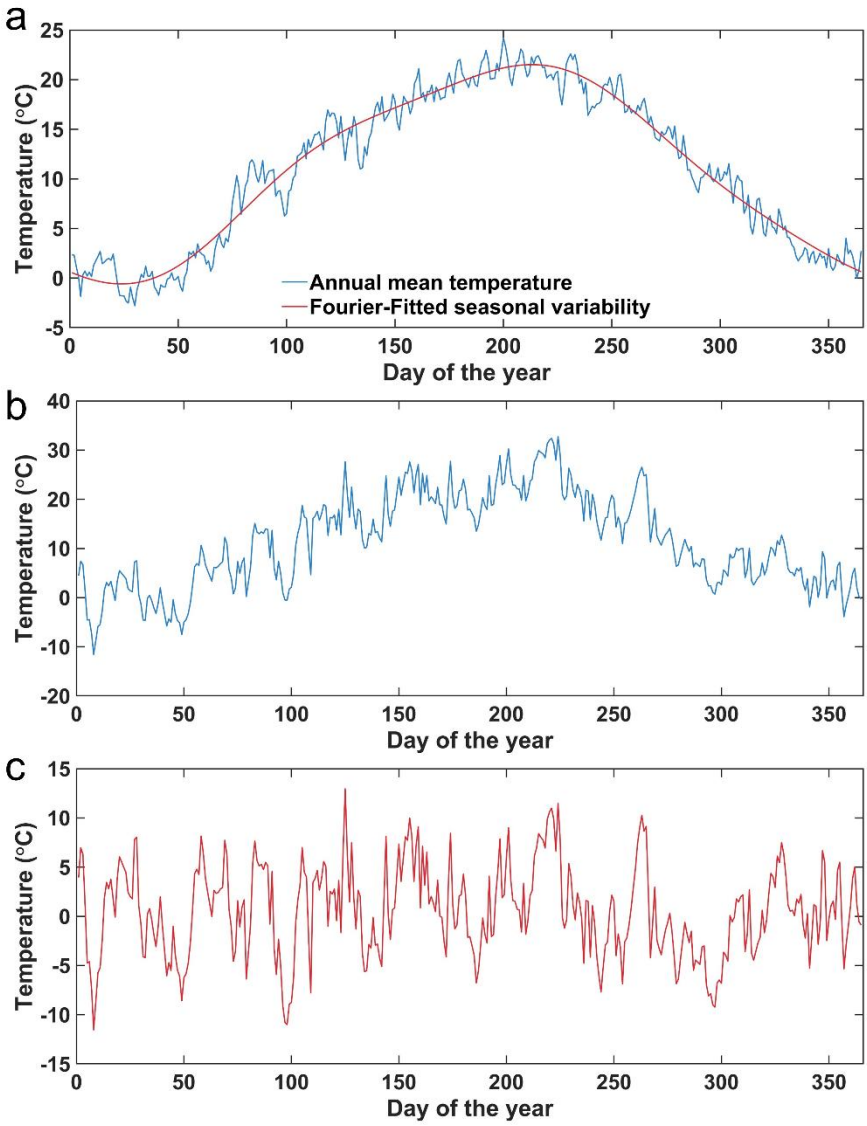

Supplementary Figure 12. Deseasonalization process for the seasonality of daily observations at FLUXNET sites. a, Mean daily maximum temperature across all years and its seasonal variation derived using Fast Fourier Transform. **b**, Daily maximum temperature observation series for the year 2003. **c**, Deseasonalized daily maximum temperature series for the year 2003 obtained after removing the seasonal cycle. The example station is Leinefelde (DE-Lnf), located at 51.33°N, 10.37°E.

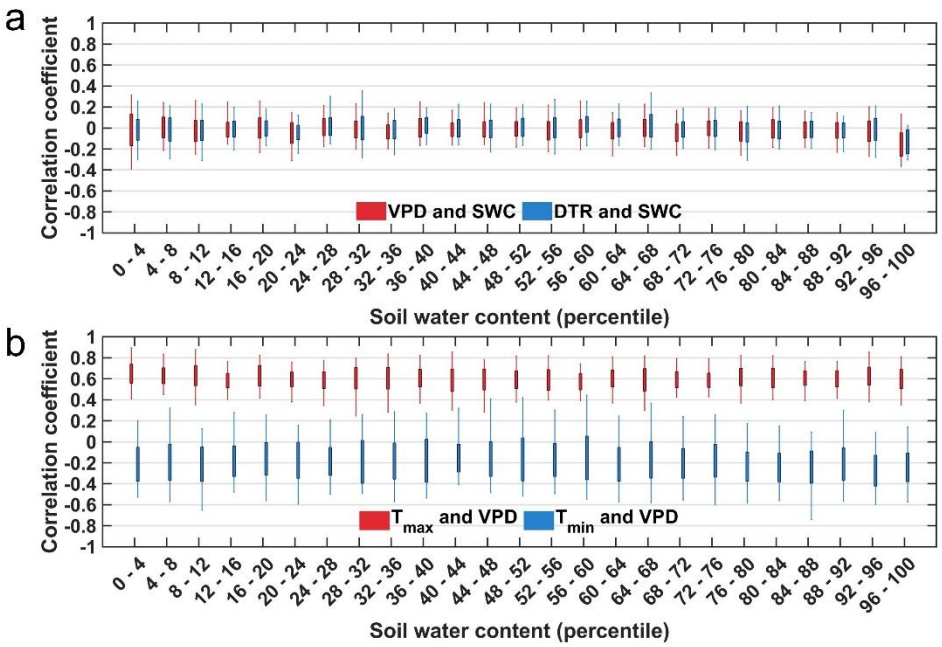

Supplementary Figure 13. Correlation between temperature and humidity variables across different soil water content (SWC) percentiles across FLUXNET sites. a, Assessment of the correlation between saturated SWC and vapor pressure deficit (VPD) or diurnal temperature range (DTR) across different soil water content percentiles at all stations. **b**, Assessment of the partial correlation between daily maximum temperature (T_{max}) or daily minimum temperature (T_{min}) and VPD while controlling for the other variable across different soil water content percentiles at all stations. The height of each box represents the interquartile range of correlation coefficients across different stations, with the edges denoting the first and third quartiles. Whiskers extend to the 2.5th and 97.5th percentiles of the correlation coefficient.

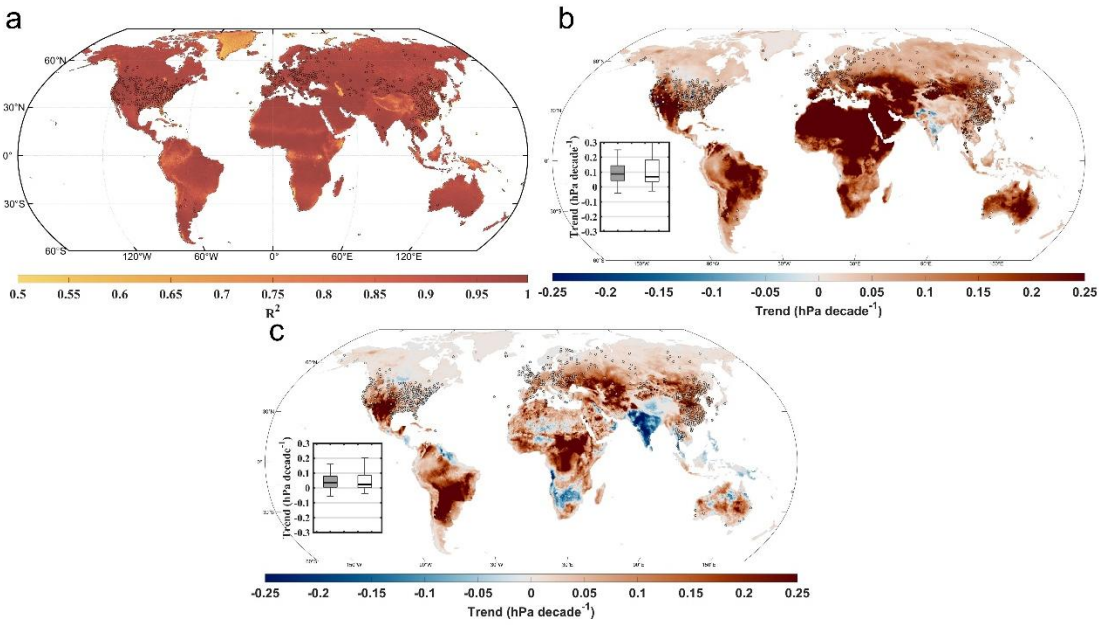

Supplementary Figure 14. Contribution of change in mean temperature and soil moisture to change in vapor pressure deficit (VPD) during 1980–2023. a, Spatial distribution of determination coefficients (R^2) of the random forest regression model in the validation dataset, with VPD as dependent variable and diurnal temperature range, mean air temperature and soil moisture as independent variables. **b** and **c**, Spatial distribution of trends in contribution of mean temperature (**b**) and soil moisture (**c**) to VPD change. The insets show the trends across different stations (solid box) or grids (hollow box) with boxplots. In all boxplots, the height of each box represents the interquartile range of trend across different stations or grids, with the thick black line indicating the median, and the edges denoting the first and third quartiles. Whiskers extend to the 2.5th and 97.5th percentiles.

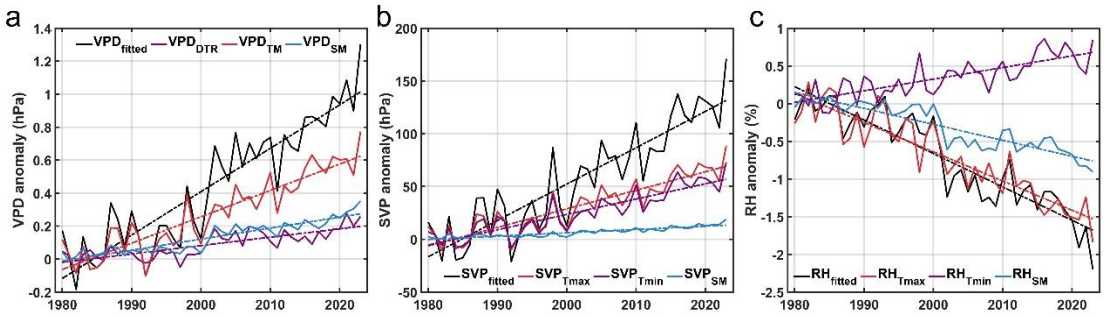

Supplementary Figure 15. Contribution of daily maximum temperature (T_{max}), daily minimum temperature (T_{min}) and soil moisture (SM) to trends in saturated vapor pressure (SVP), relative humidity (RH) and vapor pressure deficit (VPD) from 1980 to 2023 derived from the ERA5-Land dataset. Variations and changes in the annual average model-fitted (subscript fitted) VPD (**a**), SVP (**b**), and RH (**c**), and the contributions of T_{max} (subscript T_{max}), T_{min} (subscript T_{min}), and soil moisture (subscript SM) to the variations and changes over land. The model-fitted values are anomalies calculated by subtracting the mean values for the control period (1980–1982). The dashed lines show the linear trends obtained from linear regressions.

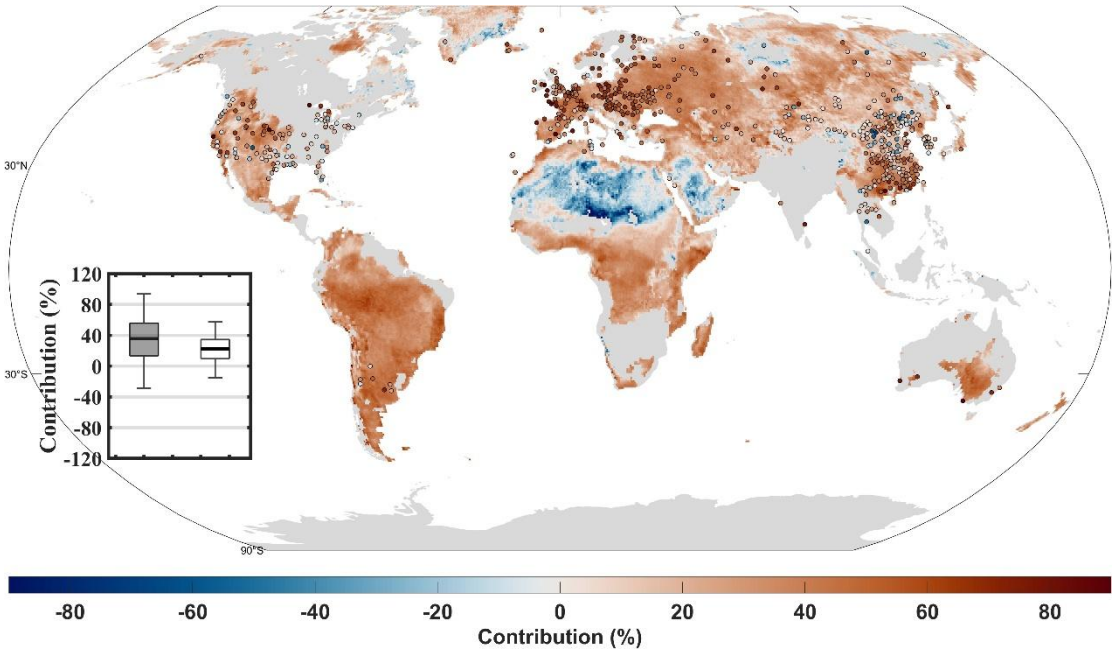

Supplementary Figure 16. Contribution rate of diurnal temperature range (DTR) change to vapor pressure deficit (VPD) increase during 1980–2023. The contribution rate is defined as the ratio of the trend in the contribution of DTR to VPD change to the trend in VPD. The insets show the contribution rate across different stations (solid box) or grids (hollow box) with boxplots. In all boxplots, the height of each box represents the interquartile range of contribution rate across different stations or grids, with the thick black line indicating the median, and the edges denoting the first and third quartiles. Whiskers extend to the 2.5th and 97.5th percentiles. Only sites or grid cells where model-simulated VPD exhibited a significant ($p<0.05$) increase are included in the analysis and shown

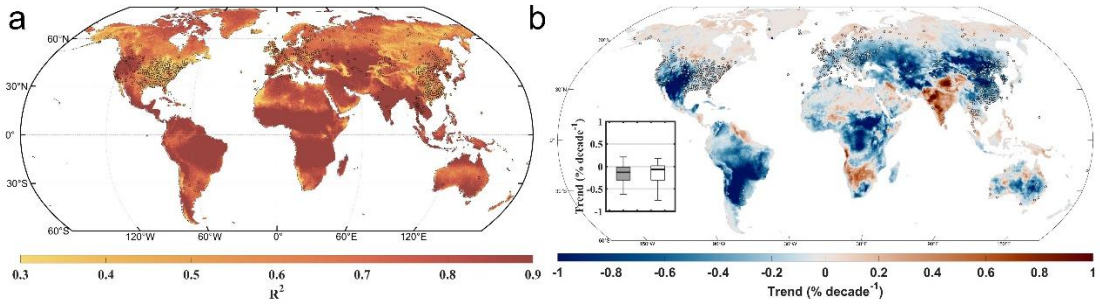

Supplementary Figure 17. Contribution of change in soil moisture (SM) to change in relative humidity (RH) during 1980–2023. a, Spatial distribution of determination coefficients (R^2) of the random forest regression model in the validation dataset, with RH as dependent variable and daily maximum temperature, daily minimum temperature and SM independent variables. **b**, Spatial distribution of trends in contribution of SM to RH change. The inset show the trends across different stations (solid box) or grids (hollow box) with a boxplot. The height of each box represents the interquartile range of trend across different stations or grids, with the thick black line indicating the median, and the edges denoting the first and third quartiles. Whiskers extend to the 2.5th and 97.5th percentiles.

Contrasting vegetation productivity responses in arid and humid zones to recent changes in diurnal temperature range

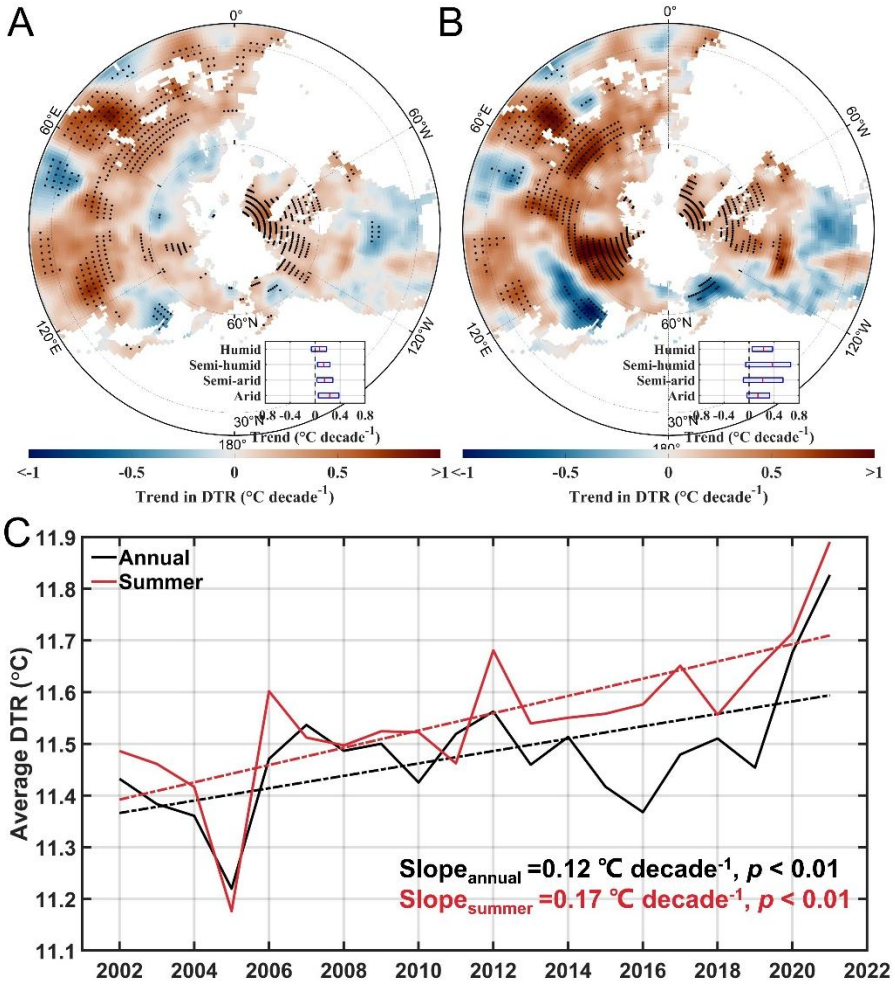

Figure 1. Trend in diurnal temperature range (DTR) in extratropical Northern Hemisphere. (A and B) Spatial distribution of the trend in annual (A) and summer (B) DTR during 2002–2021. The black dots mark the areas where the trends are significant at the p<0.1 level. The insets show the DTR trends in humid, semi-humid, semi-arid, and arid zones with a boxplot. The width of each box indicates the interquartile range of the trends for all grid points, the red line within each box represents the median, and the left and right edges of the box indicate the first and third quartiles, respectively. The spatial distribution of the four climate zones is illustrated in Figure S1A. (C) Variations and changes in area-averaged annual and summer DTR over land in the extratropical Northern Hemisphere from 2002 to 2021. The dashed lines show the linear trends in DTR obtained from linear regressions.

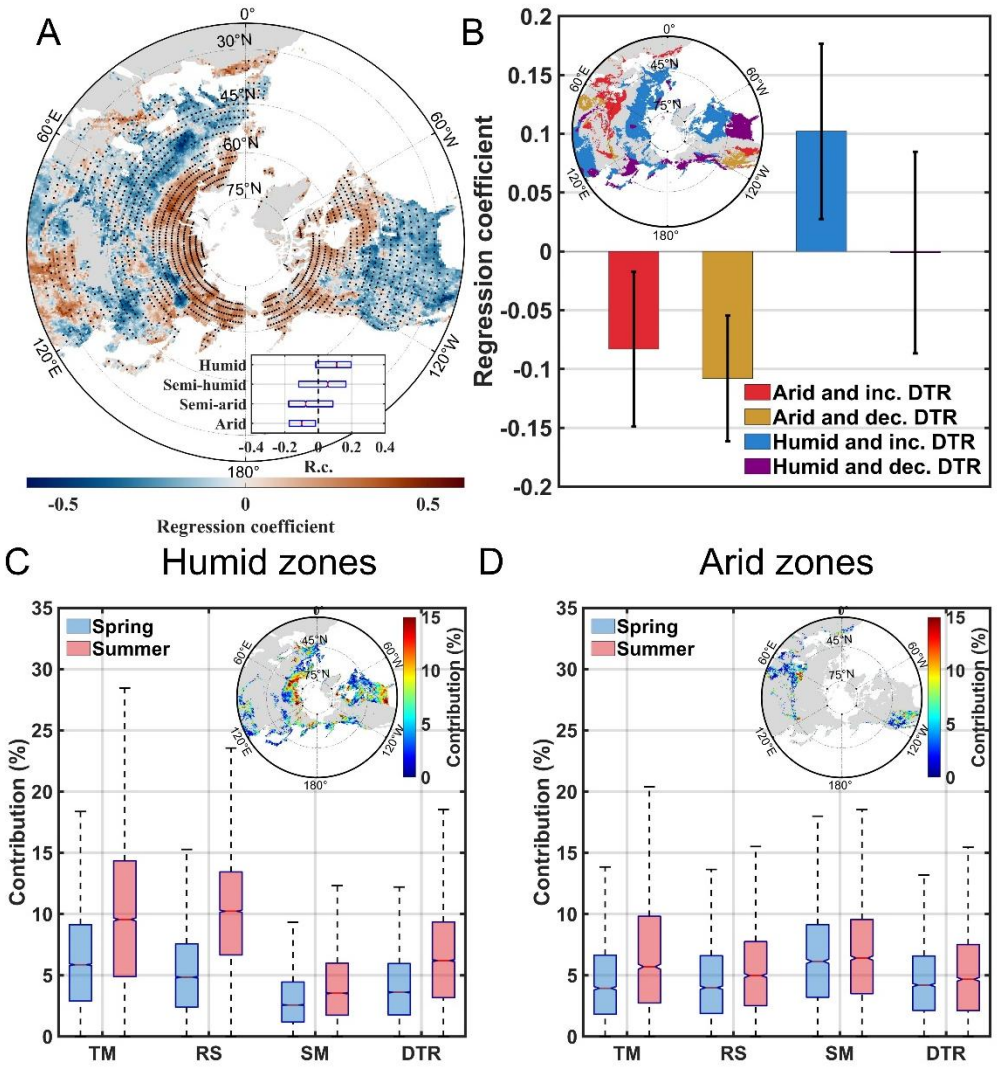

Figure 2. Impact of summer diurnal temperature range (DTR) on vegetation productivity. (A) Spatial distribution of ridge regression coefficients of summer DTR to annual net primary production (NPP) from 2002 to 2021. The black dots mark the areas where the regression results are significant at the $p<0.05$ level. The inset shows the regression coefficients across different climate zones with a boxplot. The width of each box indicates the interquartile range of the regression coefficients for all grid points, the red line within each box represents the median, and the left and right edges of the box indicate the first and third quartiles, respectively. (B) Ridge regression coefficients of NPP with summer DTR in four regions: arid zones with increasing (inc.) DTR, arid zones with decreasing (dec.) DTR, humid zones with inc. DTR, and humid zones with dec. DTR. The inset shows the spatial distribution of these four regions. (C and D) Assessment of the contributions of mean air temperature (TM), solar radiation (RS), soil moisture (SM), and DTR variations during spring and summer to the variations in annual NPP in humid (C) and arid (D) zones. The height of each box represents the interquartile range of contributions for all grid points, with the red line indicating the median, and the edges denoting the first and third quartiles. Whiskers depict the minimum and maximum contribution values, excluding outliers exceeding 1.5 times the interquartile range. The insets display the spatial distribution of the contribution of summer DTR to annual NPP.

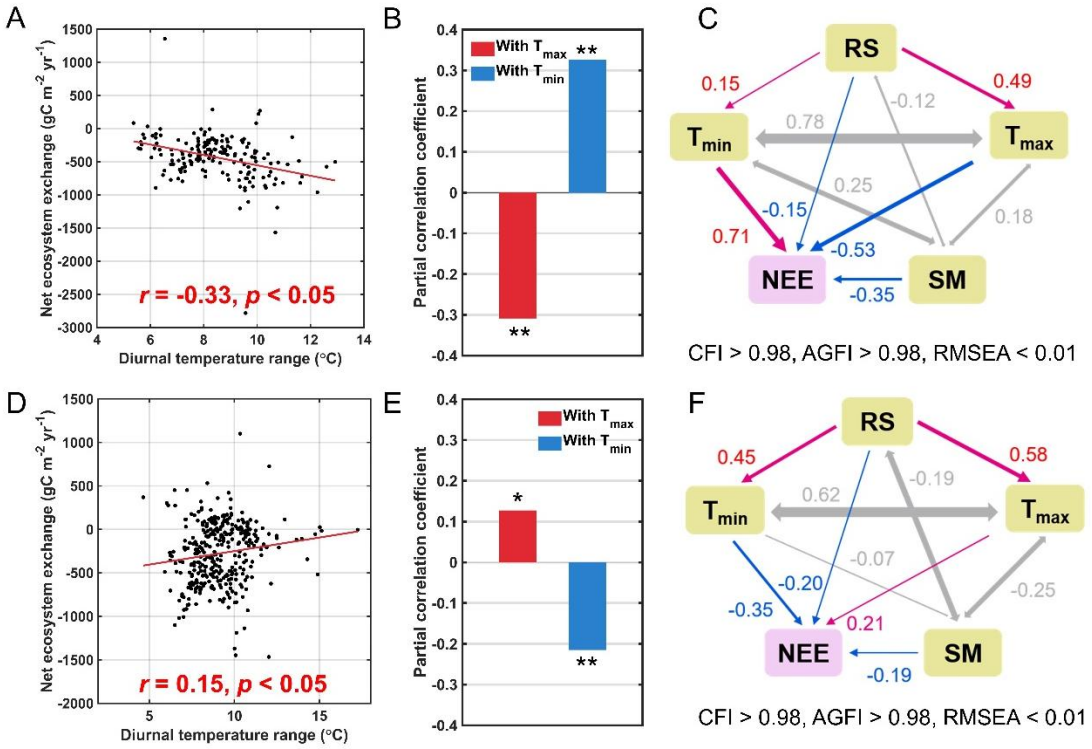

Figure 3. Impact of summer diurnal temperature range (DTR) on annual net ecosystem exchange (NEE) in forest ecosystems in humid zones during 2002–2021. (A and D) Relationship between summer DTR and annual NEE in deciduous broadleaf forests (DBF; A) and evergreen needleleaf forests (ENF; D). Each dot represents the annual NEE (y-axis) corresponding to the summer mean DTR (x-axis) across all sites and years within the ecosystem type. The Pearson correlation coefficient (*r*) is shown in the lower part of the figure. (B and E) Partial correlation coefficient of annual NEE with summer average daily maximum temperature (T_{max}) or daily minimum temperature (T_{min}), while controlling for the other temperature, in DBF (B) and ENF (E). The asterisk indicates the significance level (*: p<0.05, **: p<0.01). (C and F) The hypothesized effects of summer solar radiation (RS), soil moisture (SM), T_{max} and T_{min} on annual NEE, based on structural equation modeling, in DBF (C) and ENF (F). Double-headed gray arrows denote covariance between variables, while single-headed arrows indicate single-way causation, with positive and negative relationships in red and blue, respectively. Arrow thicknesses correspond to the strength of the relationships, with numbers next to the arrows representing the magnitude of the direct coefficients. The numbers below the graphs show the comparative fit index (CFI), adjusted goodness of fit index (AGFI) and root mean square error of approximation (RMSEA) of the structural equation models.

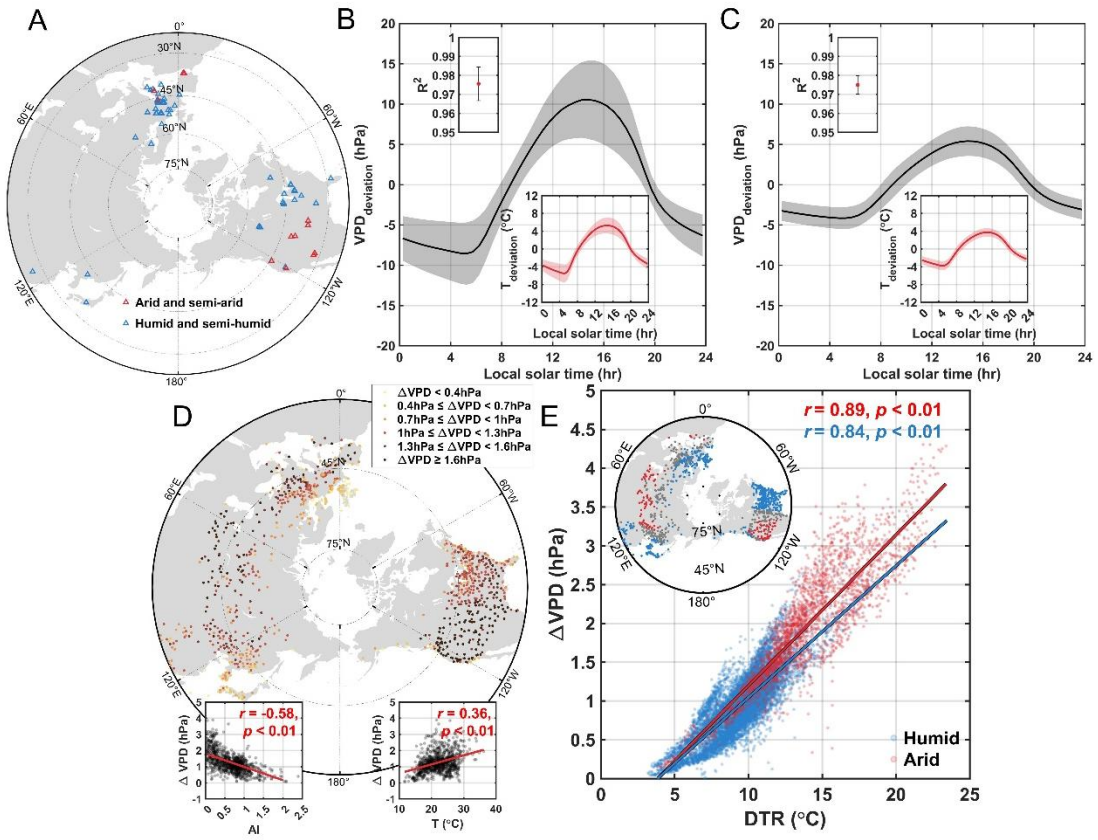

Figure 4. Vapor pressure deficit (VPD) variation and its relationship with changes in diurnal temperature range (DTR) during 2002–2021. (A) Locations of flux tower sites in arid/semi-arid and semi-humid/humid zones. (B and C) Averaged summer diurnal variations in VPD in arid/semi-arid zones (B) and semi-humid/humid zones (C). The y-axis represents the summer-average half-hourly VPD deviations ($VPD_{deviation}$) from the daily mean. The thick lines represent the mean value and the shading the standard deviation around the mean for different sites within each zone. The insets display the summer-average half-hourly temperature deviations ($T_{deviation}$) from the daily mean. The R-square value (R^2) of average diurnal variations in temperature on average diurnal variations in VPD is depicted in the upper left, with the mean value and 95% confidence interval displayed by red dots and error bars, respectively. (D) Spatial distribution of multi-year (2002–2021) summer average ΔVPD, defined as the difference between daily average VPD calculated using sub-daily temperature and relative humidity, and daily VPD calculated using daily average T and relative humidity. The variable ΔVPD is an indicator of the asymmetric effect of sub-diurnal temperature variations on daily average VPD. Observations of temperature and relative humidity were taken from the HadISD dataset. The inset illustrates the relationship between the aridity index (AI) and multi-year summer average ΔVPD, with the Pearson correlation coefficient (r) displayed. (E) Relationship between summer DTR and ΔVPD in arid and humid zones. Each dot represents the summer average ΔVPD (y-axis) corresponding to the summer average DTR (x-axis) across all sites and years (2002–2021) within the arid and humid zones. The inset displays the locations of the observations in arid (red point), humid (blue), and semi-arid/semi-humid (gray) zones.


EGU
Sharing not permitted

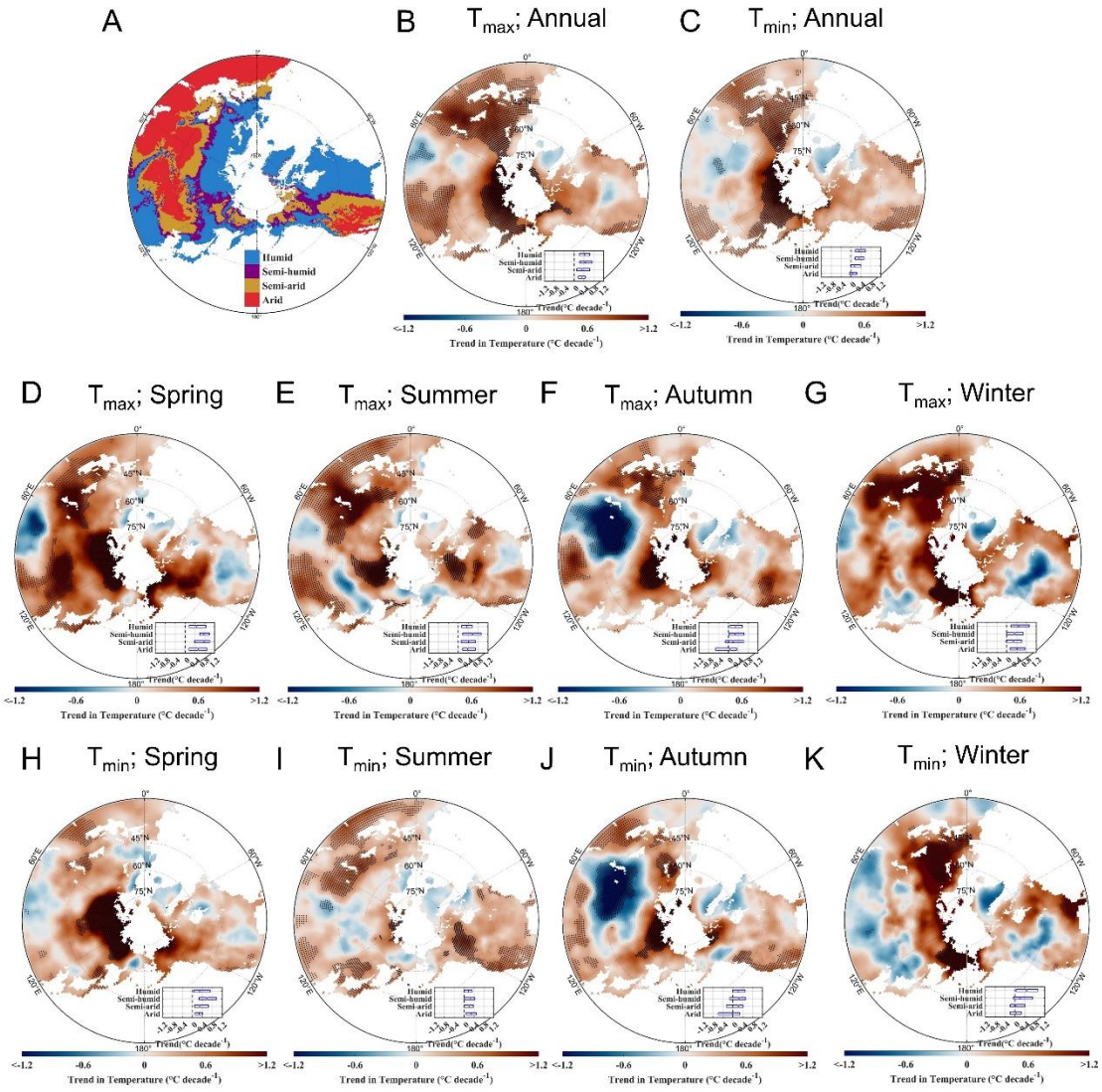

Figure S1. Trend in daily maximum temperature (T_{max}) and daily minimum temperature (T_{min}) in extratropical Northern Hemisphere during 2002-2021. (A) Spatial distribution of humid, semi-humid, semi-arid and arid zones. (B and C) Spatial distribution of the annual trend in T_{max} (B) and T_{min} (C). (D-G) Spatial distribution of the spring (D), summer (E), autumn (F) and winter (G) trend in T_{max}. (H-K) Spatial distribution of the spring (H), summer (I), autumn (J) and winter (K) trend in T_{min}. The black dots mark the areas where trends are significant at the p<0.1 level. The width of each box in the insets indicates the interquartile range of the trend in T_{max} or T_{min} for all grid points, the red line within each box represents the median, and the left and right edges of the box indicate the first and third quartiles, respectively.

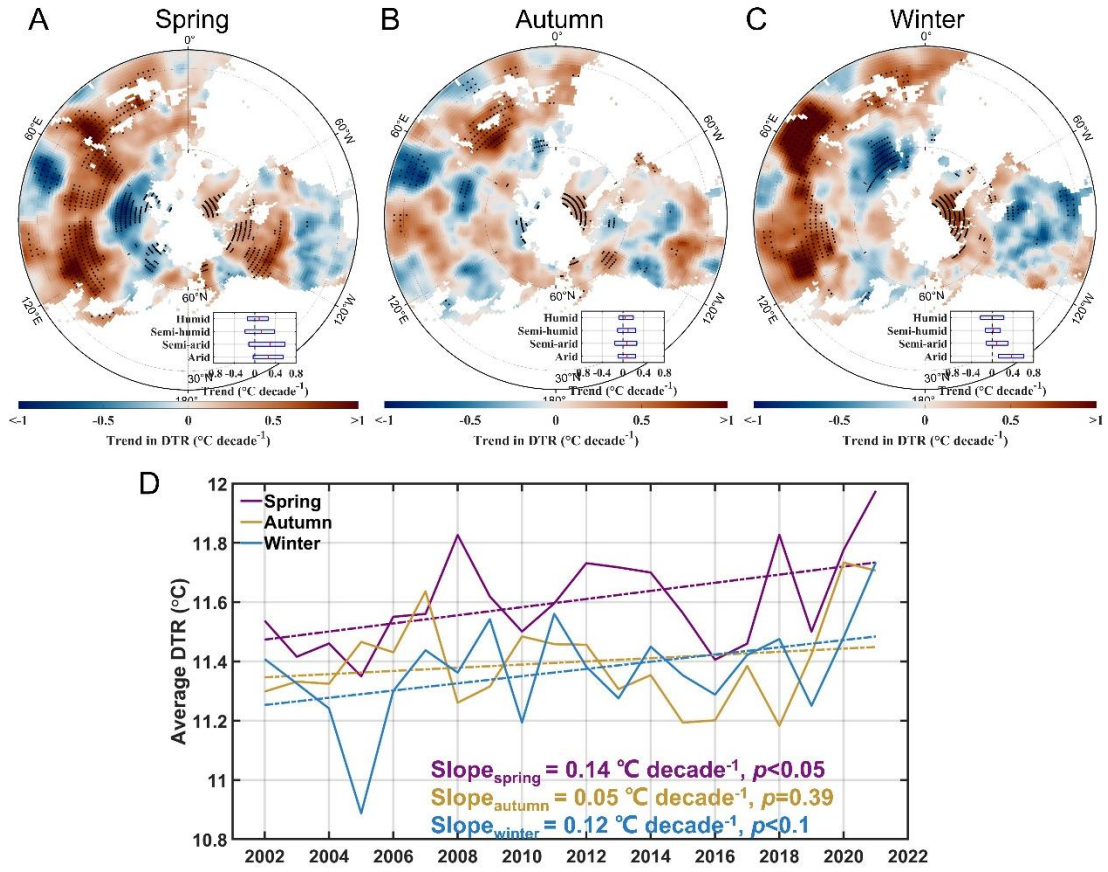

Figure S2. Trend in diurnal temperature range (DTR) in extratropical Northern Hemisphere in spring, autumn and winter during 2002-2021. (A-C) Spatial distribution of the DTR trend in spring (A), autumn (B) and winter (C). The black dots mark the areas where trends are significant at the $p<0.05$ level. The width of each box in the insets indicates the interquartile range of the trend in DTR for all grid points, the red line within each box represents the median, and the left and right edges of the box indicate the first and third quartiles, respectively. (D) Variations and changes in area-averaged spring, autumn and winter DTR in the extratropical Northern Hemisphere. The dashed lines show the linear trends obtained from linear regressions.

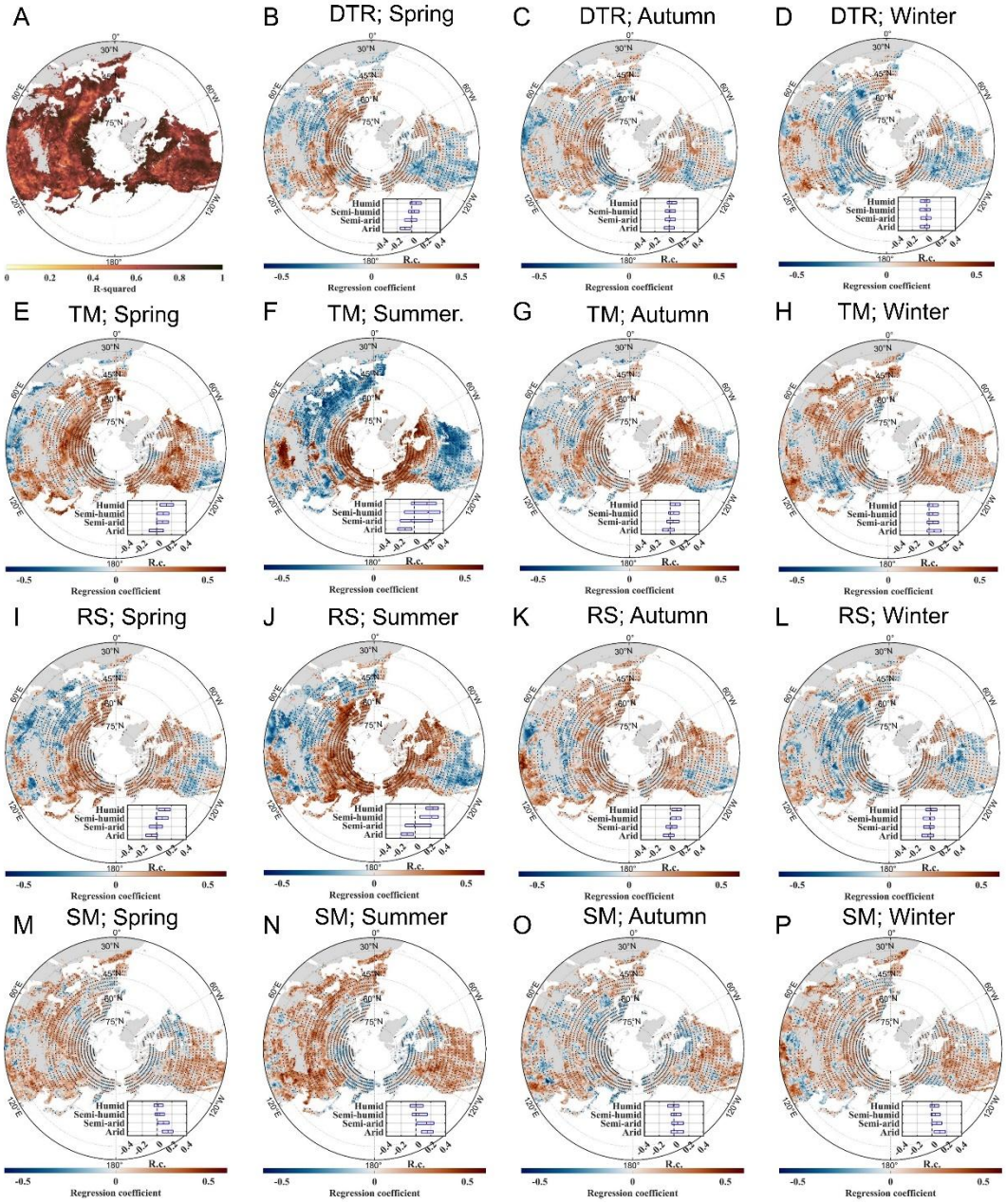

Figure S3. Impact of seasonal environmental variables on annual net primary productivity (NPP). (A) Spatial distribution of the coefficient of determination (R^2) of the regression model. (B-D) Spatial distribution of ridge regression coefficients (R.c.) of diurnal temperature range (DTR) during the spring (B), autumn (C) and winter (D) to annual NPP. (E-H) Spatial distribution of R.c. of mean air temperature (TM) during spring (E), summer (F), autumn (G) and winter (H) to annual NPP. (I-L) Spatial distribution of R.c. of mean solar radiation (RS) during spring (I), summer (J), autumn (K) and winter (L) to annual NPP. (M-P) Spatial distribution of R.c. of mean soil moisture (SM) during spring (M), summer (N), autumn (O) and winter (P) to annual NPP. The black dots mark the areas where the regression results are significant at the $p<0.05$ level. The width of each box indicates the interquartile range of the R.c. for all grid points, the red line within each box represents the median, and the left and right edges of the box indicate the first and third quartiles, respectively.

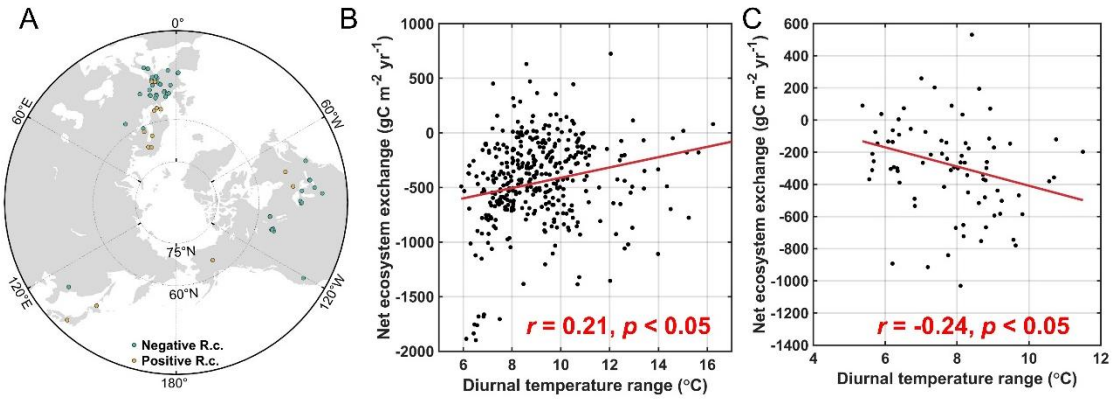

Figure S4. Correlation between summer diurnal temperature range (DTR) and annual net ecosystem exchange (NEE) across all forest flux tower sites. (A) Spatial distribution of sites with detected negative (green points) and positive (yellow points) ridge regression coefficients (R.c.) of net primary productivity (NPP) with DTR. (B and C) Correlation between summer DTR and annual NEE in regions with detected negative (B) and positive (C) R.c. of NPP with DTR across all forest flux tower sites.

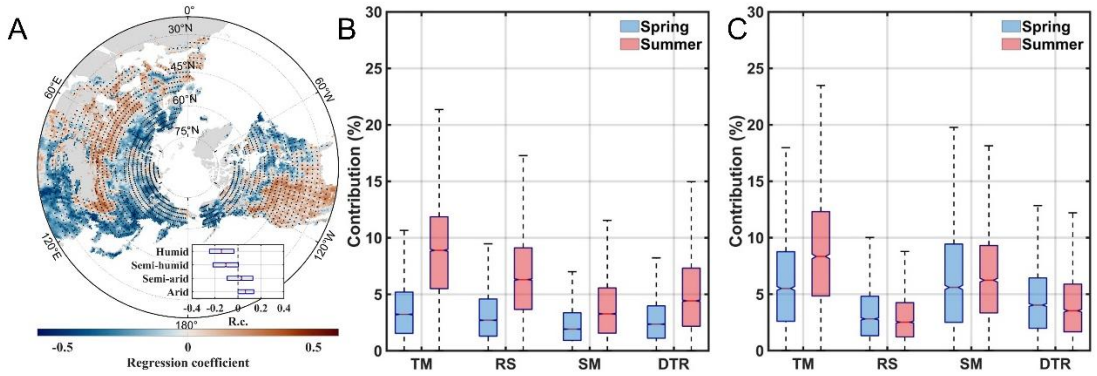

Figure S5. Impact of summer diurnal temperature range (DTR) on annual indicators of net ecosystem exchange (NEE) during 1981-2018. (A) Spatial distribution of regression coefficients for DTR during summer on annual NEE. The black dots mark the areas where the regression results are significant at the $p<0.05$ level. The width of each box in the inset indicates the interquartile range of the regression coefficients, the red line within each box represents the median, and the left and right edges of the box indicate the first and third quartiles, respectively. (B and C) Contribution of mean air temperature (TM), solar radiation (RS), soil moisture (SM) and DTR during spring and summer to variations in annual NEE in humid (B) and arid (C) zones, respectively. The height of each box indicates the interquartile range of contribution for all grid points, the red line in each box indicates the median, and the edges of the box indicate the first and third quartiles, respectively. Whiskers depict the minimum and maximum contribution values, excluding outliers exceeding 1.5 times the interquartile range.

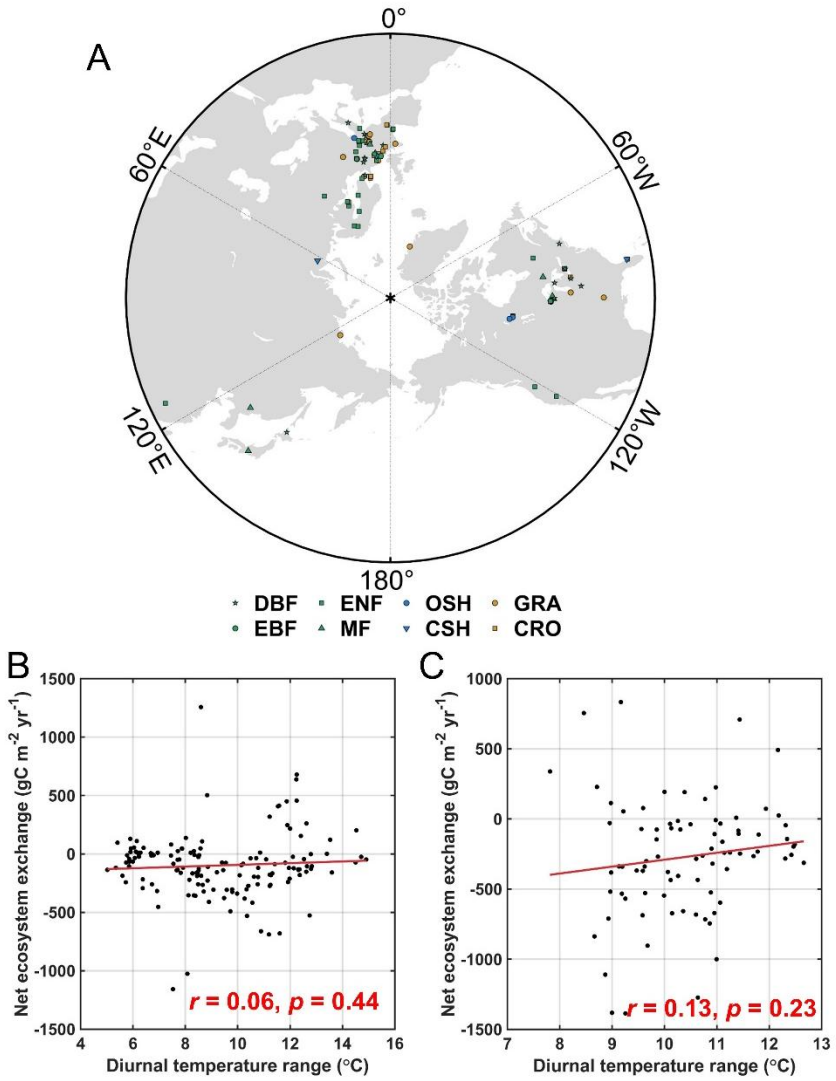

Figure S6. Relationship between summer diurnal temperature range (DTR) and annual net ecosystem exchange (NEE) in humid ecosystems. (A) Spatial distribution of flux tower sites in humid zones. The ecosystems include evergreen needleleaf forest (ENF), evergreen broadleaf forest (EBF), deciduous broadleaf forest (DBF), mixed forest (MF), closed shrub (CSH), open shrub (OSH), grassland (GRA) and cropland (CRO). (B and C) Relationship between summer DTR and annual NEE in humid grassland (B) and cropland (C) ecosystems. The Pearson correlation coefficients (*r*) are displayed in the lower part of the figures.

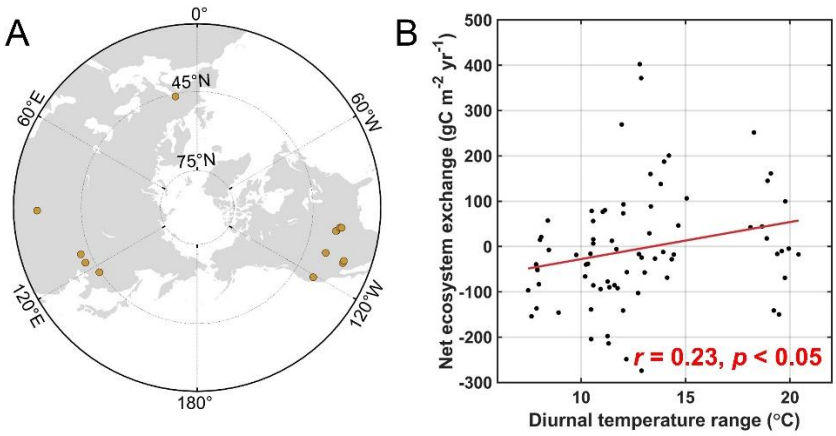

Figure S7. Relationship between diurnal temperature range (DTR) and net ecosystem exchange (NEE) in arid and semi-arid grassland ecosystems. (A) Spatial distribution of grassland flux tower sites in arid and semi-arid zones. (B) Relationship between summer DTR and annual NEE. The Pearson correlation coefficient (r) is displayed in the lower part of the figure.

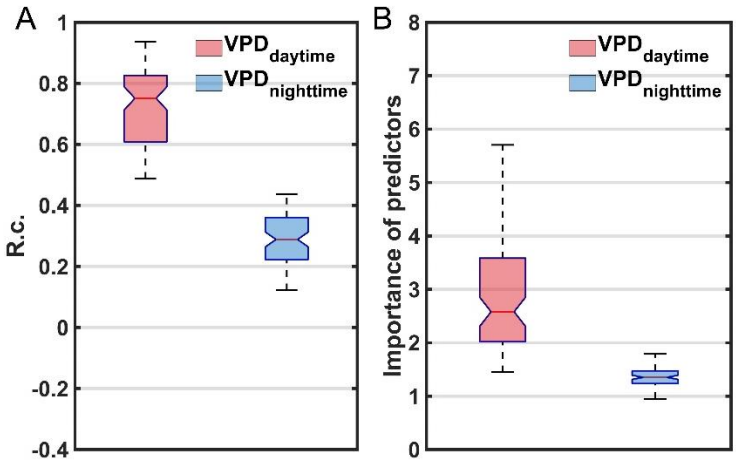

Figure S8. Impact of vapor pressure deficit (VPD) during the day ($VPD_{daytime}$) and night ($VPD_{nighttime}$) on the daily average VPD. (A) Ridge regression coefficients (R.c.) of daily $VPD_{daytime}$ and $VPD_{nighttime}$ to daily average VPD during summer. (B) Feature importance of predictors of daily $VPD_{daytime}$ and $VPD_{nighttime}$ to daily average VPD during summer. We employed out-of-bag predictor importance to assess the importance of predictors. The height of each box indicates the interquartile range of R.c. or feature importance of predictors, the red line in each box indicates the median, and the edges of the box indicate the first and third quartiles, respectively. Whiskers depict the minimum and maximum values, excluding outliers exceeding 1.5 times the interquartile range.

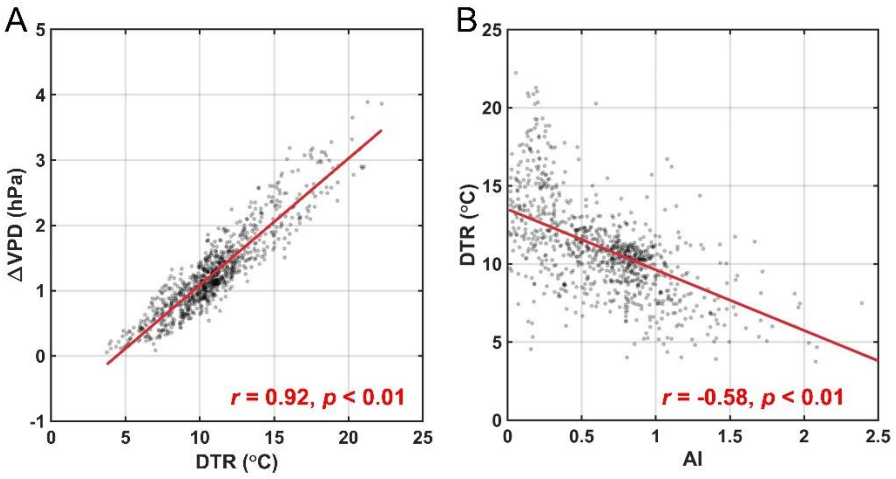

Figure S9. Relationship between summer diurnal temperature range (DTR), vapor pressure deficit (VPD) and aridity index (AI). (A) Relationship between multi-year (2002-2021) summer averaged DTR and ΔVPD, namely the difference between VPD generated by sub-daily and daily average temperature and relative humidity. (B) Relationship between the AI and multi-year summer averaged DTR. The Pearson correlation coefficients (*r*) are displayed in the lower part of the figures.

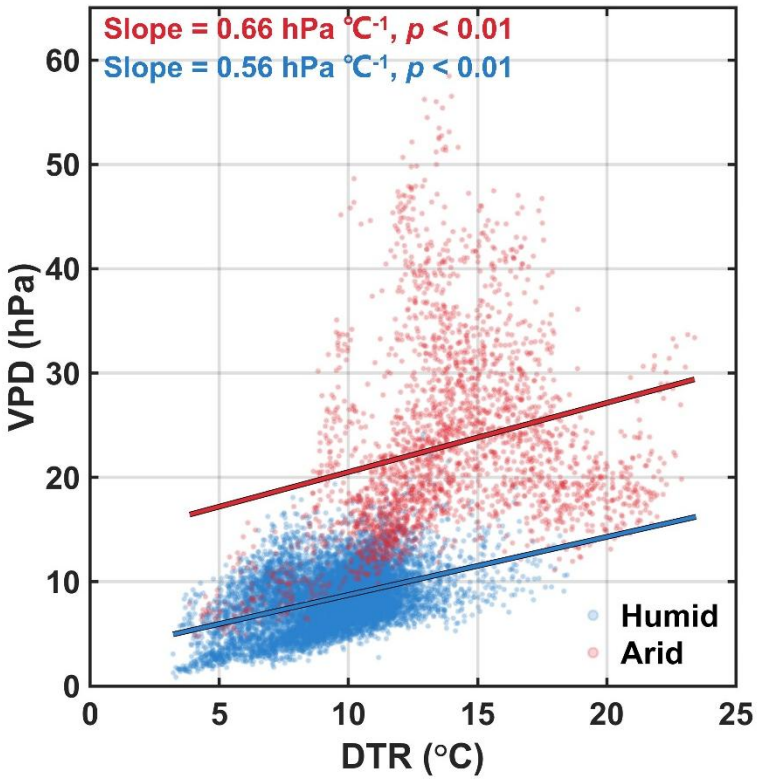

Figure S10. Vapor pressure deficit (VPD) variation with diurnal temperature range (DTR) variations in arid and humid zones. Each dot represents the summer average VPD (y-axis) corresponding to the summer average DTR (x-axis) across all sites and years (2002-2021) within the arid and humid zones. The VPD was calculated using sub-daily air temperature and relative humidity obtained from the HadISD dataset.

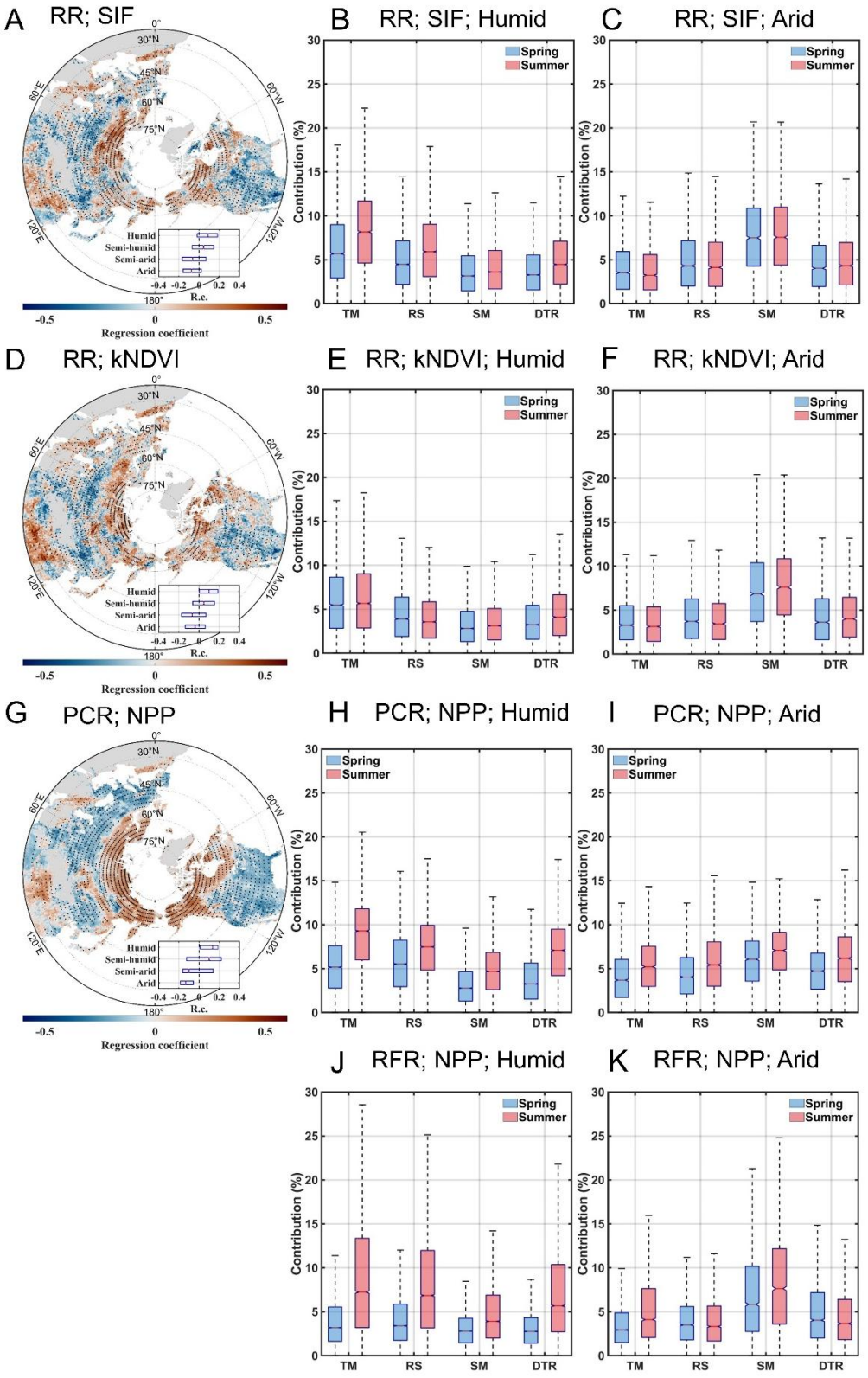

Figure S11. Impact of summer diurnal temperature range (DTR) on annual indicators of vegetation productivity during 2002-2021. (A, D and G) Spatial distribution of regression coefficients for DTR during summer on annual indicators: solar-induced fluorescence (SIF, A), kernel normalized difference vegetation index (kNDVI, D) and net primary productivity (NPP, G,). Ridge regression (RR) was applied to estimate the coefficients for A and D, while principal

components regression (PCR) was used for G. The black dots mark the areas where the regression results are significant at the $p<0.05$ level. The width of each box in the inset indicates the interquartile range of the regression coefficients, the red line within each box represents the median, and the left and right edges of the box indicate the first and third quartiles, respectively. (B-C, E-F and H-K) Contribution of mean air temperature (TM), solar radiation (RS), soil moisture (SM) and DTR during spring and summer to variations in annual SIF (B and C), kNDVI (E and F) and NPP (H-K) in humid (B, E, H and J) and arid (C, F, I and K) zones. RR was applied to estimate the coefficients for (B, C, E and F), PCR was applied to estimate the coefficients for (H and I), and random forest regression (RFR) were used for J and K, respectively. The height of each box indicates the interquartile range of contribution for all grid points, the red line in each box indicates the median, and the edges of the box indicate the first and third quartiles, respectively. Whiskers depict the minimum and maximum contribution values, excluding outliers exceeding 1.5 times the interquartile range.

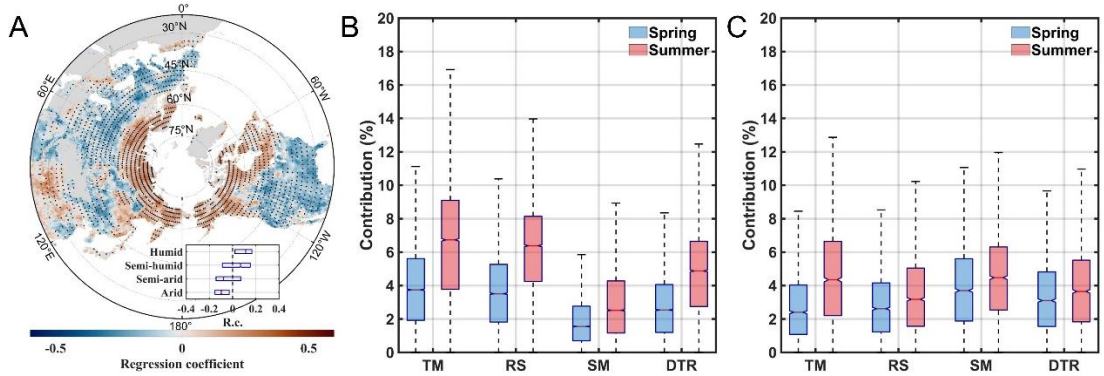

Figure S12. Impact of current year's summer diurnal temperature range (DTR) on annual indicators of net primary productivity (NPP) during 2003-2021. (A) Spatial distribution of regression coefficients for DTR during current year's summer on annual NEE. The black dots mark the areas where the regression results are significant at the $p<0.05$ level. The width of each box in the inset indicates the interquartile range of the regression coefficients, the red line within each box represents the median, and the left and right edges of the box indicate the first and third quartiles, respectively. (B and C) Contribution of current year's mean air temperature (TM), solar radiation (RS), soil moisture (SM) and DTR during spring and summer to variations in annual NEE in humid (B) and arid (C) zones, respectively. The height of each box indicates the interquartile range of contribution for all grid points, the red line in each box indicates the median, and the edges of the box indicate the first and third quartiles, respectively. Whiskers depict the minimum and maximum contribution values, excluding outliers exceeding 1.5 times the interquartile range. The regression analysis incorporated independent variables representing environmental factors from all seasons across two years (the current year and the previous year) with annual NPP of the current year as the response variable.

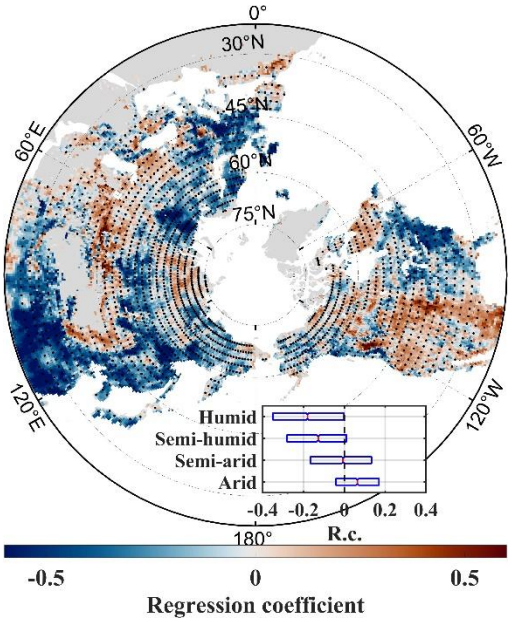

Figure S13. Spatial distribution of regression coefficients for growing season (May-October) diurnal temperature range (DTR) on growing season net ecosystem exchange (NEE). The black dots mark the areas where the regression results are significant at the $p<0.05$ level. The width of each box in the inset indicates the interquartile range of the regression coefficients, the red line within each box represents the median, and the left and right edges of the box indicate the first and third quartiles, respectively. The regression analysis incorporated independent variables representing DTR, mean temperature, solar radiation and soil moisture from the growing season, with growing season NEE as the response variable.

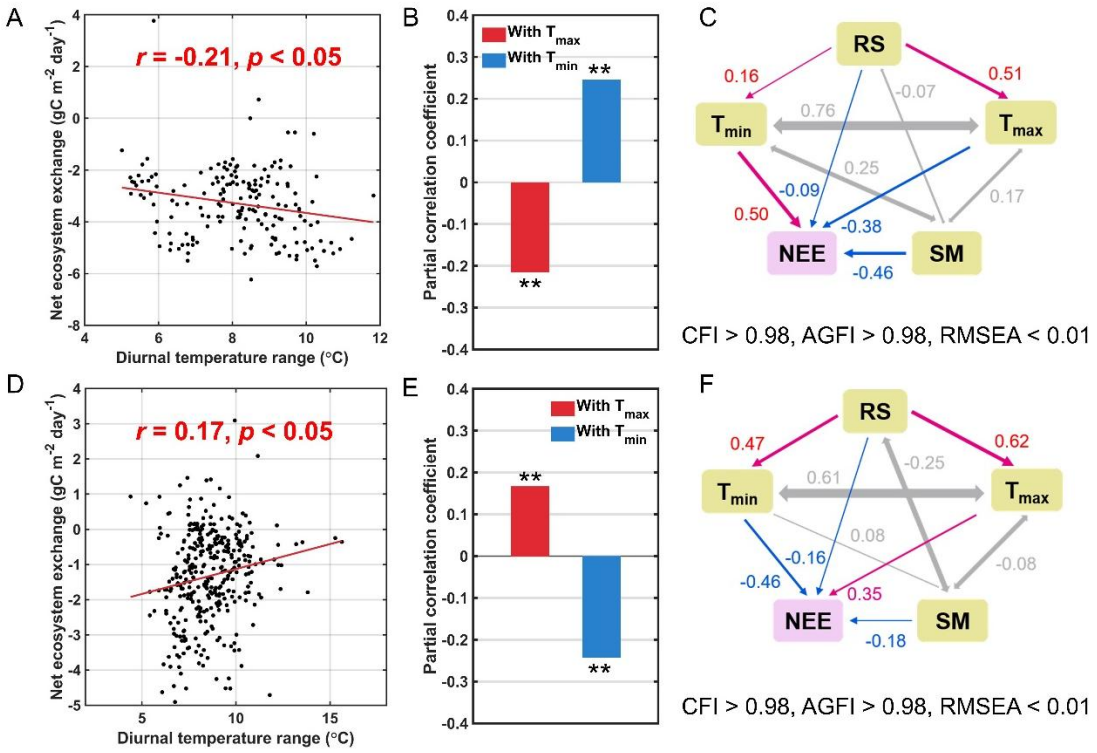

Figure S14. Impact of growing season (May-October) diurnal temperature range (DTR) on net ecosystem exchange (NEE) in forest ecosystems in humid zones. (A and D) Relationship between growing season average DTR and NEE in deciduous broadleaf forests (DBF; A) and evergreen needleleaf forests (ENF; D). Each dot represents the annual NEE (y-axis) corresponding to the summer mean DTR (x-axis) across all sites and years within the ecosystem type. The Pearson correlation coefficient (r) is shown in the lower part of the figure. (B and E) Partial correlation coefficient of growing season average NEE with daily maximum temperature (T_{max}) or daily minimum temperature (T_{min}), while controlling for the other temperature, in DBF (B) and ENF (E). The asterisk indicates the significance level (*: p<0.05, **: p<0.01). (C and F) The hypothesized effects of growing season average solar radiation (RS), soil moisture (SM), T_{max} and T_{min} on NEE based on structural equation modeling, in DBF (C) and ENF (F). Double-headed gray arrows denote covariance between variables, while single-headed arrows indicate single-way causation, with positive and negative relationships in red and blue, respectively. Arrow thicknesses correspond to the strength of the relationships, with numbers next to the arrows representing the magnitude of the direct coefficients. The numbers below the graphs show the comparative fit index (CFI), adjusted goodness of fit index (AGFI) and root mean square error of approximation (RMSEA) of the structural equation models.

ECOLOGY

Disentangling the effects of vapor pressure deficit on northern terrestrial vegetation productivity

Ziqian Zhong[1], Bin He[1]*, Ying-Ping Wang[2], Hans W. Chen[3], Deliang Chen[4], Yongshuo H. Fu[5], Yaning Chen[6], Lanlan Guo[7], Ying Deng[8], Ling Huang[9], Wenping Yuan[10], Xingmin Hao[6], Rui Tang[1], Huiming Liu[11], Liying Sun[12], Xiaoming Xie[1], Yafeng Zhang[1]

The impact of atmospheric vapor pressure deficit (VPD) on plant photosynthesis has long been acknowledged, but large interactions with air temperature (T) and soil moisture (SM) still hinder a complete understanding of the influence of VPD on vegetation production across various climate zones. Here, we found a diverging response of productivity to VPD in the Northern Hemisphere by excluding interactive effects of VPD with T and SM. The interactions between VPD and T/SM not only offset the potential positive impact of warming on vegetation productivity but also amplifies the negative effect of soil drying. Notably, for high-latitude ecosystems, there occurs a pronounced shift in vegetation productivity's response to VPD during the growing season when VPD surpasses a threshold of 3.5 to 4.0 hectopascals. These results yield previously unknown insights into the role of VPD in terrestrial ecosystems and enhance our comprehension of the terrestrial carbon cycle's response to global warming.

INTRODUCTION

Atmospheric vapor pressure deficit (VPD), defined as the difference between the saturated vapor pressure and actual vapor pressure, is an important factor influencing stomatal conductance and therefore photosynthesis (*1*, *2*). Plants close their stomata to prevent excessive water loss when VPD is high, and thus, the photosynthesis and carbon uptake of plants are reduced (*1*–*4*). Several studies showed that an increase in VPD substantially influenced vegetation productivity (*1*–*4*), forest mortality (*3*, *5*), crop yields (*6*, *7*), and global terrestrial carbon sinks (*8*). Considering the likely increase in VPD under global warming, VPD will play an increasing role in controlling global ecosystem, carbon, and water exchanges (*2*, *9*).

Changes in VPD can be caused by moisture content in the air and air temperature (T). Evapotranspiration is controlled by soil moisture (SM) among other factors, providing an important source of atmospheric moisture. Therefore, the impact of VPD on vegetation productivity can be driven directly and indirectly through SM and air T. Despite the wide attention given to the effects of VPD on ecosystems, a question that remains open is to what extent vegetation productivity at the regional scale and in different climate zones is influenced by VPD. The difficulty in answering this question lies in the fact that VPD is closely coupled to T and SM, which also have strong influences on terrestrial vegetation productivity. According to the Clausius-Clapeyron relation, the saturated vapor pressure is determined entirely by T (*10*, *11*); therefore, the high correlation between VPD and T is expected. In contrast to the generally negative impact of VPD on vegetation productivity, the impact of T on vegetation productivity is more complex (*12*, *13*). SM is another factor strongly coupled with VPD due to land-atmosphere interactions (*14*, *15*), and can constrain plant photosynthesis directly because it determines the amount of water that can be extracted by plant roots (*16*). Simultaneously, increased VPD associated with decreased SM also affects photosynthesis by regulating the plant stomatal opening (*17*–*19*). To date, the relative effects of VPD, T, and SM on vegetation production remain debated and are difficult to disentangle, while identification of these effects is important to gain a better understanding of the response of vegetation productivity to climate change and improving terrestrial ecosystem models.

In this study, we analyzed the independent effects of VPD on vegetation productivity over the Northern Hemisphere (NH) after excluding the effects caused by T and SM. Satellite observation-based contiguous solar-induced fluorescence (CSIF) and leaf area index (LAI), as well as gross primary productivity simulated from empirical models based on eddy covariance observational data (GPP-FLUXCOM), were used as proxies for vegetation productivity. To quantify the independent influences of VPD, we first used ridge regression analysis to eliminate the interactions between VPD and T or SM and assessed the response of vegetation productivity to VPD at the interannual scale using growing-season mean values. Here, T and VPD were sourced from the fifth generation ECMWF reanalysis (ERA5) dataset (*20*), and SM was obtained from the Global Land Evaporation Amsterdam Model (GLEAM) dataset (*21*). The vegetation growing season was defined as those months with an average T higher than 0°C (*22*). We then applied

[1]State Key Laboratory of Earth Surface Processes and Resource Ecology, Faculty of Geographical Science, Beijing Normal University, 100875 Beijing, China. [2]CSIRO Environment, Private Bag 1, Aspendale, Victoria, Australia. [3]Department of Space, Earth and Environment, Division of Geoscience and Remote Sensing, Chalmers University of Technology, SE-412 96 Gothenburg, Sweden. [4]Regional Climate Group, Department of Earth Sciences, University of Gothenburg, S-40530 Gothenburg, Sweden. [5]College of Water Sciences, Beijing Normal University, 100875 Beijing, China. [6]State Key Laboratory of Desert and Oasis Ecology, Xinjiang Institute of Ecology and Geography, Chinese Academy of Sciences, 830011 Urumqi, China. [7]School of Geography, Beijing Normal University, 100875 Beijing, China. [8]State Key Laboratory of Vegetation and Environmental Change, Institute of Botany, Chinese Academy of Sciences, No. 20 Nanxincun, Xiangshan, 100093 Beijing, China. [9]College of Urban and Environmental Sciences, Peking University, 100871 Beijing, China. [10]School of Atmospheric Sciences, Sun Yat-Sen University, 510275 Guangzhou, China. [11]Ministry of Ecology and Environment Center for Satellite Application on Ecology and Environment, 100094 Beijing, China. [12]Key Laboratory of Water Cycle and Related Land Surface Processes, Institute of Geographic Sciences and Natural Resources Research, Chinese Academy of Sciences, 100101 Beijing, China.
*Corresponding author. Email: hebin@bnu.edu.cn

a structural equation model with the partial least square (PLS-SEM) algorithm to disentangle the direct effect of VPD on vegetation from the indirect effects of T or SM on vegetation via VPD.

RESULTS

The independent effects of VPD on vegetation productivity

The independent effect refers to the impact of an independent variable on the dependent variable after excluding confounding effects of other independent variables (*23*, *24*). In this study, the independent effect of VPD on GPP represents the magnitude of GPP change resulting from variations in VPD while controlling for the effects of other environmental factors that may also influence GPP, such as T and SM. High degrees of multicollinearity among VPD, SM, and T have posed challenges to quantifying the independent effect of VPD on GPP. High multicollinearity is evident in the notable correlations between the average growing-season VPD and SM or T (fig. S1A and B). In addition, high variance inflation factors (VIFs; see Materials and Methods) are found in most areas across the NH for a multiple linear regression with an average growing-season SM, T, VPD, and solar radiation (R) as independent variables and an average growing-season CSIF as the dependent variable (fig. S1C), reinforcing this issue. In this analysis, the effect of solar radiation on vegetation productivity was considered as there is a direct correlation between solar radiation and plant photosynthesis. These high degrees of multicollinearity among independent variables have the potential to result in substantial regression coefficient bias and misleading statistical inferences (*23*, *25*).

To reduce the impact of multicollinearity on the correct detection of the relationships, we performed a ridge regression analysis (*26*) to assess the effect of the average growing-season VPD on CSIF. Ridge regression is a linear regularization method and an effective eliminator of multicollinearity. It improves upon the ordinary least square regression model in scenarios where the independent variables are strongly correlated by introducing a penalty term in the cost function, which penalizes large parameter values. Thus, it is appropriate for analysis when there exists severe multicollinearity among independent variables. As shown in fig. S1D, the VIFs of the ridge regression model are much smaller than that of the original multivariate linear model, indicating that the interactions among SM, T, and VPD were minimized and that the regression coefficients of the ridge regression model offered more reliable information about the influences of the independent variables than that of the multiple linear regression model.

On the basis of the ridge regression analysis using average annual growing-season values, a distinct contrast in the independent effect of VPD on CSIF is observed between arid and humid zones (Fig. 1). In most middle- and low-latitude regions, such as Central Asia, western North America, and India, the CSIF was negatively correlated with VPD, which is consistent with the negative responses of surface conductance or photosynthesis to increases in VPD (*2*, *27*). In contrast, CSIF was positively correlated with VPD in some boreal zones, such as northern Eurasia and northern North America. Similar results were also found over the NH when using GPP-FLUXCOM (1980–2018) and LAI–Moderate Resolution Imaging Spectroradiometer (MODIS) (2001–2019) as proxies for vegetation productivity instead of CSIF (fig. S2) or when substituting SM data obtained from the ERA5 dataset instead of the GLEAM dataset (fig. S3). To test the robustness of our analysis, we also applied an additional statistical analysis called principal component regression (*28*). Principal component regression produces principal components (PCs) that are orthogonal (i.e., uncorrelated) to each other in the regression, enabling optimal performance with highly correlated predictor variables. This method reveals a consistent pattern in the response of vegetation productivity proxies (CSIF, GPP-FLUXCOM, and LAI-MODIS) to VPD, with a notable variation found in the independent impact of VPD on productivity among different climate zones (fig. S4). Both regression methods demonstrate that vegetation productivity shows a negative response to VPD changes in arid and semiarid zones while exhibiting neutral or positive responses in humid zones.

The role of VPD in vegetation production

The above analysis suggests that VPD changes alone extensively affected vegetation productivity during 2000–2019. In the real world, however, VPD is considered the middle variable of T or SM variations affecting vegetation productivity. For example, rising T could lead to higher VPD and thereby further limit plant photosynthesis. In addition, when soil becomes wetter, the increasing evaporation reduces VPD and further promotes plant transpiration and photosynthesis. These different processes imply simultaneously multiple pathways for VPD to influence vegetation productivity by interacting with other variables, such as T and SM. To further reveal how T and SM have influenced vegetation production via VPD, a PLS-SEM model (see Materials and Methods) was used to detect the direct and indirect effects of average growing-season climatic variables and SM on vegetation productivity. Figure 2A shows all pathways of how the environmental variables (SM, T, VPD, and solar radiation) can affect CSIF in the PLS-SEM model. Here, we used goodness of fit (GoF), an index for assessing the overall prediction performance of the model, to measure the model reliability (Fig. 2B). Only grid cells with a GoF larger than 0.5 from the PLS-SEM results were considered in the analyses following a previous study (*29*). The effect of environmental factors on vegetation productivity was quantified using the derived influence coefficients from the PLS-SEM model, where a high positive influence coefficient indicates a strong positive effect. The strengths of the direct effects were given by the path coefficients, which represent the direction and strength of the linear relationships between variables. An indirect effect is the influence of one predictor on another response variable by taking an indirect path, namely, adding the product of all possible paths excluding the direct effect (*29*). The total effect is defined as the sum of direct effects and indirect effects.

To detect what role VPD has played in affecting vegetation productivity, we compared and quantified the direct effect of T on CSIF with the indirect effect of T on CSIF via VPD during 2000–2019. The interactions between the direct effect of average growing-season T (Di.) and indirect effect of average growing-season T via VPD (In.) on CSIF were divided into four categories: positive Di. and In. (Di+ and In+), positive Di. and negative In. (Di+ and In−), negative Di. and positive In. (Di− and In+), and negative Di. and In. (Di− and In−). When the directions of direct and indirect effects are the same, we call this an enhancing effect and otherwise an offset effect. The degree of enhancing or offset effects could be determined by the absolute value of the ratio (%) of the In. to the Di. influence coefficient in the PLS-SEM model. Here, T exerted a negative, indirect effect on CSIF via VPD across most middle- and low-latitude regions, especially in arid and semiarid

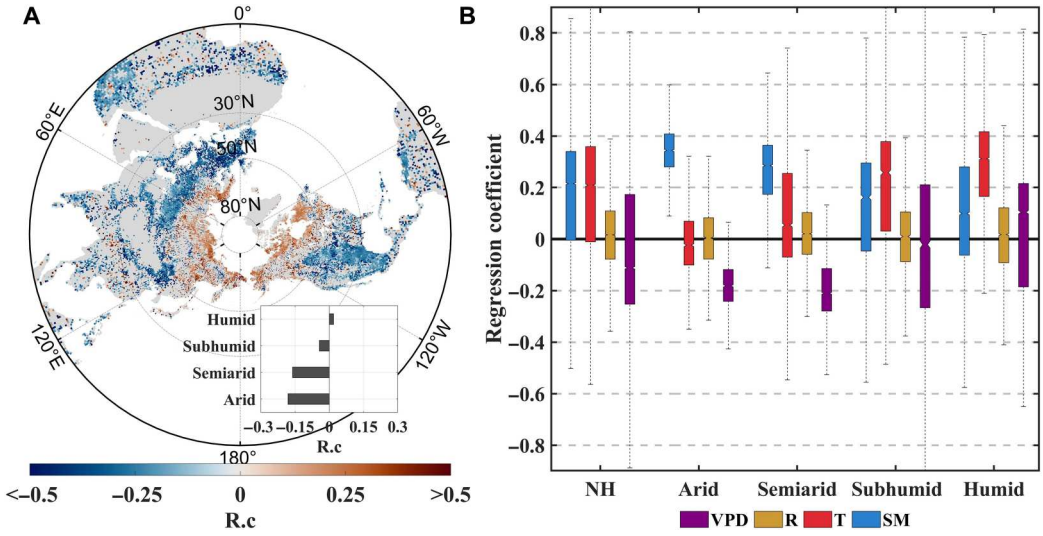

Fig. 1. The independent effect of VPD on vegetation productivity over the NH. (**A**) Ridge regression coefficient (R.c) of VPD to CSIF during the growing season from 2000 to 2019. The inset shows the mean value of the R.c over arid, semiarid, subhumid, and humid zones. (**B**) R.cs for VPD, solar radiation (R), air T, and SM in the regression with CSIF over the different climate zones, visualized with a boxplot. The height of each box indicates the interquartile range, the notch of each box indicates the median, and the bottom and top of the box indicate the first and third quartiles, respectively. The whiskers that extend to the most extreme regression coefficient are not considered outliers, which is a value that is more than 1.5 times the interquartile range away from the bottom or top of the box. Only the grid cells with the regression result that passed the test of significance ($P < 0.05$) were analyzed and are shown.

zones, while a positive indirect effect on CSIF via VPD was observed in the high-latitude region (Fig. 2D). One major interaction was that the negative effect of T on CSIF via VPD offset the positive effect of T on CSIF (Di+ and In−), which accounted for 55.6% of the vegetation area and was mainly distributed in eastern Africa, Europe, Central Asia, India, East Asia, and North America (Fig. 2E). In these areas, vegetation productivity increased with increasing T, while vegetation productivity may also have been supressed by the higher VPD caused by a rising T. We focused on this most widespread interaction and found that the negative effect of T on CSIF via VPD offset had a median magnitude of 69.4% of the positive effect of T on CSIF over the NH (Fig. 2F). This offset effect was strongest in the arid zone (126.7%), followed by that in the semiarid (112.2%), subhumid (62.5%), and humid (39.0%) zones. Here, median values were used to minimize the impact of outliers. Similar results were also found when using LAI-MODIS data that covers a comparable time period (2001–2019) as a proxy for GPP (fig. S5) or when substituting SM data obtained from the ERA5 dataset instead of the GLEAM dataset (fig. S6).

In parallel to the direct and indirect effects of T on CSIF, the direct effect of SM on CSIF and the indirect effect of SM on CSIF via VPD during 2000–2019 were also recognized, as shown in Fig. 3. SM exerted a positive indirect effect on CSIF via VPD across most regions. In contrast to the counteraction between the direct and indirect effects of T on CSIF, the direct positive effect of SM and indirect positive effect of SM via VPD on CSIF (Di+ and In+) reinforced each other in arid and semiarid zones, which respectively accounted for 63.6 and 60.8% of the total vegetated area in these zones, respectively. The process by which SM positively affected CSIF via VPD can be explained by the fact that increased SM could have reduced VPD through increased evaporation and further restrained the negative effects on vegetation brought by high-VPD conditions. The interactions between Di. and In. in humid and semihumid zones were complex (Fig. 3C). Vegetation in these zones was not limited by water availability; therefore, the positive Di. or In. was not prevalent in these areas. Similar results were also found when using LAI-MODIS data as a proxy for GPP during the period 2001 to 2019, as well as when substituting SM data obtained from the ERA5 dataset instead of the GLEAM dataset, as demonstrated by figs. S7 and S8, respectively. The above findings reveal the strong counteraction between the direct effect of T and T-associated VPD effect on CSIF and the enhancement of the direct effect of SM and SM-associated VPD effect on CSIF.

The threshold of VPD sensitivities of vegetation productivity

The results above show diverging sensitivities of productivity to VPD across different climate zones. The shift from a positive to a negative influence of VPD on productivity indicates that there is a VPD threshold that determines the direction of the effect of VPD on vegetation productivity. We hypothesize that VPD positively influenced photosynthesis during the growing season up to a certain VPD threshold, beyond which a shift in the response direction of vegetation productivity to VPD occurred with the increase of VPD. To test this hypothesis, we focused on the interannual effect of VPD on the GPP in high-latitude Eurasia (0° to 180°E, 50° to 85°N), where we detected the positive effect of VPD on vegetation productivity based on the ridge regression analysis (Fig. 1A) and PLS-SEM analysis (Fig. 2D). As depicted in the insets of Fig. 4, we investigated the ridge regression coefficient (R.c) between VPD and interannual variations of GPP-FLUXCOM or CSIF during the growing season. The median of R.c changed modestly at first and declined significantly above a certain VPD threshold. The average growing-season VPD threshold, which was defined as breakpoints (BPs) of the medians in Fig. 4, was identified by the

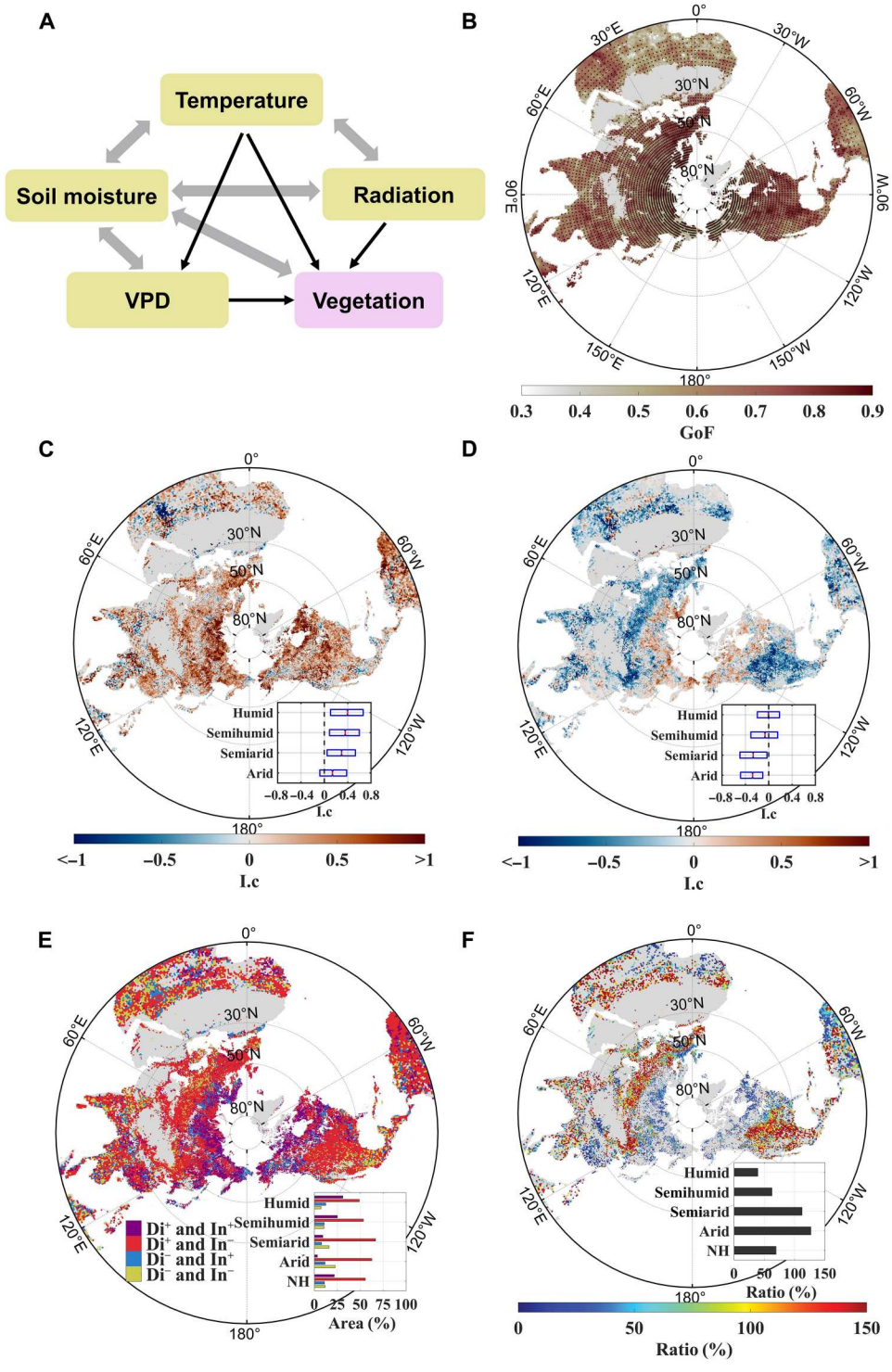

Fig. 2. The offset effect of the influence of VPD on vegetation productivity compared to the air T effect on vegetation productivity. (**A**) Conceptual model depicting hypothesized direct and indirect effects of T, SM, R, and VPD on vegetation productivity, which was represented by CSIF. Double-headed gray arrows indicate covariance between the variables, and single-headed black arrows indicate the hypothesized direction of causation. (**B**) GoF of PLS-SEM with CSIF as the vegetation productivity proxies during the growing season from 2000 to 2019. The dots indicate the pixels with a GoF of PLS-SEM larger than 0.5. (**C**) Direct effect of T on CSIF (Di.) and (**D**) the indirect effect of T on CSIF via VPD (In.) during the growing season from 2000 to 2019. The effects were quantified using the derived influence coefficients (I.cs) from the PLS-SEM model, which were visualized with a boxplot. The width of each box indicates the interquartile range of I.c for all grid points, the red line in each box indicates the median, and the left and right edges of the box indicate the first and third quartiles, respectively. (**E**) Interaction between positive or negative Di. (Di+ or Di−) and positive or negative In. (In+ or In−) on CSIF. The insets show the area proportion (%) of different categories of interaction over the whole NH and different climate zones. (**F**) Degree of offset effect (ratio) between Di+ and In−. Only the regions in (E) with Di+ and In− were selected and analyzed. The insets show the median of the ratio in the grid points over different climate zones.

nonparametric Pettitt breakpoint test (*30*) as 3.50 hPa ($P < 0.01$) and 3.96 hPa ($P < 0.01$) derived from the GPP-FLUXCOM and CSIF data, respectively. Above the VPD threshold, the positive sensitivity of vegetation productivity declined substantially. Similar results were also found when ridge regression analysis was performed using the SM data obtained from the ERA5 dataset instead of the GLEAM dataset (fig. S9) or when the independent effect of VPD on vegetation productivity proxy was estimated by principal component regression (fig. S10).

DISCUSSION

In this study, we found that there were differences in the sensitivity of productivity to VPD across different climate zones, although it is

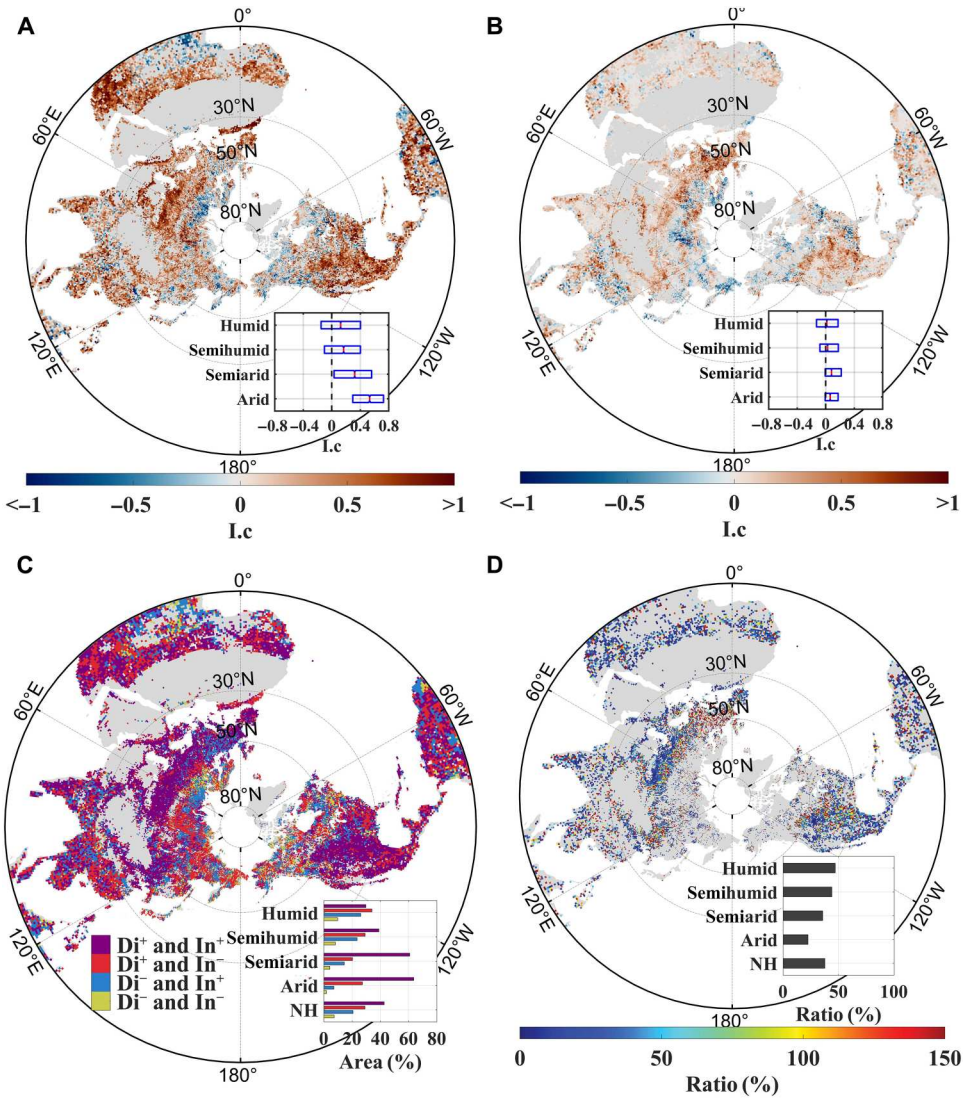

Fig. 3. The enhancing effect of the influence of VPD on vegetation productivity to the influence of SM on vegetation productivity. (**A**) Direct effect of SM on CSIF (Di.) and (**B**) the indirect effect of SM on CSIF via VPD (In.) during the growing season from 2000 to 2019. The effects were quantified using the derived I.cs from the PLS-SEM model, which were visualized with a boxplot. The width of each box indicates the interquartile range of I.c for grid points, the red line in each box indicates the median, and the left and right edges of the box indicate the first and third quartiles, respectively. (**C**) Interaction between positive or negative Di. (Di+ or Di−) and positive or negative In. (In+ or In−) on CSIF. The inset shows the area proportion (%) of different categories of interaction over the whole NH and different climate zones. (**D**) Degree of enhancing effect (ratio) between Di+ and In+. Only the regions in (C) with Di+ and In+ were selected and analyzed. The inset shows the median of the ratio in the grid points over different climate zones.

well known that increasing VPD alone reduces stomatal conductance and further inhibits photosynthesis under conditions of high VPD. By contrast, however, some leaf-scale studies have suggested that the stomatal conductance of leaves increases with increasing VPD (*31*, *32*) and thus leads to an increased photosynthetic rate under conditions of low VPD (*33*, *34*). When VPD is low and the stomata are fully open, the leaf guard cells sense the increased rate of transpiration through the stomatal pores and induce stomatal opening (*35*). As a result of this "feedback" response (*36*), with an increase of VPD, the transpiration rate increases and the nutrient (such as nitrogen, phosphorus, and potassium) uptake from the soil is promoted (*37*–*40*), which is beneficial for vegetation growth. Moreover, some field experiments performed in northern Europe where the positive effect of VPD on vegetation productivity was detected (Fig. 1A) revealed adverse effects of an increase in atmospheric humidity (or decrease in VPD) on photosynthetic capacity and growth rate in vegetation. The adverse impact includes reducing branch and stem wood density and diminishing nutrient supply to foliage (*34*), reducing glandular trichome density (*39*), and reducing intrinsic water-use efficiency, which could expose plants to a greater risk of dehydration under water stress (*41*). These factors could explain the neutral or even positive effects of VPD on vegetation in regions with generally low VPD, such as northern Eurasia.

The varying responses of vegetation productivity to VPD in dry and moist regions result in a rapid shift toward negative responses

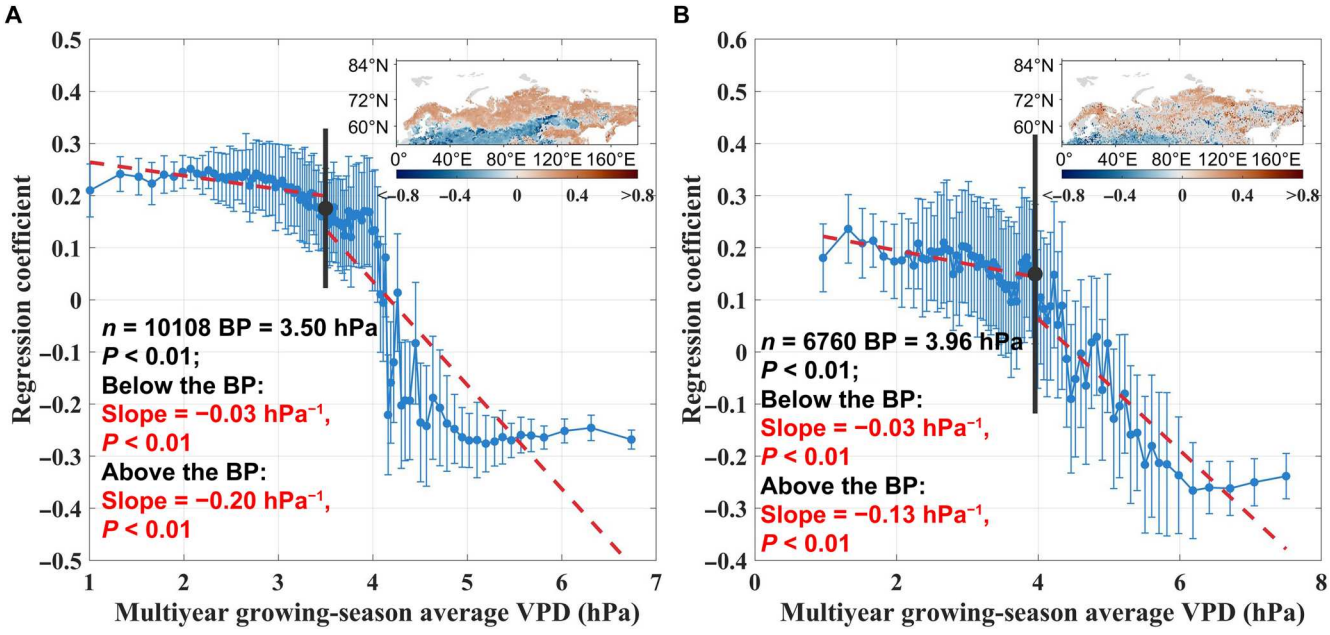

Fig. 4. The thresholds in the relationship between VPD and the sensitivity of vegetation productivity to VPD for high-latitude ecosystems. The R.c of average growing-season VPD to average growing-season vegetation productivity proxies, which were (**A**) GPP-FLUXCOM (during 1980–2018) and (**B**) CSIF (during 2000–2019) as a function of multiyear growing-season average VPD in high-latitude Eurasia (0° to 180°E, 50° to 85°N). The blue points and error bars represent the median and SD of R.c in each bin, respectively (see Materials and Methods). The nonparametric Pettitt test was used to detect the occurrence of BPs in the medians, which are shown as black points and heavy lines. The red dotted line represents the line-fitting curve of medians below or above the BP. The insets show the spatial pattern of the regression coefficient of VPD to vegetation productivity proxies during the growing season. Only the grid cells with the regression result that passed the test of significance ($P < 0.05$) were analyzed and shown.

once the atmospheric aridity level surpasses a critical threshold at the vegetation location. This study identifies a VPD threshold specific to high-latitude ecosystems, which is strongly correlated with the local climatic conditions in the vegetation region. In addition, this finding suggests that there may be differences in vegetation stomatal responses to VPD in various levels of atmospheric dryness. To investigate the potential mechanism behind this VPD threshold, we conducted ridge regression analysis using average growing-season VPD, SM, T, solar radiation, wind speed, and GPP-FLUXCOM as independent variables as well as average growing-season transpiration rate as the dependent variable in the northern Eurasia region (fig. S11). Here, we examined the relationship between VPD and transpiration rate because the rate of transpiration is directly related to stomatal conductance (*42*–*45*). When the average VPD during the growing season was below the threshold of 3.85 hPa, the transpiration rate showed a positive sensitivity to VPD, and the sensitivity value slightly increased with the increase of environmental VPD. This suggests that plant stomata were fully open, in accordance with previous studies that also observed stomatal opening under low VPD conditions (*46*, *47*). Consequently, it is possible that photosynthesis was not barely restricted by VPD. Above the VPD threshold, the positive sensitivity of transpiration rate declined considerably. This indicates that leaf stomatal conductance was starting to be substantially limited by VPD, leading to a corresponding inhibition of photosynthesis. The threshold effect of stomatal conductance in response to VPD has been documented in previous experimental studies (*31*, *48*, *49*). Nonetheless, it should be noted that the threshold may vary considerably among different plant species. This variation could be attributed to differences in stomatal regulation capacity, which varies among species (*50*–*53*).

We further investigated how water stress affected the sensitivity of GPP to VPD by exploring the relationship between GPP and VPD under different average growing-season VPD and SM conditions (fig. S12). Above a greater VPD threshold, negative GPP response to VPD was observed under conditions of higher SM. Under conditions of increasing VPD, sufficient SM enables vegetation to maintain high transpiration efficiency, which can reduce the impact of VPD on leaf stomatal conductance and vegetation photosynthesis. These findings support the notion that plants balance various costs, such as productivity and leaf T regulation during drought, by operating stomata at the edge of the supply capacity of the plant's hydraulic system (*54*–*56*). However, we found that the pattern of GPP sensitivity to VPD varied more substantially with changes in the average growing-season VPD overall compared to the influence of SM. Negative GPP response to VPD is common when the average VPD during the growing season is 4 hPa or higher, regardless of SM conditions. This pattern highlights the critical role of VPD background values in determining the response of GPP to VPD.

Our hemispheric-scale analysis of the influence of VPD as an independent variable on vegetation productivity was an attempt to identify what role VPD in isolation plays in influencing vegetation production and to what extent it affects vegetation production. We found that VPD in isolation had a strong impact on vegetation productivity and revealed the strong counteraction between the direct effect of T and T-associated VPD effect on vegetation productivity and the enhancing effect of the direct effect of SM and SM-

associated VPD effect on the vegetation productivity in most parts of the NH. In addition, we proposed and accepted a hypothesis that there exists an average growing-season VPD threshold of the sensitivity of vegetation productivity to VPD, which led to the positive response of vegetation productivity to VPD in low VPD regions, such as high-latitude ecosystems, and the negative response of vegetation productivity to VPD in other parts of the NH with higher VPD. Our findings provide insights into the role VPD plays in terrestrial ecosystems, disentangle the interaction between VPD and T or SM on vegetation productivity, and reveal the potential threat of prospective increasing VPD under global warming (*2*, *57*) in high-latitude ecosystems.

Note that, however, the extent to which VPD affects ecosystems is still highly uncertain due to the possible carryover effect (*58*) of climatic factors on terrestrial ecosystems. More in-depth studies using datasets with different time scales are needed in the future to more accurately assess the impact of VPD on vegetation productivity. In addition, station-based analysis is needed to further detect more exact values of the VPD threshold for different ecosystems and to further reveal the mechanism for the positive response of vegetation productivity to VPD under wetter conditions (*59*). Continuous monitoring and dedicated experiments could improve our understanding of the role of VPD in terrestrial ecosystems.

MATERIALS AND METHODS

Vegetation productivity

The CSIF dataset (*60*), LAI-MODIS dataset, and GPP derived from empirical models based on flux tower observations (FLUXCOM) were used to indicate vegetation productivity in this study. The clear-sky condition CSIF dataset was generated at moderate spatio-temporal resolutions (0.05° × 0.05° and 4 days) and over the 2000–2019 period by training a neural network with surface reflectance from the MODIS reflectance dataset (MCD43C4 V006) and SIF from the Orbiting Carbon Observatory-2 (OCO-2). The CSIF not only shows high accuracy when validated against the satellite-retrieved OCO-2 SIF but also exhibits a strong correlation with GPP estimated from flux towers. The MOD15A2H Version 6 MODIS combined with LAI and fraction of photosynthetically active radiation product is an 8-day composite dataset with a 500-m pixel size available from 2000. The algorithm chooses the "best" pixel available from all acquisitions of the Terra sensor within the 8-day period. The FLUXCOM GPP with a spatial resolution of 0.5° × 0.5° is a monthly dataset simulated from empirical models forced by eddy covariance data, remote sensing data, and climate data (*61*). The empirical models were trained by random forests, artificial neural networks, and multivariate adaptive regression spline algorithms. Here, the FLXUCOM carbon fluxes data driven by the ERA5 climate reanalysis from 1980 to 2018 were used. All datasets were aggregated to a spatial resolution of 0.5° before analysis.

Climate, SM, and transpiration data

The monthly root-zone SM and transpiration at a spatial resolution of 0.25° were obtained from the Global Land Evaporation Amsterdam Model (GLEAM) version 3.5 datasets, which is a global dataset spanning the 41-year period from 1980 to 2020 and based on satellite and reanalysis data. The monthly 2-m air T, dew point T, 10-m wind speed, and SM were obtained from the ERA5 for the global climate and weather with a spatial resolution of 31 km. Here, SM content between 0 and 1 m was calculated by summing up the moisture content for each layer and weighting it by the thickness of the layer (*16*). The monthly surface net downward shortwave radiation at a spatial resolution of 0.625° × 0.5° was obtained from the Modern-Era Retrospective analysis for Research and Applications, Version 2 (MERRA-2) datasets beginning in 1980 (*62*). According to the Clausius-Clapeyron relation, we used monthly 2-m T and dew point data to calculate VPD based on the ERA5 dataset (*27*). All datasets were aggregated to a spatial resolution of 0.5°.

Aridity index

The aridity index (AI), defined as the ratio of annual precipitation to annual potential evapotranspiration, was used to identify global climate zones. Under this quantitative indicator, the NH was classified into arid (AI < 0.2), semiarid (0.2 ≤ AI < 0.5), subhumid (0.5 ≤ AI < 0.65), and humid (AI ≥ 0.65) subtypes. The AI was obtained from the Global Aridity Index and Potential Evapotranspiration (ET0) Climate Database v2 (*63*).

Pearson's correlation analysis

Pearson's correlation analysis between VPD and SM or T was used to determine the coupling between VPD and SM and T. The significance of Pearson's correlations was assessed at $P < 0.05$.

Ridge regression analysis

To account for multicollinearity among VPD, T, and SM, we performed a ridge regression analysis to verify the effect of VPD on vegetation productivity. Ridge regression is a widely used linear regularization method and independent statistical test commonly used in plant physiology and ecophysiology, which improves the mean square error of estimation by introducing a penalty term in the minimized residual equation, and substantially increases the reliability of the estimates in cases of strong multicollinearity. Because the advantage of ridge regression, it is widely used in the research of the response of the ecosystem to changes in climate variables, especially in the regression analysis when there exists severe multicollinearity among climate variables [e.g., severe multicollinearity among daytime warming and night-time warming (*24*) or seasonal mean T and precipitation (*64*)]. The VIF, which assesses how much the variance of an estimated regression coefficient increases when predictors are correlated, is used to detect the severity of multicollinearity in the regression analysis. When notable multicollinearity issues exist, the VIF will be very large for the variables involved.

In the regression analysis, all variables were normalized with *z* score and detrended using a linear model to focus on the interannual relationship between VPD and vegetation productivity. Because we focused on the relationship among environmental factors, SM, and vegetation, to eliminate the interference of misleading relationships in bare land, only the regions with multiyear (during 2000–2019) average CSIF values larger than 0.006 mW m^{-2} nm^{-1} sr^{-1} were selected for the ridge regression analysis following (*60*). The significance of the ridge regression analysis was assessed using an *F* test at a significance level of 0.05.

Principal component regression analysis

We also used the principal component regression analysis (*28*) to verify the effect of VPD on vegetation productivity. The principal component regression transforms the original dataset into a new set of orthogonal (i.e., uncorrelated) variables, which are called

PCs. After transformation, a least square regression on this reduced set of PCs was performed. The principal component regression avoids collinearity of climatic variables because PCs are uncorrelated to each other. The low-variance PCs indicate collinearity among original predictors and thus should be excluded in the regression step. Here, the PCs that explain less than 5% of the overall variance of climatic variables were excluded from the regression (*64*). Only the regions with multiyear average annual CSIF values larger than 0.006 mW m^{-2} nm^{-1} sr^{-1} were selected for the regression analysis. The significance of the principal component regression analysis was assessed using an F test at a significance level of 0.05.

PLS-SEM

PLS-SEM is a multivariate statistical analysis technique for path analysis that requires previous knowledge to establish the relationships among the variables. In contrast to the common structural equation modeling, which is based on maximum likelihood, PLS-SEM requires neither a large sample size nor a specific assumption on the distribution of the data and works well with missing data. When the sample size and data distribution do not conform to the requirements of common SEMs, for example, when long-term observations are not available, PLS-SEM has a more functional advantage. Here, we ran our PLS-SEM model using 1000 bootstraps to validate the estimates of path coefficients and the coefficients of determination. The degree of direct effect, indirect effect, and total effect can be quantified by the direct influence coefficient, indirect influence coefficient, and total influence coefficient, respectively. Models with different input variables were evaluated using the GoF statistic. GoF assesses the overall prediction performance of the model by considering the commonality and R^2 coefficients. All variables were standardized before conducting the path analysis and were detrended using a linear model in the path analysis to focus on the interannual relationship between environmental factors and vegetation productivity. Only the regions with multiyear (during 2000–2019) average CSIF values larger than 0.006 mW m^{-2} nm^{-1} sr^{-1} were selected for the PLS-SEM analysis.

VPD threshold

To detect the threshold in the relationship between VPD and the sensitivity of vegetation productivity to VPD, all grid points were firstly sorted into $\sqrt{n}$ (rounded to the nearest integer) bins, where n is the number of grid points, according to the ascending order of average growing-season VPD. Then, the VPD threshold, which was defined as BPs of the medians of the groups, was quantified by the nonparametric Pettitt breakpoint test (*30*), which has been widely used to detect abrupt changes in observed climatic and hydrological series (*65*, *66*).

Supplementary Materials

This PDF file includes:

Figs. S1 to S12

REFERENCE AND NOTES

1. B. N. Sulman, D. T. Roman, K. Yi, L. Wang, R. P. Phillips, K. A. Novick, High atmospheric demand for water can limit forest carbon uptake and transpiration as severely as dry soil. *Geophys. Res. Lett.* **43**, 9686–9695 (2016).
2. K. A. Novick, D. L. Ficklin, P. C. Stoy, C. A. Williams, G. Bohrer, A. C. Oishi, S. A. Papuga, P. D. Blanken, A. Noormets, B. N. Sulman, R. L. Scott, L. Wang, R. P. Phillips, The increasing importance of atmospheric demand for ecosystem water and carbon fluxes. *Nat. Clim. Change* **6**, 1023–1027 (2016).
3. A. Park Williams, C. D. Allen, A. K. Macalady, D. Griffin, C. A. Woodhouse, D. M. Meko, T. W. Swetnam, S. A. Rauscher, R. Seager, H. D. Grissino-Mayer, J. S. Dean, E. R. Cook, C. Gangodagamage, M. Cai, N. G. McDowell, Temperature as a potent driver of regional forest drought stress and tree mortality. *Nat. Clim. Change* **3**, 292–297 (2013).
4. K. A. Novick, C. F. Miniat, J. M. Vose, Drought limitations to leaf-level gas exchange: Results from a model linking stomatal optimization and cohesion-tension theory. *Plant Cell Environ.* **39**, 583–596 (2016).
5. D. Eamus, N. Boulain, J. Cleverly, D. D. Breshears, Global change-type drought-induced tree mortality: Vapor pressure deficit is more important than temperature per se in causing decline in tree health. *Ecol. Evol.* **3**, 2711–2729 (2013).
6. D. B. Lobell, G. L. Hammer, G. McLean, C. Messina, M. J. Roberts, W. Schlenker, The critical role of extreme heat for maize production in the United States. *Nat. Clim. Change* **3**, 497–501 (2013).
7. D. Zhang, Q. Du, Z. Zhang, X. Jiao, X. Song, J. Li, Vapour pressure deficit control in relation to water transport and water productivity in greenhouse tomato production during summer. *Sci. Rep.* **7**, 43461 (2017).
8. B. He, C. Chen, S. Lin, W. Yuan, H. W. Chen, D. Chen, Y. Zhang, L. Guo, X. Zhao, X. Liu, S. Piao, Z. Zhong, R. Wang, R. Tang, Worldwide impacts of atmospheric vapor pressure deficit on the interannual variability of terrestrial carbon sinks. *Natl. Sci. Rev.* **9**, nwab150 (2021).
9. J. Ding, T. Yang, Y. Zhao, D. Liu, X. Wang, Y. Yao, S. Peng, T. Wang, S. Piao, Increasingly important role of atmospheric aridity on Tibetan Alpine grasslands. *Geophys. Res. Lett.* **45**, 2852–2859 (2018).
10. C. Yi, E. Pendall, P. Ciais, Focus on extreme events and the carbon cycle. *Environ. Res. Lett.* **10**, 070201 (2015).
11. G. G. Katul, R. Oren, S. Manzoni, C. Higgins, M. B. Parlange, Evapotranspiration: A process driving mass transport and energy exchange in the soil-plant-atmosphere-climate system. *Rev. Geophys.* **50**, 10.1029/2011RG000366, (2012).
12. M. Huang, S. Piao, P. Ciais, J. Peñuelas, X. Wang, T. F. Keenan, S. Peng, J. A. Berry, K. Wang, J. Mao, R. Alkama, A. Cescatti, M. Cuntz, H. De Deurwaerder, M. Gao, Y. He, Y. Liu, Y. Luo, R. B. Myneni, S. Niu, X. Shi, W. Yuan, H. Verbeeck, T. Wang, J. Wu, I. A. Janssens, Air temperature optima of vegetation productivity across global biomes. *Nat. Ecol. Evol.* **3**, 772–779 (2019).
13. Ü. Niinemets, Global-scale climatic controls of leaf dry mass per area, density, and thickness in trees and shrubs. *Ecology* **82**, 453–469 (2001).
14. S. I. Seneviratne, T. Corti, E. L. Davin, M. Hirschi, E. B. Jaeger, I. Lehner, B. Orlowsky, A. J. Teuling, Investigating soil moisture–climate interactions in a changing climate: A review. *Earth-Sci. Rev.* **99**, 125–161 (2010).
15. S. Zhou, Y. Zhang, A. Park Williams, P. Gentine, Projected increases in intensity, frequency, and terrestrial carbon costs of compound drought and aridity events. *Sci. Adv.* **5**, eaau5740 (2019).
16. L. Liu, L. Gudmundsson, M. Hauser, D. Qin, S. Li, S. I. Seneviratne, Soil moisture dominates dryness stress on ecosystem production globally. *Nat. Commun.* **11**, 4892 (2020).
17. B. D. Stocker, J. Zscheischler, T. F. Keenan, I. C. Prentice, J. Peñuelas, S. I. Seneviratne, Quantifying soil moisture impacts on light use efficiency across biomes. *New Phytol.* **218**, 1430–1449 (2018).
18. A. P. Williams, C. D. Allen, C. I. Millar, T. W. Swetnam, J. Michaelsen, C. J. Still, S. W. Leavitt, Forest responses to increasing aridity and warmth in the southwestern United States. *Proc. Natl. Acad. Sci. U.S.A.* **107**, 21289–21294 (2010).
19. L. Liu, S. Peng, A. AghaKouchak, Y. Huang, Y. Li, D. Qin, A. Xie, S. Li, Broad consistency between satellite and vegetation model estimates of net primary productivity across global and regional scales. *J. Geophys. Res. Biogeo.* **123**, 3603–3616 (2018).
20. H. Hersbach, B. Bell, P. Berrisford, S. Hirahara, A. Horányi, J. Muñoz-Sabater, J. Nicolas, C. Peubey, R. Radu, D. Schepers, A. Simmons, C. Soci, S. Abdalla, X. Abellan, G. Balsamo, P. Bechtold, G. Biavati, J. Bidlot, M. Bonavita, G. Chiara, P. Dahlgren, D. Dee, M. Diamantakis, R. Dragani, J. Flemming, R. Forbes, M. Fuentes, A. Geer, L. Haimberger, S. Healy, R. J. Hogan, E. Hólm, M. Janisková, S. Keeley, P. Laloyaux, P. Lopez, C. Lupu, G. Radnoti, P. Rosnay, I. Rozum, F. Vamborg, S. Villaume, J.-N. Thépaut, The ERA5 global reanalysis. *Q. J. Roy. Meteorol. Soc.* **146**, 1999–2049 (2020).
21. B. Martens, D. G. Miralles, H. Lievens, R. van der Schalie, R. A. M. de Jeu, D. Fernández-Prieto, H. E. Beck, W. A. Dorigo, N. E. C. Verhoest, GLEAM v3: Satellite-based land evaporation and root-zone soil moisture. *Geosci. Model Dev. Discuss.* **10**, 1903–1925 (2017).
22. D. Wu, X. Zhao, S. Liang, T. Zhou, K. Huang, B. Tang, W. Zhao, Time-lag effects of global vegetation responses to climate change. *Glob. Chang. Biol.* **21**, 3520–3531 (2015).
23. J. H. Kim, Multicollinearity and misleading statistical results. *Korean J. Anesthesiol.* **72**, 558–569 (2019).
24. S. Peng, S. Piao, P. Ciais, R. B. Myneni, A. Chen, F. Chevallier, A. J. Dolman, I. A. Janssens, J. Peñuelas, G. Zhang, S. Vicca, S. Wan, S. Wang, H. Zeng, Asymmetric effects of daytime and night-time warming on Northern Hemisphere vegetation. *Nature* **501**, 88–92 (2013).

25. D. R. Jensen, D. E. Ramirez, Revision: Variance inflation in regression. *Adv. Decis. Sci.* **2013**, 671204, 2013
26. A. E. Hoerl, R. W. Kennard, Ridge regression: Biased estimation for nonorthogonal problems. *Technometrics* **42**, 80–86 (2000).
27. A. Barkhordarian, K. W. Bowman, N. Cressie, J. Jewell, J. Liu, Emergent constraints on tropical atmospheric aridity—Carbon feedbacks and the future of carbon sequestration. *Environ. Res. Lett.* **16**, 114008 (2021).
28. S. H. Park, Collinearity and optimal restrictions on regression parameters for estimating responses. *Technometrics* **23**, 289–295 (1981).
29. J. Wang, F. Pan, J. Soininen, J. Heino, J. Shen, Nutrient enrichment modifies temperature-biodiversity relationships in large-scale field experiments. *Nat. Commun.* **7**, 13960 (2016).
30. A. N. Pettitt, A simple cumulative sum type statistic for the change-point problem with zero-one observations. *Biometrika* **67**, 79–84 (1980).
31. D. R. Woodruff, F. C. Meinzer, K. A. McCulloh, Height-related trends in stomatal sensitivity to leaf-to-air vapour pressure deficit in a tall conifer. *J. Exp. Bot.* **61**, 203–210 (2010).
32. D. K. Soni, S. Ranjan, R. Singh, P. B. Khare, U. V. Pathre, P. A. Shirke, Photosynthetic characteristics and the response of stomata to environmental determinants and ABA in *Selaginella bryopteris*, a resurrection spike moss species. *Plant Sci.* **207**, 191–192 (2012).
33. A. Sellin, M. Alber, M. Keinänen, P. Kupper, J. Lihavainen, K. Lõhmus, E. Oksanen, A. Sõber, J. Sõber, A. Tullus, Growth of northern deciduous trees under increasing atmospheric humidity: Possible mechanisms behind the growth retardation. *Reg. Environ. Change* **17**, 2135–2148 (2017).
34. A. Sellin, A. Tullus, A. Niglas, E. Õunapuu, A. Karusion, K. Lõhmus, Humidity-driven changes in growth rate, photosynthetic capacity, hydraulic properties and other functional traits in silver birch (*Betula pendula*). *Ecol. Res.* **28**, 523–535 (2013).
35. C. Grossiord, T. N. Buckley, L. A. Cernusak, K. A. Novick, B. Poulter, R. T. W. Siegwolf, J. S. Sperry, N. G. McDowell, Plant responses to rising vapor pressure deficit. *New Phytol.* **226**, 1550–1566 (2020).
36. J. L. Monteith, A reinterpretation of stomatal responses to humidity. *Plant Cell Environ.* **18**, 357–364 (1995).
37. V. Novák, J. Vidoň, Transpiration and nutrient uptake dynamics in maize (*Zea mays* L.). *Ecol. Model.* **166**, 99–107 (2003).
38. L. A. Cernusak, K. Winter, B. L. Turner, Transpiration modulates phosphorus acquisition in tropical tree seedlings. *Tree Physiol.* **31**, 878–885 (2011).
39. J. Lihavainen, V. Ahonen, S. Keski-Saari, A. Sõber, E. Oksanen, M. Keinänen, Low vapor pressure deficit reduces glandular trichome density and modifies the chemical composition of cuticular waxes in silver birch leaves. *Tree Physiol.* **37**, 1166–1181 (2017).
40. E. Oksanen, J. Lihavainen, M. Keinänen, S. Keski-Saari, S. Kontunen-Soppela, A. Sellin, A. Sõber. Northern Forest Trees Under Increasing Atmospheric Humidity. F. Cánovas, U. Lüttge, R. Matyssek, H. Pretzsch, Eds. Progress in Botany, vol 80. (Springer, Cham., 2018) https://doi.org/10.1007/124_2017_15
41. A. Niglas, P. Kupper, A. Tullus, A. Sellin, Responses of sap flow, leaf gas exchange and growth of hybrid aspen to elevated atmospheric humidity under field conditions. *AoB Plants* **6**, plu021 (2014).
42. F. Hayat, M. A. Ahmed, M. Zarebanadkouki, M. Javaux, G. Cai, A. Carminati, Transpiration Reduction in Maize (*Zea mays* L) in response to soil drying. *Front. Plant Sci.* **10**, 1695 (2020).
43. J. Martínez-Vilalta, R. Poyatos, D. Aguadé, J. Retana, M. Mencuccini, A new look at water transport regulation in plants. *New Phytol.* **204**, 105–115 (2014).
44. I. Jauregui, S. A. Rothwell, S. H. Taylor, M. A. J. Parry, E. Carmo-Silva, I. C. Dodd, Whole plant chamber to examine sensitivity of cereal gas exchange to changes in evaporative demand. *Plant Methods* **14**, 97 (2018).
45. J. Macková, M. Vašková, P. Macek, M. Hronková, L. Schreiber, J. Šantrůček, Plant response to drought stress simulated by ABA application: Changes in chemical composition of cuticular waxes. *Environ. Exp. Bot.* **86**, 70–75 (2013).
46. R. Schoppach, W. Sadok, Differential sensitivities of transpiration to evaporative demand and soil water deficit among wheat elite cultivars indicate different strategies for drought tolerance. *Environ. Exp. Bot.* **84**, 1–10 (2012).
47. S. Medina, R. Vicente, M. T. Nieto-Taladriz, N. Aparicio, F. Chairi, O. Vergara-Diaz, J. L. Araus, The plant-transpiration response to Vapor Pressure Deficit (VPD) in durum wheat is associated with differential yield performance and specific expression of genes involved in primary metabolism and water transport. *Front. Plant Sci.* **9**, 1994 (2019).
48. L. A. Cernusak, G. R. Goldsmith, M. Arend, R. T. W. Siegwolf, Effect of vapor pressure deficit on gas exchange in wild-type and abscisic acid–insensitive plants. *Plant Physiol.* **181**, 1573–1586 (2019).
49. J. Li, X. Li, Response of stomatal conductance of two tree species to vapor pressure deficit in three climate zones. *J. Arid. Land* **6**, 771–781 (2014).
50. G. Pasqualotto, V. Carraro, E. Suarez Huerta, T. Anfodillo, Assessment of canopy conductance responses to vapor pressure deficit in eight hazelnut orchards across continents. *Front. Plant Sci.* **12**, 767916 (2021).
51. T. N. Buckley, The control of stomata by water balance. *New Phytol.* **168**, 275–292 (2005).
52. P. J. Franks, Passive and active stomatal control: Either or both? *New Phytol.* **198**, 325–327 (2013).
53. P. J. Franks, G. D. Farquhar, The mechanical diversity of stomata and its significance in gas-exchange control. *Plant Physiol.* **143**, 78–87 (2007).
54. P. Cruiziat, H. Cochard, T. Améglio, Hydraulic architecture of trees: Main concepts and results. *Ann. For. Sci.* **59**, 723–752 (2002).
55. J. S. Sperry, Coordinating stomatal and xylem functioning – an evolutionary perspective. *New Phytol.* **162**, 568–570 (2004).
56. N. Martin-StPaul, S. Delzon, H. Cochard, Plant resistance to drought depends on timely stomatal closure. *Ecol. Lett.* **20**, 1437–1447 (2017).
57. N. G. McDowell, C. D. Allen, Darcy's law predicts widespread forest mortality under climate warming. *Nat. Clim. Change* **5**, 669–672 (2015).
58. X. Lian, S. Piao, A. Chen, K. Wang, X. Li, W. Buermann, C. Huntingford, J. Peñuelas, H. Xu, R. B. Myneni, Seasonal biological carryover dominates northern vegetation growth. *Nat. Commun.* **12**, 983 (2021).
59. J. K. Green, J. Berry, P. Ciais, Y. Zhang, P. Gentine, Amazon rainforest photosynthesis increases in response to atmospheric dryness. *Sci. Adv.* **6**, eabb7232 (2020).
60. Y. Zhang, J. Joiner, S. H. Alemohammad, S. Zhou, P. Gentine, A global spatially contiguous solar-induced fluorescence (CSIF) dataset using neural networks. *Biogeosciences* **15**, 5779–5800 (2018).
61. M. Jung, S. Koirala, U. Weber, K. Ichii, F. Gans, G. Camps-Valls, D. Papale, C. Schwalm, G. Tramontana, M. Reichstein, The FLUXCOM ensemble of global land-atmosphere energy fluxes. *Sci. Data* **6**, 74 (2019).
62. R. Gelaro, W. McCarty, M. J. Suárez, R. Todling, A. Molod, L. Takacs, C. A. Randles, A. Darmenov, M. G. Bosilovich, R. Reichle, K. Wargan, L. Coy, R. Cullather, C. Draper, S. Akella, V. Buchard, A. Conaty, A. M. da Silva, W. Gu, G. K. Kim, R. Koster, R. Lucchesi, D. Merkova, J. E. Nielsen, G. Partyka, S. Pawson, W. Putman, M. Rienecker, S. D. Schubert, M. Sienkiewicz, B. Zhao, The Modern-Era Retrospective Analysis for Research and Applications, Version 2 (MERRA-2). *J. Climate* **30**, 5419–5454 (2017).
63. T. Antonio, Z. Robert, *Global Aridity Index and Potential Evapotranspiration (ET0) Climate Database v2*. (2019).
64. X. Wang, P. Ciais, Y. Wang, D. Zhu, Divergent response of seasonally dry tropical vegetation to climatic variations in dry and wet seasons. *Glob. Chang. Biol.* **24**, 4709–4717 (2018).
65. G. Verstraeten, J. Poesen, G. Demarée, C. Salles, Long-term (105 years) variability in rain erosivity as derived from 10-min rainfall depth data for Ukkel (Brussels, Belgium): Implications for assessing soil erosion rates. *J. Geophys. Res. Atmos.* **111**, D22109 (2006).
66. X. Xu, D. Yang, H. Yang, H. Lei, Attribution analysis based on the Budyko hypothesis for detecting the dominant cause of runoff decline in Haihe basin. *J. Hydrol.* **510**, 530–540 (2014).

Acknowledgments

Funding: This work has been supported by the National Key Scientific Research and Development Program of China (grant 2017YFA0603601) and the Strategic Priority Research Program of the Chinese Academy of Sciences (grant XDA20060402). Support from the Swedish strategic research areas BECC and MERGE, as well as STINT (CH2020-8799 and CH2020-8767), are also acknowledged. **Author contributions:** B.H., Y.C., and Z.Z. designed the research. Z.Z., Y.D., R.T., X.X., and Y.Z. performed the analysis. Z.Z. and B.H. drafted the paper. Y.-P.W., H.W.C., D.C., Y.H.F., L.G., L.H., W.Y., X.H., H.L., and L.S. contributed to the interpretation of the results and to the writing of the paper. **Competing interests:** The authors declare that they have no competing interests. **Data and materials availability:** All data needed to evaluate the conclusions in the paper are present in the paper and/or the Supplementary Materials. The source data were freely accessed from the following locations: the CSIF dataset is from https://osf.io/8xqy6/. The LAI-MODIS dataset is from https://modis.gsfc.nasa.gov/data/. The FLUXCOM GPP dataset is from www.fluxcom.org/domains/fluxcom.org/CF-Products/. The ERA5 dataset is from https://cds.climate.copernicus.eu/cdsapp#!/dataset/reanalysis-era5-single-levels-monthly-means?tab=form. The GLEAM SM and transpiration data are from www.gleam.eu/#datasets. The MERRA-2 downward shortwave radiation dataset is from https://disc.gsfc.nasa.gov/datasets?project=MERRA-2. The AI dataset is from https://doi.org/10.6084/m9.figshare.7504448.v3. The source codes for conducting PLS-SEM can be obtained from the PLS-SEM Toolbox available on MATLAB Central File Exchange. The toolbox was downloaded on 6 February 2022 from the following URL: www.mathworks.com/matlabcentral/fileexchange/54147-pls-sem-toolbox.

Submitted 13 October 2022
Accepted 7 July 2023
Published 9 August 2023
10.1126/sciadv.adf3166

Ridge regression and attribution

Ridge regression minimizes the effects of high multicollinearity (i.e., correlation) among the independent variables, particularly in alleviating interference resulting from strong correlations between temperature and soil moisture, or DTR and SM. Prior to conducting the ridge regression analysis, long-term linear trends were removed from all variables. The detrended time series were then converted into z-scores by dividing the anomalies (from the linear trend) by their standard deviations for the period from 1980 to 2023.

Sensitivity experiment

To further quantify the long-term impact of diurnally asymmetric warming on VPD changes, we used monthly DTR, mean temperature, and soil moisture as independent variables in a random forest regression to predict monthly VPD values from 1980 to 2023. This random forest regression approach was chosen specifically to capture the complex nonlinear relationships among these variables. We first trained the model using 80% of the data randomly selected as the training set. The median R^2 for the validation set reached 0.91 using the HadISD dataset and 0.95 using ERA5-Land data, indicating that the random forest model effectively captures most of the variance in VPD across land areas. We then used all data to re-train the models to obtain the fitted VPD values (VPD_{fitted}). Subsequently, three sensitivity experiments were conducted, one for each independent variable, keeping the tested variable constant at its mean value for each month during the control period, defined as the initial three years (1980–1982), while the other two variables varied according to the input. The difference between VPD_{fitted} and the estimated VPD from each sensitivity experiment was considered the contribution of DTR, TM, and SM change to the VPD change, denoted as VPD_{DTR}, VPD_{TM}, and VPD_{SM}, respectively.